Characterization of Spin Hall and Magneto-ionic Devices for Logic, Memory and Neuromorphic Applications

A DISSERTATION

SUBMITTED TO THE FACULTY OF

UNIVERSITY OF MINNESOTA

BY

PROTYUSH SAHU

IN PARTIAL FULFILLMENT OF THE REQUIREMENTS

FOR THE DEGREE OF

DOCTOR OF PHILOSOPHY

Advisor: Jian-Ping Wang

July 2021

ACKNOWLEDGEMENTS

I want to thank my advisor, who has patiently supported and guided me for the past six years. His insights into problem-solving, through countless discussions, brainstorming became an excellent avenue for me to follow.

I would also like to thank my colleagues with whom I shared my research and the office. Dr. Yang Lv was one of my first mentors who taught me device fabrication and the first half of the electrical measurements. The techniques taught to me by Yang would go on to become very fruitful for the rest of my Ph.D. Dr. Mahendra DC taught me about the second half of the characterization techniques and guided me through several of my projects. Most of the work done by me is almost a direct continuation of the projects from Yang and Mahendra. Thomas Peterson and Yihong Fan are other key people during my PhD. Yihong is an expert on spin pumping experimental setup and played a significant role in spin pumping measurements of Gd-BiSe project. He did all the spin pumping experiments and analyzed the data. Tom is the expert on data analysis who did several of the analysis on spin Hall projects and material characterization. He performed all the data analysis on the second harmonic experiment. Dr. Junyang Chen and Dr. Delin Zhang taught me how to grow thin films and trained me well on deposition systems. All the research wouldn't have been possible without helpful discussion and inputs from Deyuan Lyu, Zhengyang Zhao, Hongshi Li, Brandon Zink, Przemyslaw Swatek, Anthony Hurben, Onri Benally.

Jason Myers, from Charfac, played a crucial role in several of my projects. He was my primary contact for transmission electron microscopy (Bi_2Se_3 and magnetoionic stack) and helped me through analysis, discussion, etc. Dr. Javier Garcia-Barriocanal also spent countless hours training me on my X-ray diffraction skills. Dr. Greg Haugstad performed RBS characterization for me.

My projects wouldn't have been possible without collaboration from other universities. During the latter half of my Ph.D., a major partnership was forged with Yuan Lu and his colleagues in LNRS France. Henri Jaffres, Jean-Marie-George, Sylvie Migot, Xavier Devaux, Huong Dang are some of the key players for Gd-BiSe project. Yuan and his team performed TEM characterization and analysis for Gd-BiSe project.

I would also like to thank Timothy Peterson, Zhen Jiang and Gordon Stecklein from Prof. Paul Crowell's group for training and preparing me for physical property measurement systems.

I'm also thankful for the financial support from C-SPIN center of the STARnet program and ASCENT center from JUMP program. My discussions with the PIs, students and postdocs, and inputs from liaisons played a major role during my project.

Lastly, I would like to thank my parents and family, whose unconditional love and support through these years in Minnesota were crucial for completing my study.

DEDICATION

ମୋର ପିତାମାତା, ପରିବାର ଏବଂ ସମସ୍ତ ଶିକ୍ଷକମାନଙ୍କ ପାଇଁ |

ABSTRACT

This thesis is divided into two parts. In the first part, my research is focused on spin-to-charge conversion in amorphous Gd (40%)-alloyed Bismuth Selenide (60%) (BSG) thin films. The spin Hall effect has emerged as a key proponent for spintronic devices. Such devices typically consist of a bilayer structure made from a spin Hall channel and a ferromagnet. Polycrystalline Bi_2Se_3 was discovered to have a large spin Hall effect. Spin Hall angle and spin Hall efficiency (SCE) have been key parameters for comparing spin Hall channels. However, the output voltage becomes an essential requirement for spin logic devices, which also depends on resistivity. Gd (40%) alloyed Bi_2Se_3, grown by sputtering, can fill these gaps for spin logic devices. The material is amorphous, ensuring good scalability. Resistivity as a function of temperature showed strong signs of 3D variable range hopping with a characteristic Mott temperature of 9.7×10^5 K and a room temperature resistivity of 60,000 μOhm.cm. With 5nm in-plane CoFeB, the spin pumping results show good symmetric peaks for different excitation frequencies. The spin to charge conversion efficiency ($\sim J_c/J_s$) increased with decreasing thickness of BSG. Second harmonic measurements were performed to characterize thermal effects. The spin-orbit torque was negligible due to the dominance of thermal effects and current shunting through the ferromagnet. Anomalous Nernst effect was found to be the dominant thermal effect. However, it couldn't explain our spin pumping results due to the lack of BSG thickness dependence and the dominance of the first harmonic voltage. The spin pumping was concluded to originate from the inverse spin Hall effect in BSG layer.

My research focuses on irreversible magneto-ionic devices for one-time-programmable memory and neuromorphic applications in the second part of the thesis. Magneto-ionic devices rely

on ionic movement through a gate dielectric to manipulate the magnetic properties of a magnetic material. We use $Co_{20}Fe_{60}B_{20}$ perpendicular magnetic anisotropy (PMA) thin films. CoFeB/MgO interfacial PMA is a consequence of orbital overlapping between Oxygen and transition metal atoms. We further engineer the device to enable field-free magnetization switching. We use an exchange bias field from an adjacent ferromagnet ($[Co(0.3nm)/Pd(0.7nm)]_3$) separated by a non-magnetic layer (Ta), forming a $[Co(0.3nm)/Pd(0.7nm)]_3$/Ta/CoFeB/MgO structure. Pd (111) was used as the seed layer for $[Co(0.3nm)/Pd(0.7nm)]_3$. The final stack is given by: Substrate/Ta(5nm)/Pd(10nm)/$[Co(0.3nm)/Pd(0.7nm)]_3$/Ta(1nm)/CoFeB(1.3nm)/MgO(2nm).

XRD and HRTEM were used to characterize the film, which showed distinct layers with some interdiffusion and a polycrystalline Pd(111). This stack is then topped with an ionic gate made from 100nm sputtered SiO_x. AHE minor curves showed that the two ferromagnets have weak antiferromagnetic coupling. Application of negative gate voltage decreases the coercivity of CoFeB from ~34 Oe to 16 Oe, signaling a lowered PMA. The exchange bias field magnitude increases from ~ 25 Oe to ~ 45 Oe, due to the decrease in thickness of CoFeB. Major loop measurements show no change in $[Co(0.3nm)/Pd(0.7nm)]_3$ layer with gate voltage. Oxygen ions from SiO_x move towards the interface of MgO/CoFeB interface under negative gate voltage. This creates an overoxidation of the interface and destroys the interfacial PMA of CoFeB. This makes the CoFeB layer go from a bi-stable to a monostable state, resulting in a pathway for a field-free magnetization switch.

CONTENTS

LIST OF TABLES

LIST OF FIGURES

LIST OF SYMBOLS

Symbol/Terminology	**Physical quantity**
α	Magnetic damping constant
M_S	Saturation Magnetization
H_K	Anisotropy field
V	Volume
P	Spin polarization
K_u	Anisotropy constant
k_b	Boltzmann constant
T	Temperature
j_C	Charge current density
j_s	Spin current density
θ_{SHA}	Spin Hall angle
e	Electronic charge
$\hbar$	Reduced Dirac's constant
t_{SH}	Thickness of spin Hall channel
λ_{SD}	Spin diffusion length
ΔH	Hamiltonian shift
μ	Spin magnetic moment of electron
B	Magnetic field

g_S	Electron spin g-factor
μ_B	Bohr Magneton
S	Spin angular momentum
c	Speed of light
H_R	Rashba Hamiltonian
H_D	Dresselhaus Hamiltonian
σ_i	Spin Pauli matrices
p_i	Momentum vector
λ_{IREE}	Inverse Rashba-Edelstein length
λ_{ISHE}	Inverse spin Hall effect length
ρ_{SH}	Resistivity of spin Hall channel
ω	Angular frequency at ferromagnetic resonance
G	Real part of spin-mixing conductance
γ	Gyromagnetic ratio
T_0	Characteristic Mott temperature
V_S	Symmetric voltage
V_A	Anti-symmetric voltage
ΔH	Linewidth
H_0	Resonance field
V_{ISHE}	Inverse spin Hall effect voltage
V_{SSE}	Spin Seebeck effect voltage

Δ_0	Intrinsic linewidth
f	Frequency
K_{eff}	Effective anisotropy constant
E_A	Energy per unit area of the ferromagnet
μ_0	Magnetic permeability
J_{eb}	Exchange coupling constant
k_m	Fermi momentum
P_g	Generation rate of ion-vacancy pairs
P_r	Recombination rate of ion-vacancy pairs
f_0	Vibration frequency of ions
C_{ion}	Ion concentration
E_g	Formation energy
E_r	Recombination energy
γ	Contribution of bond polarization to local E-field
E_m	Oxygen energy migration barrier
a	SiO_x lattice constant

LIST OF ABBREVIATIONS

Abbreviation	**Terminology**
MTJ	Magnetic tunnel junction
TMR	Tunneling magnetoresistance
STT	Spin transfer torque
MRAM	Magnetoresistive random access memory
SOT	Spin orbit torque
MESO	Magnetoelectric spin-orbit
CMOS	Complementary metal-oxide semiconductor
(I)SHE	(Inverse) Spin Hall effect
FM	Ferromagnet
SHA	Spin Hall angle
SCE	Spin-to-charge conversion efficiency
SH	Spin Hall
SD	Spin diffusion
FOR	Frame of reference
SOC	Spin orbit coupling
CIP-GMR	Current in plane giant magnetoresistance
USMR	Unidirectional spin Hall magnetoresistance
IREE	Inverse Rashba-Edelstein length
TEM	Transmission electron microscopy

EDX	Energy dissipative X-ray spectroscopy
SAED	Selected area electron diffraction
EELS	Electron energy loss spectroscopy
ANE	Anomalous Nernst effect
SSE	Spin Seebeck effect
SE	Seebeck effect
SMR	Spin Hall magnetoresistance
FMR	Ferromagnetic resonance
FFT	Fast Fourier transform
HAADF	High angle annular dark field
RBS	Rutherford backscattering
VRH	Variable range hopping
ES	Efros-Shlovski
BSG	Bismuth Selenide Gadolinium
CFB	Cobalt Iron Boron
AHE	Anomalous Hall effect
AMR	Anomalous magnetoresistance
VN	Von-Neumann
OTP	One time programmable
ASIC	Application specific integrated circuit
FPGA	Field programmable gate array
PMA	Perpendicular magnetic anisotropy

SW	Stoner-Wolhfharth
RKKY	Ruderman-Kittel-Kasuya-Yosida
ALD	Atomic layer deposition
PEALD	Plasma-enhanced atomic layer deposition
CVD	Chemical vapor deposition
XRD	X-ray diffraction
RTA	Rapid thermal annealing
SAF	Synthetic antiferromagnet

CHAPTER 1-1: INTRODUCTION

Parts of this section of the thesis has been reproduced verbatim from Sahu et al. APL 112, 122402 (2018) and Sahu et al. arxiv: 1911.03323

1-1.1 Motivation

Moore's law has been a critical driver of technological growth for the last five decades [1,2]. The scaling down of the silicon transistors has created ever denser, faster and power-hungry semiconductor devices. However, this trend is expected to slow down as we go to smaller dimensions. The economics of process engineering would become unfeasible to keep up with the pace of transistor scaling. Therefore, there is a strong push, at least in the nanoelectronics research community, to look beyond the traditional CMOS-based electronics. Spintronics is one of the leading candidates [3-7]. Unlike conventional electronics, in spintronics, the electrons are spin-polarized and create a net flow of angular momentum. The spin polarization of the electrons is an extra degree of freedom, so far unutilized in conventional electronics. Spintronics promises to lower the power consumption for high-density electronic applications [8-10]. Spintronics requires an amalgamation of semiconductors and metals with ferromagnets (FM) to study the underlying physics. A key advantage of spintronics is the permanent/semi-permanent behavior of magnetization, which makes the data bits (0 and 1) non-volatile. This can be advantageous for several memory and logic applications [11-13]. The first primary spintronic device, to make its way into integrated circuits, was magnetic tunnel junction (MTJ) [10, 14-16].

MTJs are two-terminal devices comprising of a ferromagnet/oxide/ferromagnet structure. The relative orientation between the magnetizations of the ferromagnets determines the resistance

of the device. The read operation is done through tunneling magnetoresistance (TMR), and the write operation is done by spin-transfer torque (STT) [17-19]. STT is achieved by passing a large current pulse through the device, enabling a transfer of spin angular momentum between the two ferromagnets. MTJs remain a good candidate for magnetoresistive random access memory (MRAM) [14-19].

Figure 1-1.1.1: Schematic of a typical MTJ structure. The green blocks are the ferromagnetic layers. The arrows refer to the direction of magnetization.

However, with time, researchers realized a crucial difficulty in play for MTJs: Switching current density vs. thermal stability [20]. The critical switching current density is given by

$$J_c = \frac{\alpha e M_S H_K V}{\hbar P}, \qquad (1\text{-}1.1.1)$$

where α is the damping constant, M_S is the saturation magnetization of the FM, H_K is the anisotropy field, V is the volume of the FM, and P is the spin polarization of the FM. The thermal stability of the FM layer is given by

$$\Delta = \frac{K_u V}{k_b T}, \tag{1-1.1.2}$$

where k_b is the Boltzmann's constant and T is the temperature. For an ideal MRAM write operation, fast switching and low current density are desirable. The spin polarization can have a maximum value of 1. Lowering the damping constant would hinder the switching speed. Therefore, there are only two major properties to play with 1) Anisotropy constant: $K_u (\sim M_S H_K)$ 2) Volume: V. Lowering either one of these can lead to lower switching current density, but it would also reduce the thermal stability of the ferromagnet. Typically, we need a thermal stability factor of at least 60, at room temperature, to maintain the non-volatility of the FM layer [21]. Hence, there is always a trade-off between thermal stability and ease of switching. This has prompted several researchers to look for new kinds of spintronic devices.

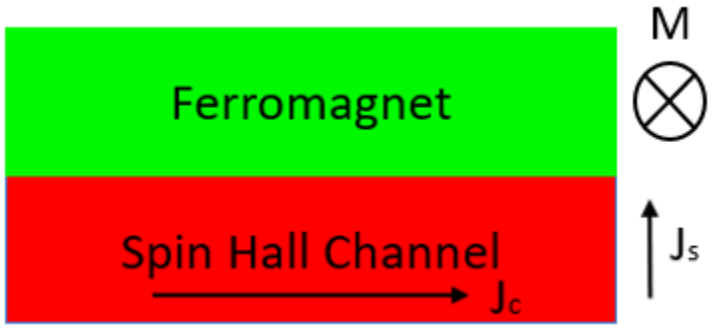

Figure 1-1.1.2: Schematic of a typical SOT bilayer structure consisting of a spin Hall channel and an adjacent in-plane ferromagnetic layer.

Spin-orbit torque (SOT) became a popular alternative, where the spin current is generated via spin Hall effect (SHE) [3,4,22-30] to perform the write operation. SOT devices require an in-plane ferromagnet to match the orientation of the injected spin. A charge current is injected into a spin Hall channel (Figure 1-1.1.2), which gives rise to a spin current in the vertical direction due to

the spin Hall effect (SHE). The spin current is then injected into an adjacent ferromagnetic layer. The injected spin current can apply torque on the magnetization of the in-plane ferromagnet and result in magnetization switching. There are four main advantages that SOT has over STT [41,48]: 1) energy consumption is lower for SOT 2) SOT has faster switching 3) dissociating the tunnel barrier from the charge current to improve the endurance 4) separation of read and write operation which allows for better engineering optimization.

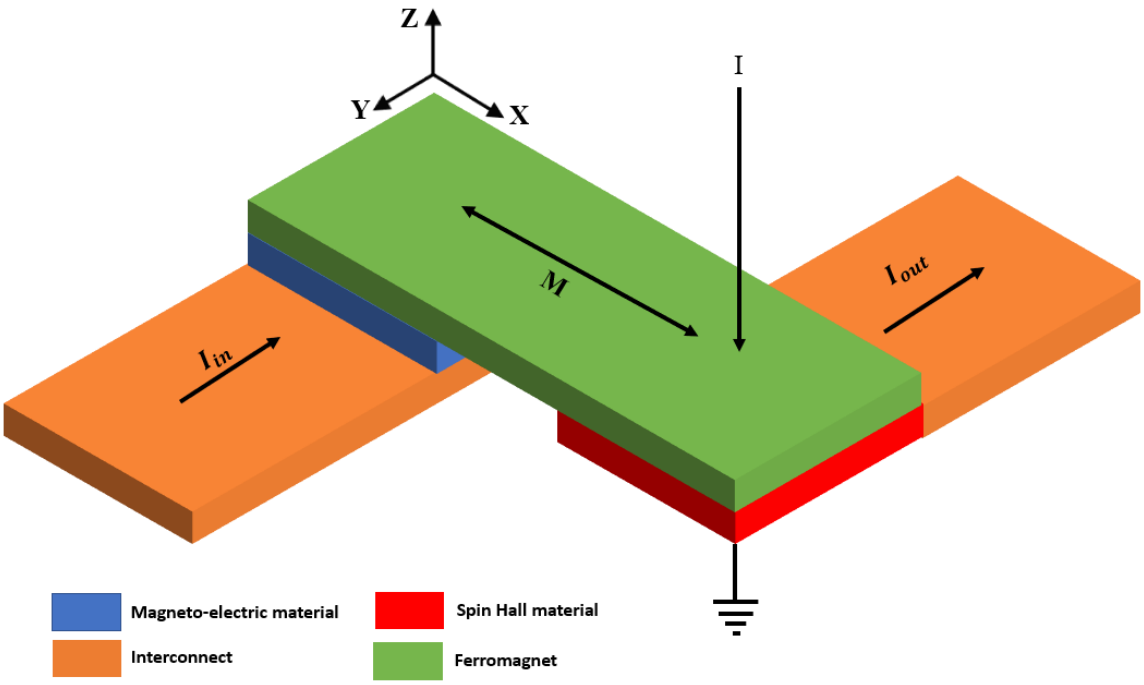

Figure 1-1.1.3: Schematic of a basic MESO device. There are four major blocks, each represented by a specific color. The input and output current directions are along the Y-axis, and the ferromagnet orientation is along the X-axis. The supply current direction is along Z-axis. The spin Hall material is grounded.

Spin logic devices have also taken center stage to keep pace with the advancement of Moore's law. One such device concept came from a group at Intel Corporation called the magnetoelectric spin-orbit (MESO) device [22]. In this device, the input side is made of a

magnetoelectric capacitor, switching the FM layer. The output side consists of a spin-to-charge conversion mechanism through inverse spin Hall effect (ISHE) to read out the magnetization state of the ferromagnet. MESO device can be used as an inverter and therefore can be used to create logic gates. Performance characterization and new MESO-based circuits were explored through a joint effort led by JP Wang and S. Sapatnekar at the University of Minnesota [73]. Figure 1-1.1.3 shows a typical MESO device schematic. The magnetoelectric input ensures that the energy consumption is low. The spin-to-charge conversion is done via ISHE, a highly scalable effect and hence desirable for logic applications. MESO device is expected to outperform (energy consumption, scaling, etc.) traditional CMOS devices [22].

1-1.2 Spin-orbit coupling

Spin-orbit coupling (SOC) is the critical piece of physics when it comes to the (inverse) spin Hall effect (ISHE). In simple terms, spin-orbit coupling is the process via which the electron's orbital and the spin angular momentum can affect each other. SOC can be described using a semiclassical, non-relativistic treatment of electronic motion, which will be enough to explain the origins of SHE.

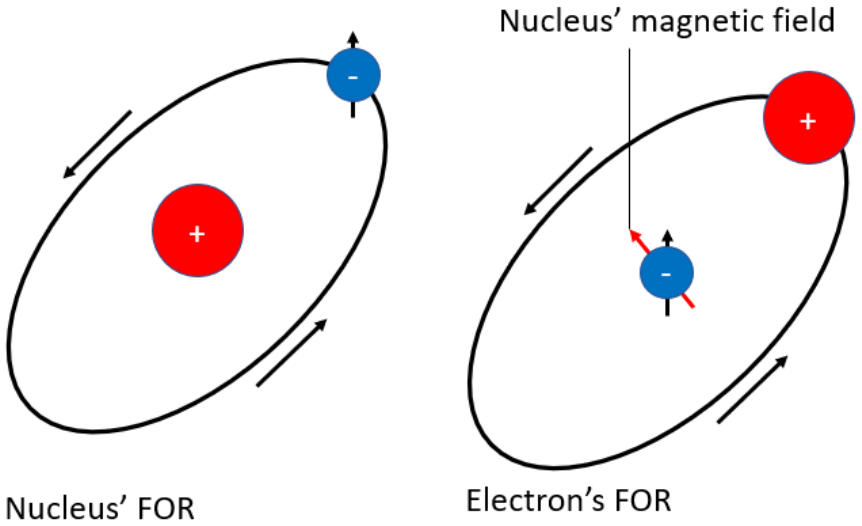

Figure 1-1.2.1: Schematic of spin-orbit interaction. The left figure shows how the system looks like when viewed from a lab FOR, and the right image shows the electron's FOR. The black arrow on the electron shows the direction of the spin of the electron. The red arrow shows the magnetic field created by the nucleus.

Figure 1-1.2.1 shows the schematic of spin-orbit interaction. In the classical treatment, the nucleus creates a magnetic field from the electron's frame of reference (FOR). This magnetic field (**B**) then interacts with the electron's magnetic moment to create an energy/Hamiltonian shift, given by

$$\Delta H = -\boldsymbol{\mu}.\boldsymbol{B}, \tag{1-1.2.1}$$

where $\boldsymbol{\mu}$ is the spin magnetic moment of the electron given as

$$\boldsymbol{\mu} = -g_S \mu_B \frac{\boldsymbol{S}}{\hbar}, \tag{1-1.2.2}$$

where μ_B is the Bohr magneton, g_S is the electron spin g-factor. The effective magnetic field generated by the orbital motion of the electron is given by [24]:

$$\boldsymbol{B} = \frac{1}{m_e e c^2} \frac{1}{r} \frac{\partial U}{\partial r} \boldsymbol{L}, \tag{1-1.2.3}$$

where $\boldsymbol{L}$ is the electron's angular momentum and U is the potential energy. Combining this with the spin magnetic moment of the electron and taking into account Thomas's interaction energy [24], we get the energy shift created from the spin-orbit coupling.

$$\Delta H = \frac{\mu_B}{\hbar m_e e c^2} \frac{1}{r} \frac{\partial U}{\partial r} \boldsymbol{L}.\boldsymbol{S}. \tag{1-1.2.4}$$

The shift in the energy level of the electron depends directly on the dot product of the orbital and spin angular momentum and the gradient of the electric potential. The electron tends to lower its energy, which depends on the relative orientation between the spin and the momentum

vector. In this situation, the scattering event of the electrons will rely on the spin of the electrons. If we flip the electron's spin, the direction of the momentum vector must also flip to maintain the lowest energy state. This is the key mechanism behind SHE and ISHE.

Furthermore, SHE can be divided into intrinsic and extrinsic types, depending on the source of the potential gradient. This potential gradient can be created by the presence of impurities, defects, etc. In such cases, the SHE is dominated by scattering events emanating from these impurity/defect points. Two well-known ones are the skew and side-jump scattering (Figure 1-1.2.2). Extrinsic SHE is expected to be a dominant force in materials with a strong disorder where scattering effects can be high, like ours.

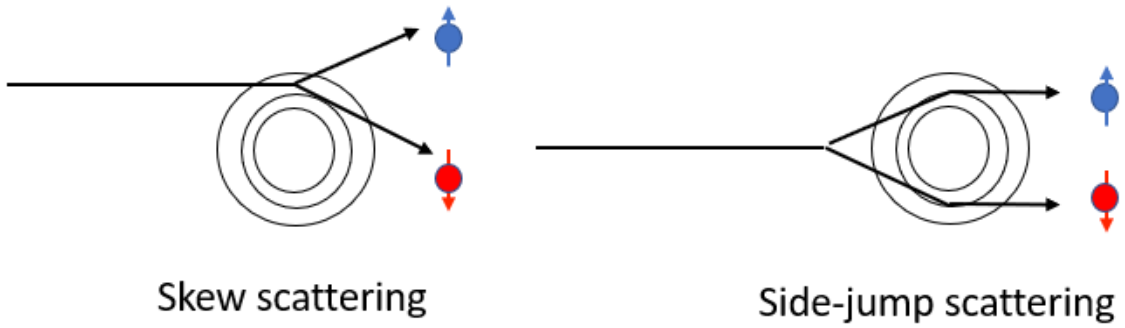

Figure 1-1.2.2: Scattering of electrons across impurities and defects due to extrinsic spin Hall mechanism. The black arrows denote the momentum vector of the electrons. The colored arrows show the direction of the spin polarization.

On the other hand, the potential gradient can also result from intrinsic effects that affect the material's band structure. The two most well-known effects are the Rashba effect and the Dresselhaus effect [25,26]. Rashba effect is a direct consequence of the breaking of structural inversion symmetry caused by the asymmetry in the crystal potential in the direction perpendicular to the 2D plane of the film [27]. This effect leads to a strong SHE effect on the film's surface and

is typically observed in exotic materials like topological insulators [25-28]. The Rashba Hamiltonian can be written as:

$$H_R = -\alpha_R(\sigma \text{ x } p).\hat{z}, \tag{1-1.2.5}$$

$$\alpha_R = -\frac{-g\mu_B E_0}{2mc^2}, \tag{1-1.2.6}$$

where E_0 is the effective electric field generated in the z-direction corresponding to the structural inversion asymmetry and m is the mass of the electron. Dresselhaus effect, discovered in 1955, is a consequence of bulk inversion asymmetry [29]. Zinc-Blende structure, which is non-centrosymmetric, is a good example of such a material system. The bulk Dresselhaus term is usually written as:

$$H_D = p_x\left(p_y^2 - p_z^2\right)\sigma_x + p_y(p_z^2 - p_x^2)\sigma_y + p_z\left(p_x^2 - p_y^2\right)\sigma_z, \tag{1-1.2.7}$$

where σ_x , σ_y and σ_z are the Pauli matrices related to the spin of the electron and p_x , p_y and p_z are the momentum in crystallographic direction [100], [010] and [001] respectively. Such effects are unlikely in disordered/amorphous films due to the absence of proper band structure [23].

1-1.3 (Inverse) Spin Hall effect

Figure 1-1.3.1 shows SHE and inverse SHE (ISHE) in a nutshell. The ability to convert charge to spin current and vice-versa is beneficial for spintronic devices and applications [6][30-37]. One can perform both SHE and ISHE based experiments to determine the efficiency of charge-to-spin conversion and vice-versa. There are many different experimental techniques designed to characterize SHE and ISHE [38-42,44]. These experiments typically require a bilayer structure consisting of the spin Hall channel and a ferromagnetic layer. However, SHE measurements for resistive spin Hall channels can be challenging. The critical problems with charge-to-spin

conversion are the dominance of thermal effects and current shunting through the ferromagnet. This can lower the impact of spin accumulation, and the thermal artifacts can completely dominate the experimental data [53]. These thermal effects are created via Joule heating and are quadratic to the injected current [71,72]. However, SHE experiments can be a great way to look at the dominance of thermal effects to the contributing signal [38,53]. We use the second harmonic method to characterize the thermal effects in the bilayer structure and compare them with the possible thermal origins of the spin pumping signal [38,42,43,53].

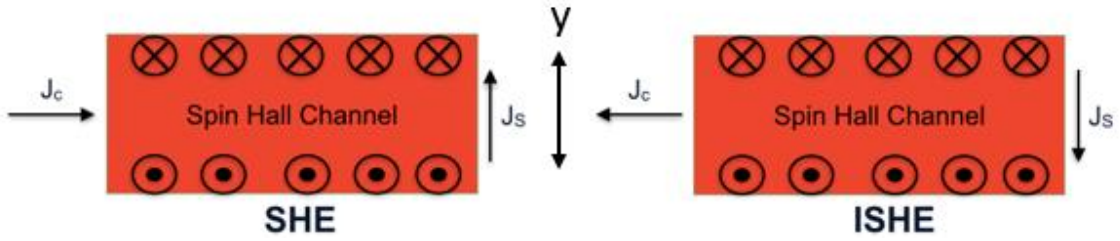

Figure 1-1.3.1: Simple schematic of charge-to-spin conversion (SHE) and spin-to-charge conversion (ISHE). The crosses and dots at the top and bottom surface depict the spin orientation of the accumulated electrons. The movement of spin current is along the y-direction

On the other hand, ISHE characterization is a viable method to deal with resistive spin Hall channels. In such systems, the spin current is injected into the spin Hall channel with the help of a FM layer. This spin current will give rise to charge current due to ISHE. Such techniques usually involve a tiny DC current and hence fewer thermal artifacts [70]. The most popular experimental approach is spin pumping, which we used for our material system [43]. There can be some issues with spin pumping of resistive spin Hall channels as it might become difficult to inject the spin current into the spin Hall channel. This can create a dominant anisotropic magnetoresistance (AMR) and anomalous Hall effect (AHE). But it can be removed by simply doing some control

experiments to exclude spin pumping signals from the FM layer. Nevertheless, spin pumping remains one of the best methods to characterize such stacks.

The key figure-of-merits are usually given by the spin Hall angle (SHA) and spin-to-charge efficiency (SCE). We make the distinction between these two parameters clear. In fact, in many cases, these two terms are used interchangeably in the spintronics community, adding to the confusion. SHA is simply defined as:

$$j_C(y) = j_s(y)\theta_{SHA}, \tag{1-1.3.1}$$

where j_C is the charge current density, j_s is the spin current density, and θ_{SHA} is the spin Hall angle. This definition of spin Hall angle comes from the assumption that we treat the interface between FM and spin Hall channel as a black-box, where we inject spin current as the input and get charge current as the output. This creates a gradient of spin accumulation in the spin Hall channel. The spin current density is maximum at the interface and decays as we move towards the bottom interface of the spin Hall channel. This thickness dependence of the spin current can be written using a simple drift-diffusion model and is given by [44, 45]:

$$j_S(y) = \frac{\sinh\left({}^{[t_{SH}-y]}/_{\lambda_{SD}}\right)}{\sinh\left({}^{t_{SH}}/_{\lambda_{SD}}\right)} J_S, \tag{1-1.3.2}$$

where $\lambda_{SD}$is the spin diffusion length in spin Hall channel and t_{SH} is the thickness of the spin Hall channel. Figure 1-1.3.2 shows how the spin current varies with the depth of the film. We have assumed a spin Hall film thickness of 8nm and spin diffusion length of 3nm.

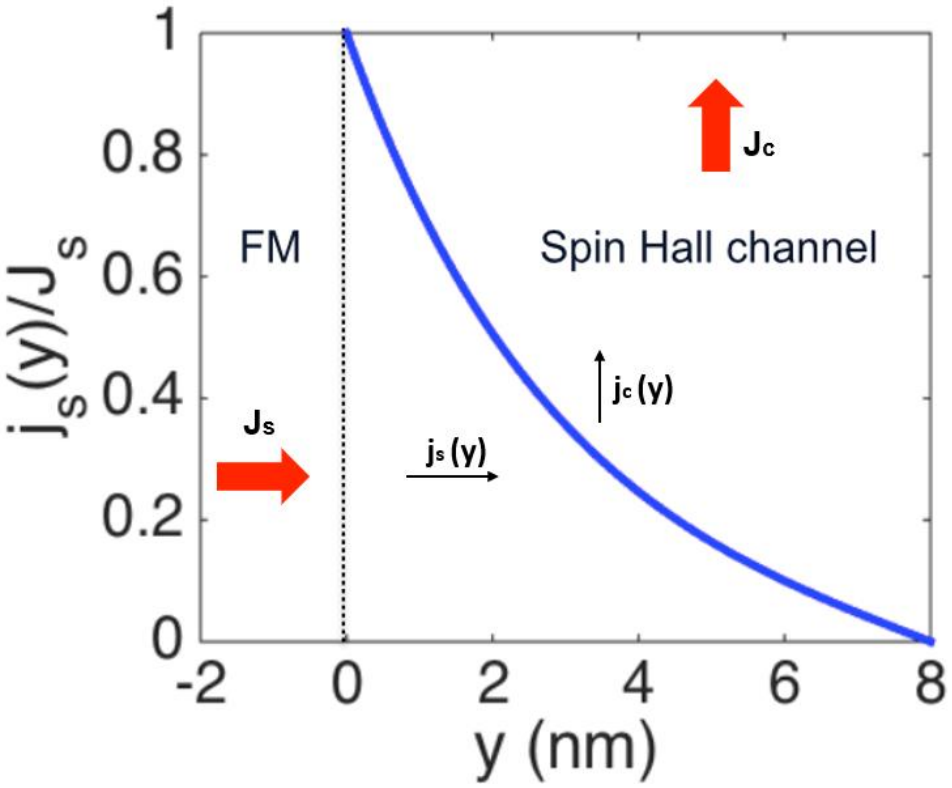

Figure 1-1.3.2: Spin current profile in a FM/Spin Hall channel bilayer structure, which shows an exponentially decaying spin accumulation in the spin Hall channel. The red arrows depict the injection of spin current and the generation of the total charge current across the entire thickness.

This gradient in spin current creates a corresponding gradient in the charge current.

$$j_C(y) = j_s(y)\theta_{SHA}, \tag{1-1.3.3}$$

$$J_C = \frac{1}{t_{SH}}\int_0^{t_{SH}} j_C(y)\, dy, \tag{1-1.3.4}$$

$$J_C = \theta_{SHA}\frac{\lambda_{SD}}{t_{SH}} tanh\left(\frac{t_{SH}}{2\lambda_{SD}}\right) J_S. \tag{1-1.3.5}$$

The total spin to charge conversion ratio becomes complicated. As a result of this, J_c/J_s is now dependent on the thickness and spin diffusion length of the spin Hall channel. This ratio is what we defined as SCE, different from SHA.

$$SCE = \frac{J_C}{J_S} \sim \theta_{SHA} \frac{\lambda_{SD}}{t_{SH}} tanh\left(\frac{t_{SH}}{2\lambda_{SD}}\right). \quad (1\text{-}1.3.6)$$

Figure 1-1.3.3 shows the thickness dependence of the SCE for two different values of spin Hall angles and spin diffusion lengths. The general trend indicates that the SCE increases with decreasing thickness. ISHE is an interfacial effect, and most of the spin-to-charge conversion occurs near the FM/spin Hall channel interface. Therefore, increasing the thickness has an averaging effect on the charge current density and thus lowers the efficiency of spin-to-charge conversion. The spin diffusion length dictates how the SCE will vary with thickness. If the spin diffusion length is low, almost all the spin-to-charge transformations will occur at the interface. Even a slight increase in thickness will drastically lower the efficiency. On the other hand, if the spin diffusion length is high, the decay in SCE will be slower with increasing thickness.

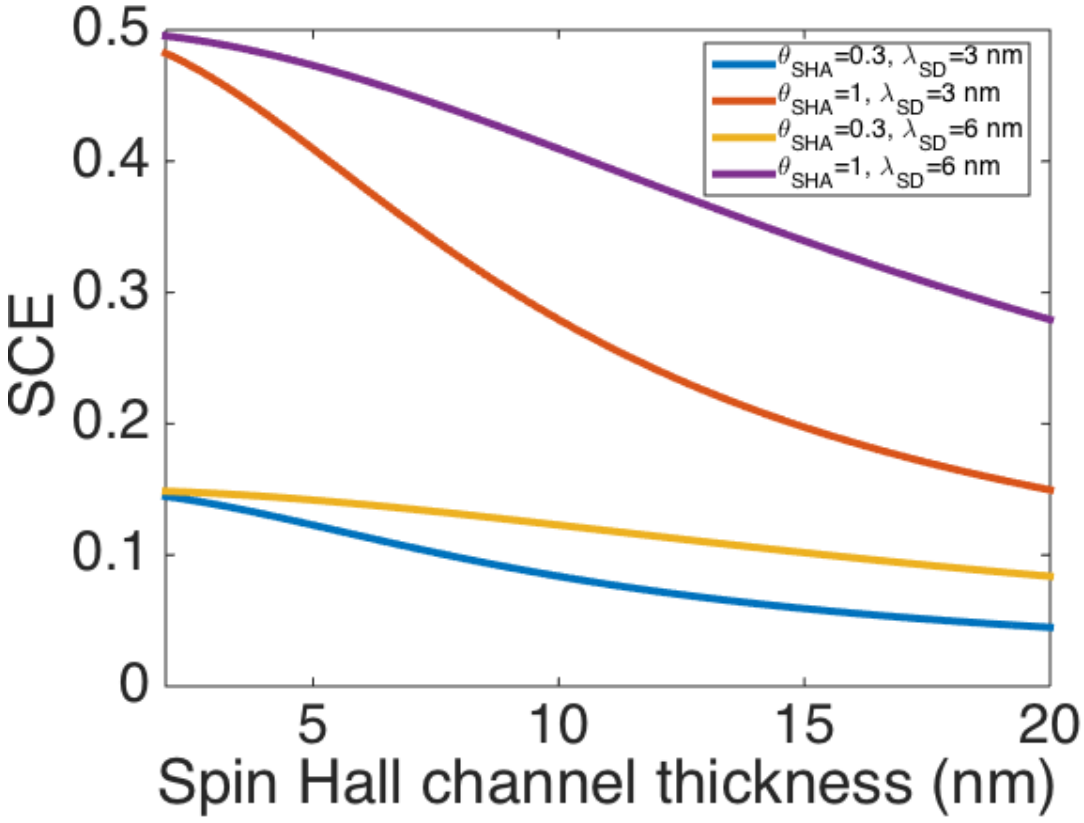

Figure 1-1.3.3: Spin-to-charge conversion efficiency (equation 1-1.3.6) as a function of the thickness of spin Hall channel for different spin Hall angles and spin diffusion lengths of the spin Hall material.

This derivation is for an ideal case where the film properties (crystallinity, roughness, etc.) are not expected to change with thickness [46]. However, things can get even more complicated in actual experiments, if the film properties show thickness dependence.

1-1.4 Magnetization read-out

Magnetization read-out is one of the essentials to making a successful spintronic device. For commercial and industrial applications, a high MR ratio is desirable. In such situations, the most

popular mechanism is tunneling magnetoresistance (TMR). Using TMR with SOT is a prevalent concept and is currently being pursued as a spintronic memory element (Figure 1-1.4.1) [47,48]. Figure 1-1.4.1 shows a typical structure of SOT-MRAM device, which contains an MTJ on top of a spin Hall channel. The spin Hall channel is used for the write operation, using SHE. The MTJ is used for read operation via TMR. However, making a TMR stack comes with several processes and device complications. It requires the deposition of additional layers of thin films and complicates the process flow with extra steps of lithography, etching, etc. Hence there is always a push to look for new kinds of MR using in-plane FMs.

Figure 1-1.4.1: Schematic of a SOT-MRAM device, consisting of a spin Hall material and a MTJ on top. The magnetization orientation of the FMs is in-plane.

Another proposed technique to detect the magnetization of the in-plane FM layer is through unidirectional spin Hall magnetoresistance (USMR) [42,49-51]. This process is very similar to current-in-plane giant magnetoresistance (CIP-GMR). The key difference being that the pinned FM layer is replaced by spin accumulation from the spin Hall channel at the FM layer/spin Hall channel interface (Figure 1-1.4.2). The spin accumulation at the interface can be calculated using the

traditional drift-diffusion model with separated spin components [49,50]. USMR has undoubtedly grown as a major proponent for in-plane magnetization read-out due to its relative simplicity in making two-terminal SOT devices. However, the MR ratio is usually small (< 0.1%), and the magnetoresistance appears as a second harmonic signal.

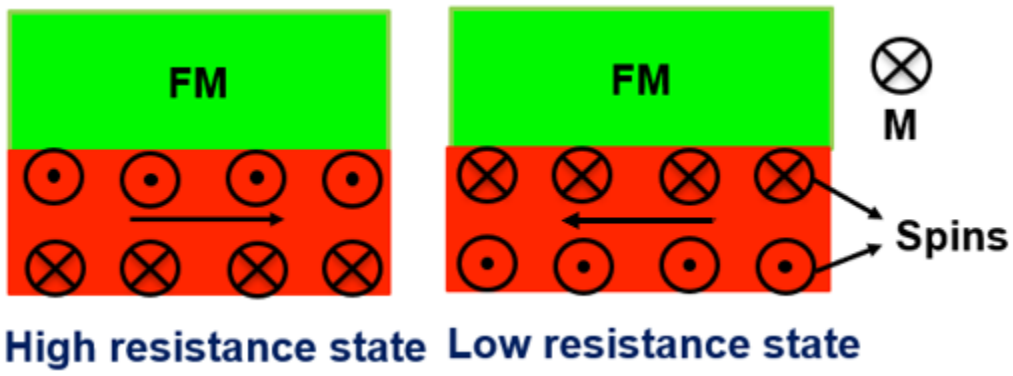

Figure 1-1.4.2: Schematic of USMR mechanism. The crosses and dots show the spin orientation of the accumulated electrons. The black arrow at the center of the spin Hall channel is the direction of injected charge current.

A third way to measure the magnetization orientation is to inject a spin current through the ferromagnet into the spin Hall channel, used in the MESO device [22]. The spin current is converted into charge current through the inverse spin Hall effect and detected as a DC output voltage (Figure1-1.4.3). A key advantage of using this technique is the simplicity and hyperbolic scalability of the spin-to-charge conversion. For a typical spin Hall material, we can assume that the spin-to-charge conversion is a consequence of the bulk inverse spin Hall effect and surface inverse Rashba-Edelstein effect (mainly observed in topological insulators). Hence the spin-to-charge conversion can be written as

$$I_C = \frac{1}{w}\left[\lambda_{IREE} + \theta_{SHA}\lambda_{SD} tanh\left(\frac{t_{SH}}{2\lambda_{SD}}\right)\right](\hat{\sigma} \text{ x } I_s), \qquad (1\text{-}1.4.1)$$

where I_C is the charge current, I_s is the spin current injected, w is the width of the nanomagnet, λ_{IREE} is the inverse Rashba-Edelstein length, and $\hat{\sigma}$ = Injected spin vector.

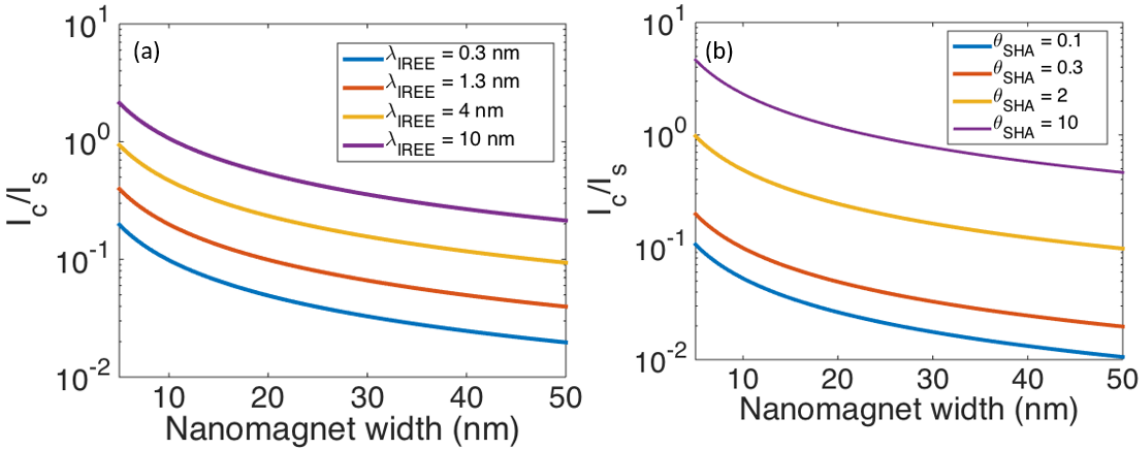

Figure 1-1.4.3: Charge-to-spin current ratio, as a function of the device width, for different inverse Rashba-Edelstein lengths (SHA = 0.3) and spin Hall angles (λ_{IREE} = 0.3nm).

Figure 1-1.4.3 shows the ratio of charge current generated to spin current injected vs the width of nanomagnet, for different values to inverse Rashba-Edelstein length and spin Hall angle. The analysis is done with a spin Hall channel thickness of 6nm and spin diffusion length of 3nm. The ratio of charge-to-spin current increases quite rapidly with decreasing nanomagnet width. The first term, of equation 1-1.4.1, corresponds to spin-to-charge conversion from the surface/interface of the film. The second term corresponds to spin-to-charge conversion in the bulk of the film. In our case, we can neglect the first term as we don't expect any exotic topological properties. Simplifying the equation 1-1.4.1 to get the ISHE voltage for a given injected supply current (I_{supply}).

$$\frac{V}{I_{supply}} = P_{FM}\rho_{SH}\lambda_{ISHE}\frac{1}{t_{SH}w}tanh\left(\frac{t_{SH}}{2\lambda_{SD}}\right) = P_{FM}\rho_{SH}\frac{SCE}{w}, \qquad (1\text{-}1.4.2)$$

where P_{FM} is the spin polarization of the FM layer, ρ_{SH} is the resistivity of the SHE layer, and $\lambda_{ISHE} \sim \theta_{SHA}\lambda_{SD}$. ISHE voltage is one of the vital figure-of-merit for spin logic applications. Based on existing literature, we require about an output voltage of ~ 100 mV for an injected current of 10 µA [22]. The spintronics community has not achieved this key figure; however, continuous research pushes this limit as close as possible to the desired value. One of the critical material parameters that can be used to tune the output voltage is the film's resistivity. We must go beyond the traditional spin Hall channels (heavy metals, topological insulators, Weyl semimetals, etc.) and look for materials in a more resistive regime (> 10000 mOhm.cm).

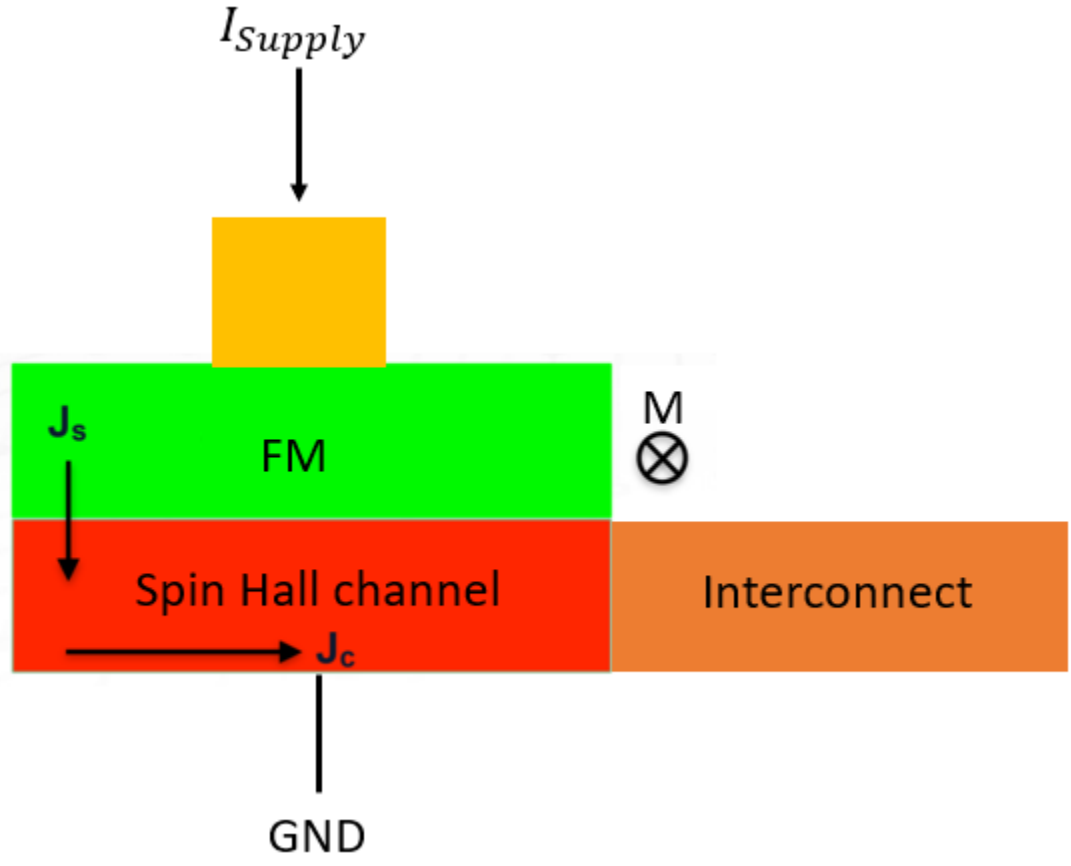

Figure 1-1.4.4: Spin-to-charge conversion system as a detection scheme. The magnetization of the ferromagnet is in-plane. The spin Hall channel is grounded.

We performed benchmarking for different spin Hall channels using the structure shown in figure 1-1.4.4. We used CoFeB as the ferromagnetic layer for the analysis. We assumed a supply current of 10 μA and spin Hall channel thickness of 6nm. Two major parameters that affect the output voltage are the resistivity of the film and the SCE. Figure 1-1.4.5 shows how different spin Hall materials compare. Heavy metals like Ta and Pt have the lowest voltage, owing to the high conductivity of the films [48,61]. The higher conductivity is desirable for MRAM applications but not for MESO and spin logic applications. The heavy metal of W has a slightly higher voltage because of the slightly higher resistivity and SCE of the beta-W phase [60]. Bi_xSb_{1-x} shows an incredibly high SCE due to its colossal spin Hall angle but lacks the resistivity to obtain a good voltage [40]. Here SC-Bi_2Se_3 stands for single-crystal Bi_2Se_3, and Poly-Bi_2Se_3 refers to polycrystalline Bi_2Se_3 [41,62,63]. $SrIrO_3$ is a new entrant into spin Hall channel materials and has shown some promise for MESO application. $SrIrO_3$ shows a good spin Hall angle (~ 0.3 -0.4) and reasonable resistivity (~ 6000 μΩ.cm) [65,66]. Gd (40%)-alloyed Bi_2Se_3(60%) doesn't have a large SCE but can generate a high voltage owing to its resistivity [43].

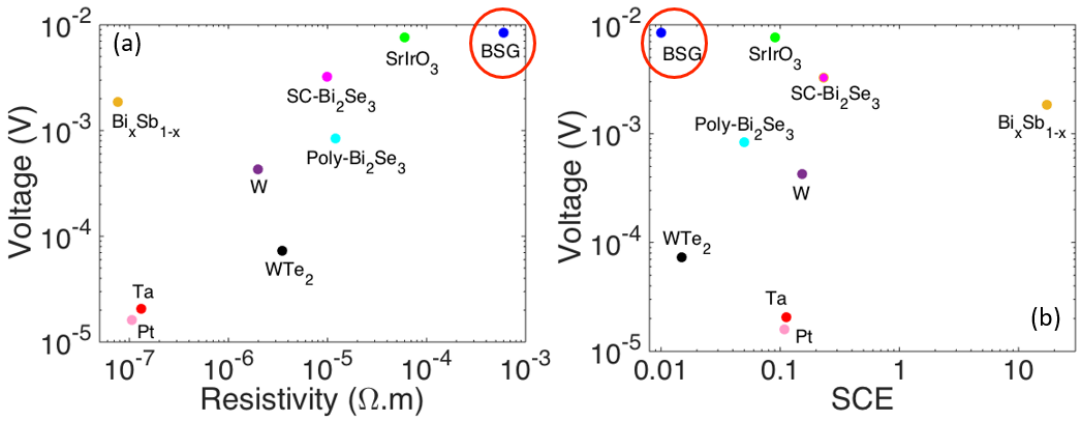

Figure 1-1.4.5: Benchmarking of ISHE voltage for different materials [32-36, 60-67] as a function of their resistivity (a) and SCE (b).

1-1.5 Spin pumping theory

Spin-pumping is one of the methods to characterize spin-to-charge conversion in a spin Hall channel [30-33, 39]. In this experiment, the FM layer (on top of the SHE layer) is excited by ferromagnetic resonance (FMR). To achieve that, we apply two different magnetic fields (Figure 1-1.5.1) in perpendicular directions. One is an AC time-varying magnetic field, and the other one is a DC magnetic field.

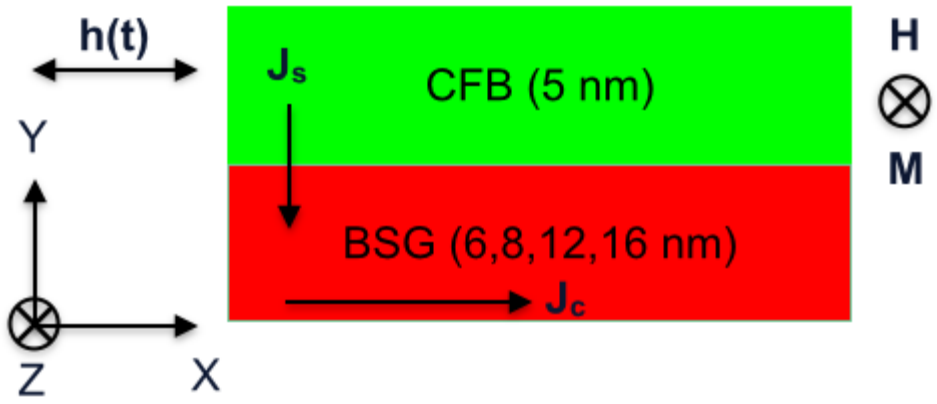

Figure 1-1.5.1: Schematic of spin pumping measurement. Magnetization of the ferromagnet is along the z-direction (along the direction of the DC magnetic field). The AC magnetic field h(t) is applied along the X-direction.

The DC magnetic field creates a precession in the FM layer with a frequency given by Larmor frequency. When the Larmor frequency equals the frequency of the AC field, the FM layer is said to be in resonance, resulting in maximum excitation of the electrons and spin injection into the BSG layer. The spin injection is given by:

$$J_S = \frac{\omega}{2\pi} \int_0^{2\pi/\omega} \frac{\hbar}{4\pi} G \frac{1}{M_S^2} \left[M(t) \text{ x } \frac{dM(t)}{dt} \right]_z dt, \quad (1\text{-}1.5.1)$$

where ω is the angular frequency at FMR, G is the real part of the spin-mixing conductance and M_S is the saturation magnetization of the FM layer, $M(t)$ is the time-dependent magnetization of the FM layer.

To obtain the term on the RHS in the square brackets, we need to first obtain the magnetizations along the x and y-direction as a function of time. The magnetization of the FM layer can be written as M(t) = M + m(t). Here M is the static part of the magnetization, and m(t) is the dynamic part of the magnetization. Using the Landau-Lifshitz-Gilbert equation, we can write the magnetization dynamics as:

$$\frac{d\boldsymbol{M}}{dt} = -\gamma M(t) \text{x } H_{eff} + \frac{\alpha}{M_S} \boldsymbol{M}(\boldsymbol{t}) \text{x } \frac{d\boldsymbol{M}(\boldsymbol{t})}{dt}, \quad (1\text{-}1.5.2)$$

where γ is the gyromagnetic ratio and α is the damping constant. The total magnetic field is a combination of the DC, AC, and the demagnetization field of the FM layer. Hence, this is given by:

$$H_{eff} = H + H_m(t) + h(t), \quad (1\text{-}1.5.3)$$

where H = (0,0,H_0), $H_m(t)$ = (0,-4π$m_y(t)$), h(t) = ($he^{i\omega t}$,0,0). For the DC magnetic field, we are only interested in the condition of ferromagnetic resonance, where the excitation is maximum, leading to highest spin current injection into the spin Hall channel. The condition for resonance is given by the famous Kittel equation [32][37]:

$$\left(\frac{\omega}{\gamma}\right)^2 = H_0(H_0 + 4\pi M_S). \quad (1\text{-}1.5.4)$$

These conditions are applied, and then solved to give us the analytical values of the x and y component of the dynamic element of magnetization of the FM layer. This was solved in Ando et al [44].

$$m_x(t) = \frac{4\pi M_S h\gamma\left\{2\alpha\omega Cos(\omega t)+[4\pi M_S\gamma + \sqrt{(4\pi M_S\gamma)^2+(2\omega)^2}]Sin(\omega t)\right\}}{8\pi\alpha\omega\sqrt{(4\pi M_S\gamma)^2+(2\omega)^2}]}, \quad (1\text{-}1.5.5)$$

$$m_y(t) = \frac{4\pi M_S h\gamma\{Cos(\omega t)\}}{4\pi\alpha\omega\sqrt{(4\pi M_S\gamma)^2 + (2\omega)^2}]}. \quad (1\text{-}1.5.6)$$

These values are then fed into equation 1-1.5.1 to give us the spin current injected from the FM layer into the spin Hall channel.

$$J_S = \frac{G\gamma^2 h^2\hbar\left\{4\pi M_S\gamma + \sqrt{(4\pi M_S\gamma)^2 + (2\omega)^2}\right\}}{8\pi\alpha^2\sqrt{(4\pi M_S\gamma)^2 + (2\omega)^2}]}\left(\frac{2e}{\hbar}\right). \quad (1\text{-}1.5.7)$$

This is one of the critical quantity that we derive from the spin pumping experiment. The other one is the charge current density, created from the device as a result of spin-to-charge conversion. This can be very simply derived from Ohm's law:

$$J_C = \frac{I}{A} = \frac{V}{RA}, \quad (1\text{-}1.5.8)$$

where *R* is the resistance of the device and *A* is the cross-sectional area. This is then combined with the spin current density derived from the spin pumping results to obtain SCE ($\sim J_c/J_s$).

1-1.6: Second-harmonic theory

The second harmonic technique is another well-known technique used for the characterization of spintronic devices [38,42,43,49,51,53]. The bilayer structure (FM/Spin Hall channel) is fabricated into Hall bars. An AC current is injected through the main channel of the Hall bar, with a specific frequency (ω), and the second harmonic Hall signal is detected. An external in-plane magnetic field (H_{ext}) is also applied at a given in-plane angle (θ).

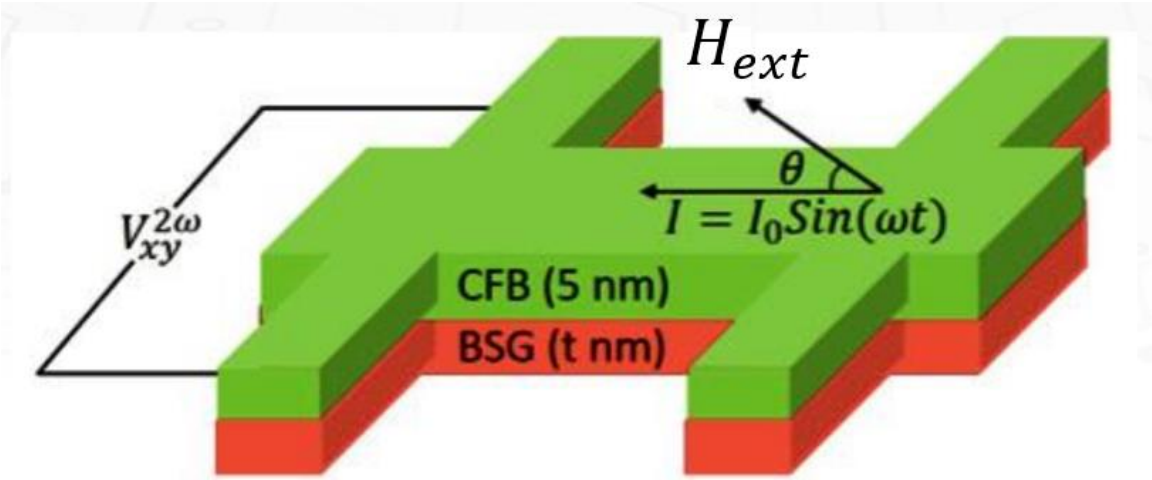

Figure 1-1.6.1: Schematic of second harmonic measurement. The angle θ is the in-plane angle between the current and the external field.

The second harmonic Hall signal mainly consists of two major physics: 1) SOT 2) Thermal effects. The SOT arises due to the torque applied by the spin current on the magnetization of the FM. For this system, the current flowing through the spin Hall channel can produce two different torque components: a field-like torque ($\vec{m} \times \vec{\sigma}$) and a damping-like ($\vec{m} \times (\vec{\sigma} \times \vec{m})$) torque [38]. Both components depend on the relative orientation between the injected spins and the local magnetization. This gives rise to two distinct effective fields called damping-like (H_{DL}) and field-

like torque (H_{FL}). The effects of SOT are strongly dependent on the resistivity of the spin Hall channel compared to the FM layer. Typically, the SOT part is negligible when the spin Hall channel is resistive compared to the FM layer (like our material) [53]. The detailed derivation of the SOT effects on the second harmonic voltage is done in Wen et al.[38]. The thermal effects arise when a magnetic field or magnetization is applied perpendicular to the thermal gradient (created from Joule heating).

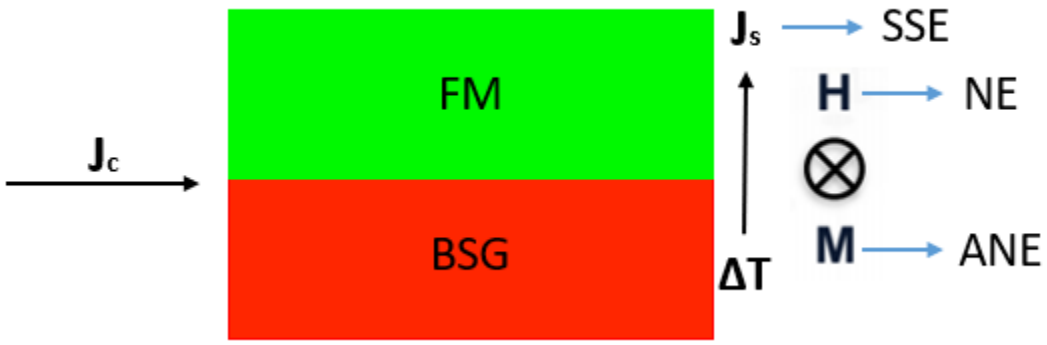

Figure 1-1.6.2: The thermal gradient generated across the thicknesses of the bilayer. The temperature gradient is created along the thicknesses of the materials. It shows the cases of NE, ANE and SSE.

The thermal effect, dependent on the external field is called the Nernst effect (NE). NE arises due to a temperature gradient across the BSG layer. This causes a second harmonic voltage, linear to the magnetic field [53]. The thermal effects dependent on the magnetization direction are mostly from anomalous Nernst effect (ANE) and spin Seebeck effect (SSE) [43]. ANE comes into play when the temperature gradient is created across the FM layer: $V_{ANE} \sim \Delta T \times M$. SSE creates a spin current along the temperature gradient direction. The second harmonic Hall voltage can be written as:

$$V_{xy}^{2\omega} = \left(\frac{H_{FL}+ H_{oe}}{H_A - H_{ext}} R_P \cos 2\theta \cos\theta + \frac{1}{2}\frac{H_{DL}}{H_K - H_{ext}} R_A \cos\theta + V_t \cos\theta + V_{NE} H_{ext} \cos\theta\right) I, \quad (1\text{-}1.6.1)$$

where H_A is the anisotropy during out-of-plane to in-plane rotation and H_K is the anisotropy field during in-plane to out-of-plane rotation. R_A is the anomalous Hall effect (AHE) coefficient, and R_p is the planar Hall effect (PHE) coefficient. The first two terms are due to SOT. The third term (V_t) is a consequence of ANE and SSE, and the fourth term (V_{NE}) is due to NE. By simply measuring the second harmonic Hall voltage as a function of the external magnetic field and the in-plane angle, we can separate each contribution to the second harmonic signal.

CHAPTER 1-2: METHODS

1-2.1 Material growth and characterization

1-2.1.1 Sputtering

Bi_2Se_3 thin film samples were grown by DC magnetron sputtering [52]. The target (material to be deposited) is kept at a negative potential, and the substrate is kept at zero potential (can be floating too). Argon gas is used as the plasma gas due to its inert properties. Under the application of a voltage, the electrons near the sputtering target are accelerated towards the wafer surface. These accelerating electrons are energetic and collide with the Ar atoms present in the chamber. These collisions between electrons and the Ar atoms lead to a transfer of energy, thereby exciting the Ar atoms and ionizing them. These ionized gaseous Ar atoms are then accelerated towards the target. Upon collision with the target, the Ar ions remove/sputter target atoms. These target atoms then fly across the chamber and settle down on the wafer/substrate.

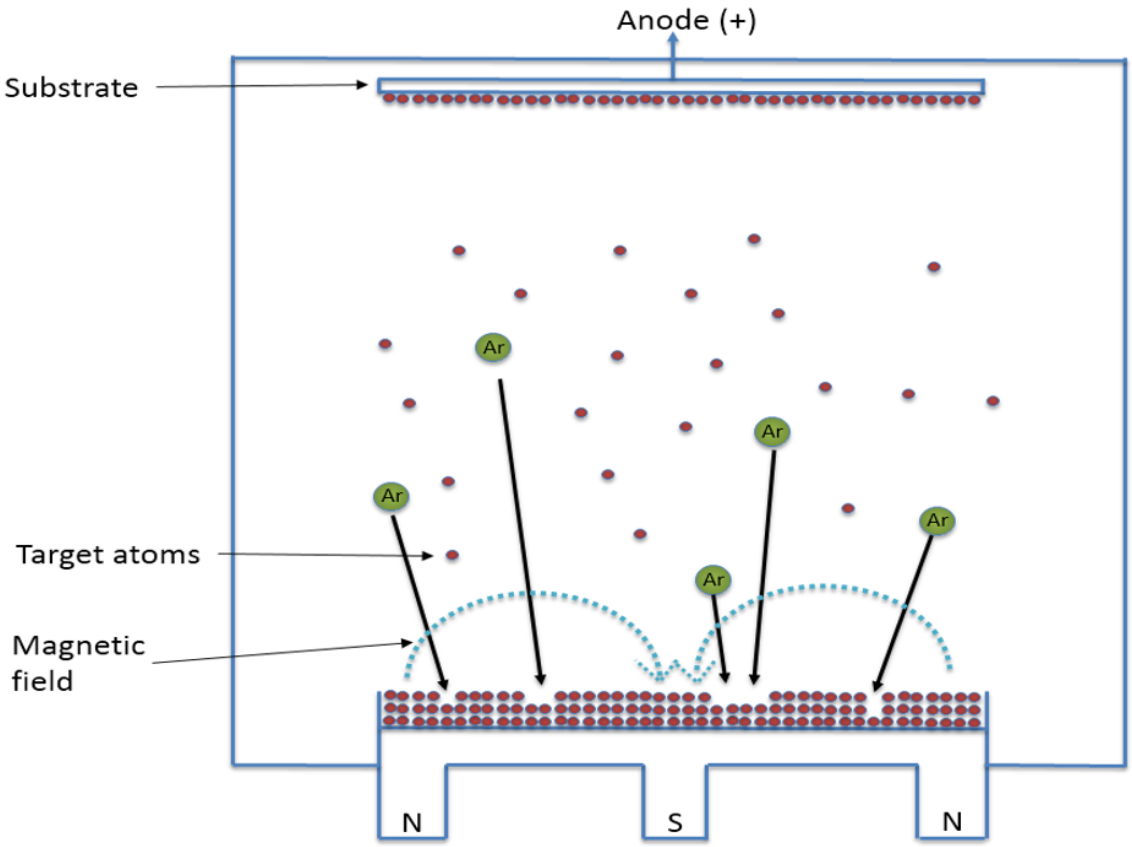

Figure 1-2.1.1: Schematic of magnetron sputtering. “N” and “S” refers to the north and south pole of the target gun magnet.

Several key factors affect the quality of the thin films. One major parameter used in vacuum processes is the mean free path of the sputtered target atoms compared to the characteristic dimension of the chamber.

$$R = \frac{Mean\ Free\ Path}{Characteristic\ Diemsion}. \qquad (1\text{-}2.1.1)$$

This is strongly dependent on the operating pressure inside the deposition chamber. Some deposition systems like molecular beam epitaxy (MBE) have a mean free path in the same order as the dimension of the chamber. This results in extremely high-quality epitaxial films. Typically, in

the sputtering process, the chamber pressure is high enough to have several collisions between the target and the substrate. Figure 1-2.1.1 shows a schematic of a simple magnetron sputtering system. Magnets are placed startegically to improve the sputtering yield. These magnets create a magnetic field that is used to confine the Ar plasma near the sputtering target.

The alloys of Bismuth Selenide with Gd are done by using layer-by-layer co-sputtering. In co-sputtering, two different targets (made of different materials) are sputtered in a layer-by-layer fashion. This creates a very intermixed thin film. The schematic of co-sputtering is shown in Figure 1-2.1.2.

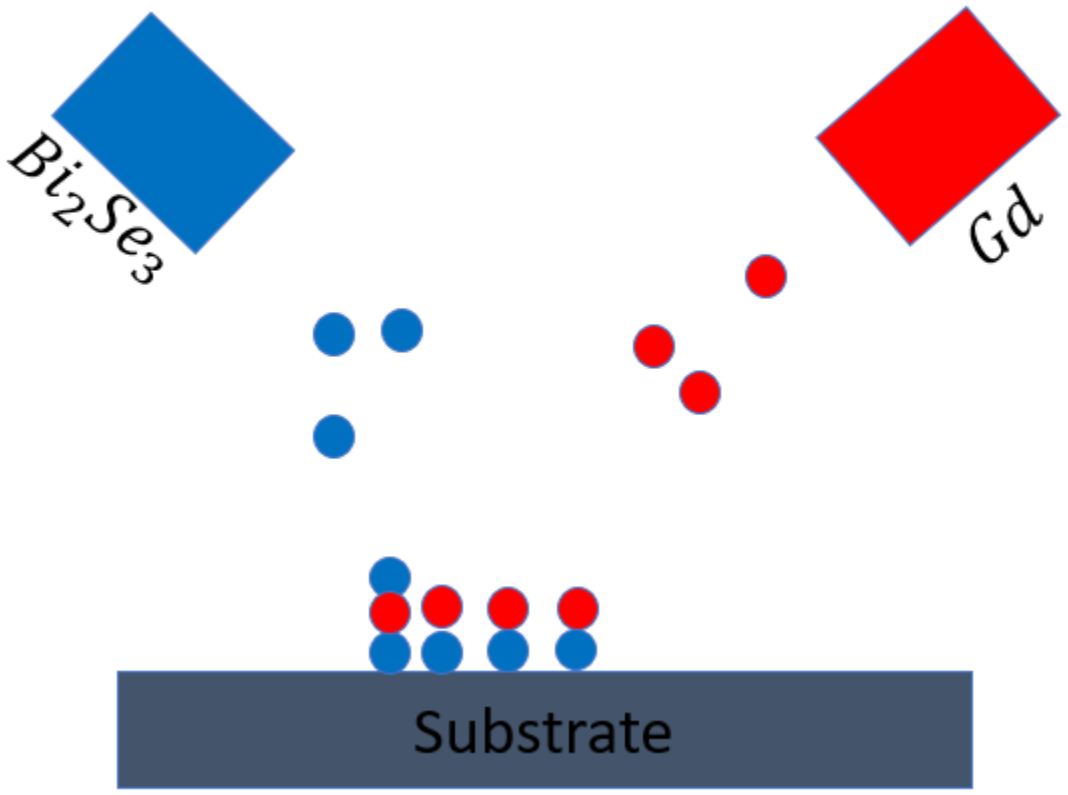

Figure 1-2.1.2: Schematic of layer-by-layer co-sputtering for gadolinium and bismuth selenide.

1-2.1.2 Transmission electron microscopy

Jason Myers did TEM and related characterizations (EDX, EELS, SAED) for the Bi_2Se_3 sample and our French collaborators (Yuan Lu et al.) for the Gd-alloyed Bismuth Selenide samples.

Electrons have smaller wavelengths than optical light. They can give us resolutions of atomic scales. These electrons are accelerated and transmitted through thin films. They are scattered by the atomic mass centers giving us the atomic-scale images of the film. The scattering process is further complicated because some scattering events can lead to the release of electromagnetic radiation (in the form of X-rays). These X-rays are then detected, which correspond to the chemical fingerprint of the material. This process is called energy dissipative X-ray spectroscopy (EDX/EDS).

As these electrons pass through the film, they can get diffracted and create a diffraction pattern (similar to X-ray diffraction). These diffraction patterns and their sharpness can be used to obtain crystallographic information about the thin film. This process is called selected area electron diffraction (SAED).

1-2.1.3 Rutherford backscattering

Rutherford backscattering (RBS) is a non-destructive technique to measure the atomic concentration of a material. Ionized He ions are transmitted through the material, which collides with the atoms present in the material. The collision allows some of the He ions to back-scatter. These backscattered He ions give us the atomic concentration of the material. The kinematics of the ionized He can be derived by using simple equations of kinematics [69]. The energy of the He

ions is reduced by the kinematic factor (k) after undergoing collision. The kinematic factor will depend on the masses M_1 (incident) and M_2 (target) as well as the angle of scattering (θ) [69]:

1-2.2 Device Fabrication

1-2.2.1 Lithography

Optical lithography was used to pattern the structures. The photoresist was coated through the spin coating (4000 rpm for 30 secs). This was followed by a soft bake done at 100 C for 60 secs. UV light was exposed for 5 secs, to create a chemical reaction in the photoresist. This chemical reaction changes the solubility of the photoresist exposed to UV light. Following that, photoresist development is done by immersing the exposed substrate in an alkaline developer for 30 secs. This keeps the photoresist intact in the required region, and the photoresist from the other areas is dissolved.

1-2.2.2 Etching

Ion milling was used to etch thin films and substrate. In an ion mill system, Ar ions are created through a high voltage plasma. These Ar ions are then accelerated towards the substrate holder. The Ar ions interact with the film, removing atoms and thereby etching the thin films. The key advantage of ion mill is that it is an entirely physical process and doesn't involve any chemistry to remove thin films. There are two major consequences of this: 1) The process has very low selectivity. This means that the etching rate is relatively independent of the film/atoms being etched. 2) The etch process is highly anisotropic. This results in almost no undercut

1-2.2.3 E-beam evaporation

E-beam evaporation was used to deposit contact metals. Typical contact stack is Ti (10nm)/Au (100nm). In e-beam evaporation, a Knudsen cell acts as the source of the material/film to be deposited. The Knudsen cell is heated using a very focused beam of electrons. The heating is done till the boiling point of the material to be deposited. Once heated, the material evaporates from the Knudsen cell and deposits on the wafer, giving us a thin film.

1-2.2.4 Process flow

The fabrication process flow for the spin pumping devices is divided into three major steps. In the first step of the patterning process, we pattern the films to create the first structure. This involves doing a round of photolithography followed by an ion mill to etch the films, thus making the first patterned structure of the thin films we will measure in the spin pumping experiment (Figure 1-2.2.1).

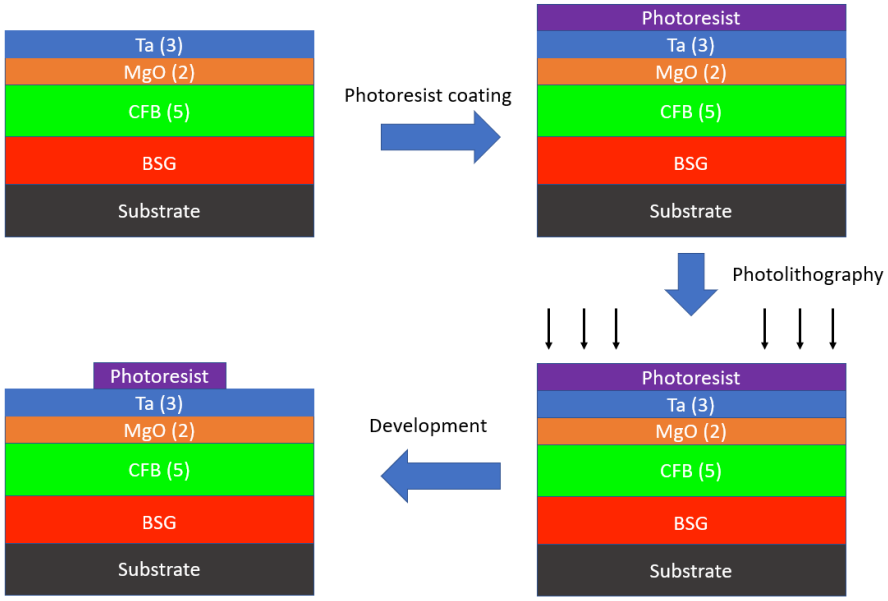

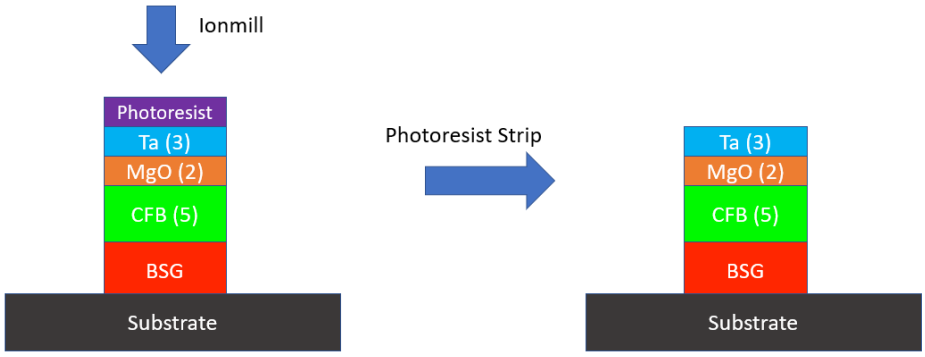

Figure 1-2.2.1: Process flow of the first step of the patterning process.

Step 2: In the second step, we do another layer of photolithography and deposit ~ 55nm SiO_2 layer via sputtering (Figure 1-2.2.2). This oxide layer separates the film from the waveguide used to apply the RF magnetic field.

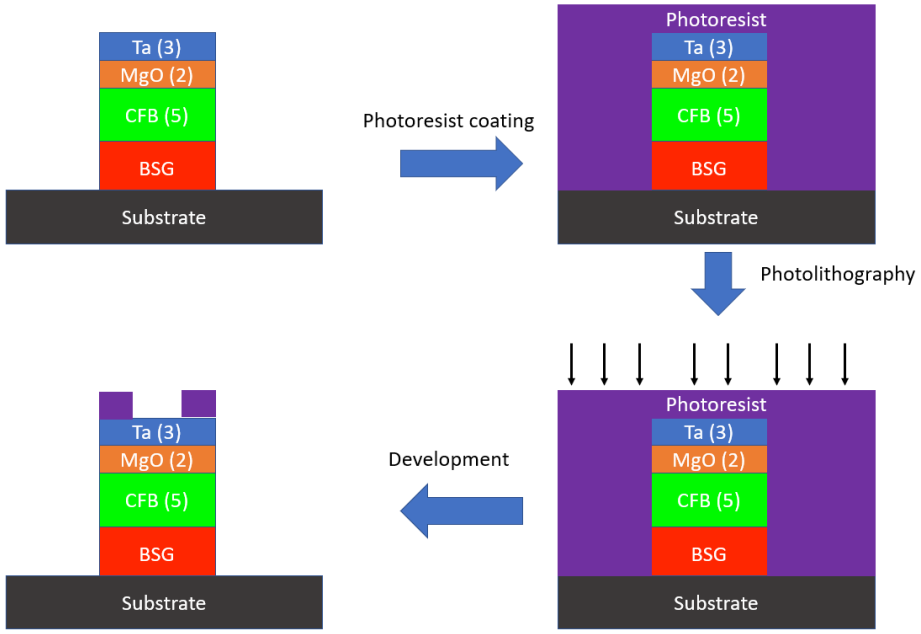

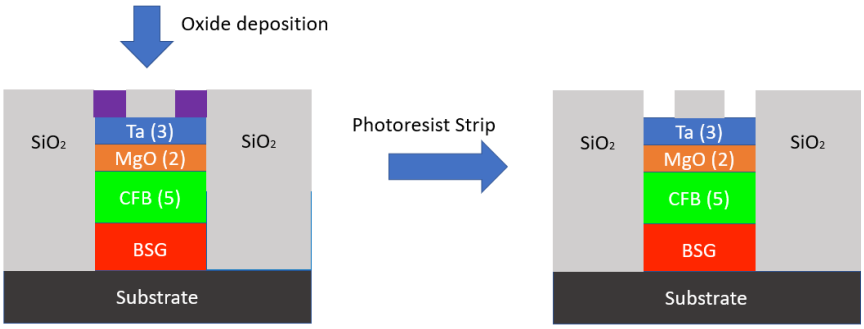

Figure 1-2.2.2: Process flow of the second step of the patterning process.

Step 3: In the third step, we do another step of photolithography followed by the deposition of metal contacts by e-beam evaporation

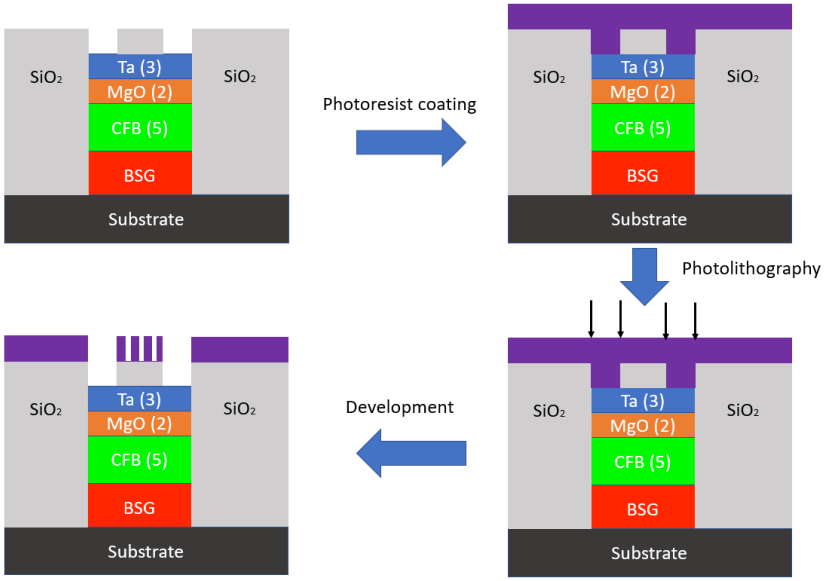

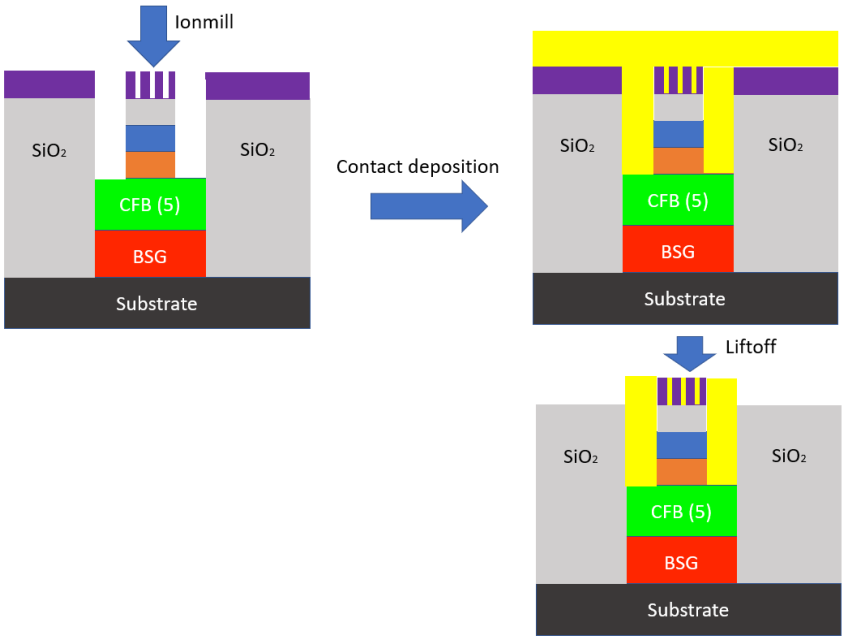

Figure 1-2.2.3: Process flow of the third step of the patterning process.

1-2.3 Electrical measurement

1-2.3.1 Setup for spin pumping

Figure 1-2.3.1 shows the experimental setup for spin pumping measurement. The signal generator is used to create an oscillating signal of a specific frequency. This oscillating signal is fed into the signal line of the coplanar waveguide. The oscillating field that can be derived simply using Ampere's law: $h_{rf} \sim I_{rf}/(2W)$, where W is the width of the coplanar waveguide [32]. An external DC field is applied to induce magnetization precession. When the frequencies of the oscillation from the DC and the AC field are equal, the ferromagnet is in resonance. This will inject a spin current into the spin Hall channel, converted into charge current via ISHE. The voltage is picked up by the voltmeter (2182). The charge current is calculated by using Ohm's law. The injected spin current is calculated using a series of steps described in the section 1-1.5.

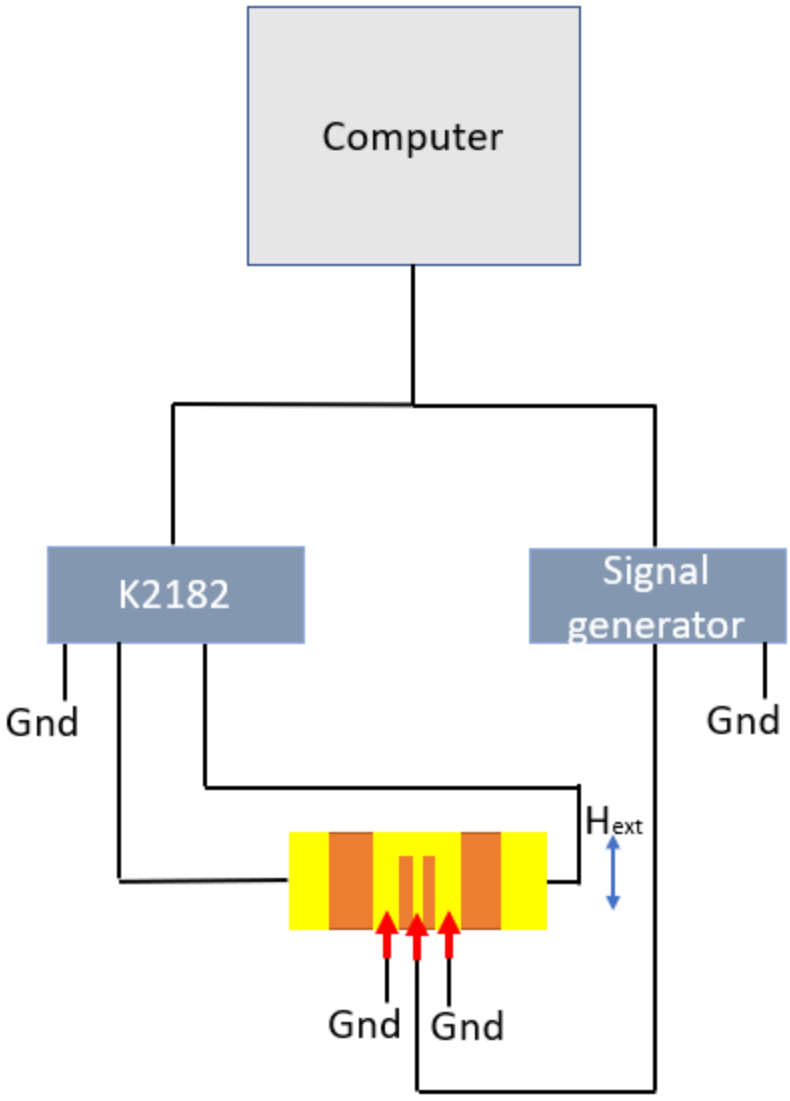

Figure1-2.3.1: Hardware testing setup for spin pumping measurement.

1-2.3.2 Setup for second harmonic

For the second harmonic, the devices are fabricated into Hall bars simply using steps 1 and 3 of the fabrication flow. Step 2 is not used since we don't need a coplanar waveguide for the second harmonic. We inject an AC current (frequency ~ 33Hz, RMS value ~ 1 mA) into the long channel

of the Hall bar. The SR830 lock-in amplifier measures the first harmonic signal. This first harmonic signal gives us a linear voltage to the injected current (classical Ohm's law). The second harmonic voltage is detected using an EGG7260, a second lock-in amplifier. The second harmonic voltage gives us the signal that has a frequency double of the injected AC current. This provides us with the voltage, which is quadratic to the injected current. A DC magnetic field is applied to the device, and the device is rotated in the presence of the magnetic field.

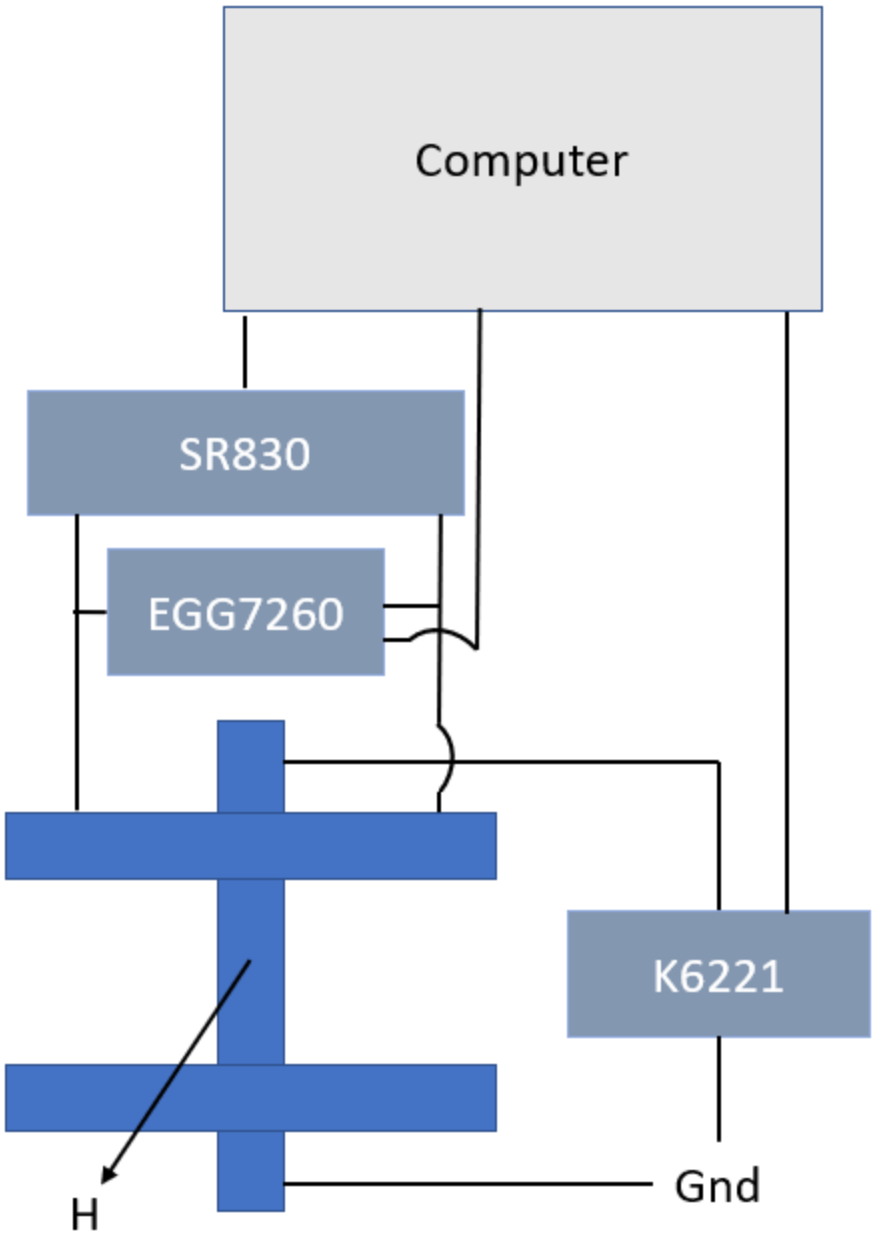

1-2.3.2: Hardware testing setup for second harmonic measurement.

CHAPTER 1-3: MATERIAL DESIGN AND OPTIMIZATION

1-3.1 Characterization of Bi_2Se_3

Previously, our group's important piece of work was DC et al [41][54]. The fundamental discovery was quantum confinement in Bismuth Selenide grains, leading to high SHE and ISHE in the films. Bi_2Se_3 films were grown at room temperature using DC magnetron sputtering on thermally oxidized Si substrates of thickness 20nm with an extra 5nm of MgO on top to prevent atmospheric oxidation. The film microstructure was characterized using (scanning) transmission electron microscopy [(S)TEM], as shown in Figs. 1-3.1.1(a) and (b); as expected, the films are polycrystalline. This polycrystallinity can be seen from the many variously oriented lattice fringes visible in Figure 1-3.1.1(b), the range of spots in the corresponding Fourier transform (FFT) [Figure 1-3.1.1(b) inset], and the rings present in the selected-area electron diffraction (SAED) pattern shown in Figure 1-3.1.1(c). The lattice spacings of the film were analyzed by measuring the frequencies in the FFT and fitting the SAED pattern via circular Hough transform. The best fits were obtained for the largest spacings, at 0.31 and 0.22nm. These matched several Bi_xSe_y phases in the ICDD PDF-2 database, but the other measured spacings (0.20, 0.14, and 0.12nm) could not be assigned to any reported structure. The higher angle rings in the SAED pattern are also substantially broadened, consistent with the disordered structure or variation in the lattice spacings between crystallites; this is further supported by streaking in the higher frequency spots in the FFT. The TEM images also showed the films to have a granular structure, wherein each grain was approximately 12–14nm long. Figure 1-3.1.1(d) shows the elemental composition of the films from

Rutherford Backscattering (RBS). There was a slightly high percentage of bismuth as compared to selenium, with a ratio of 0.44:0.56.

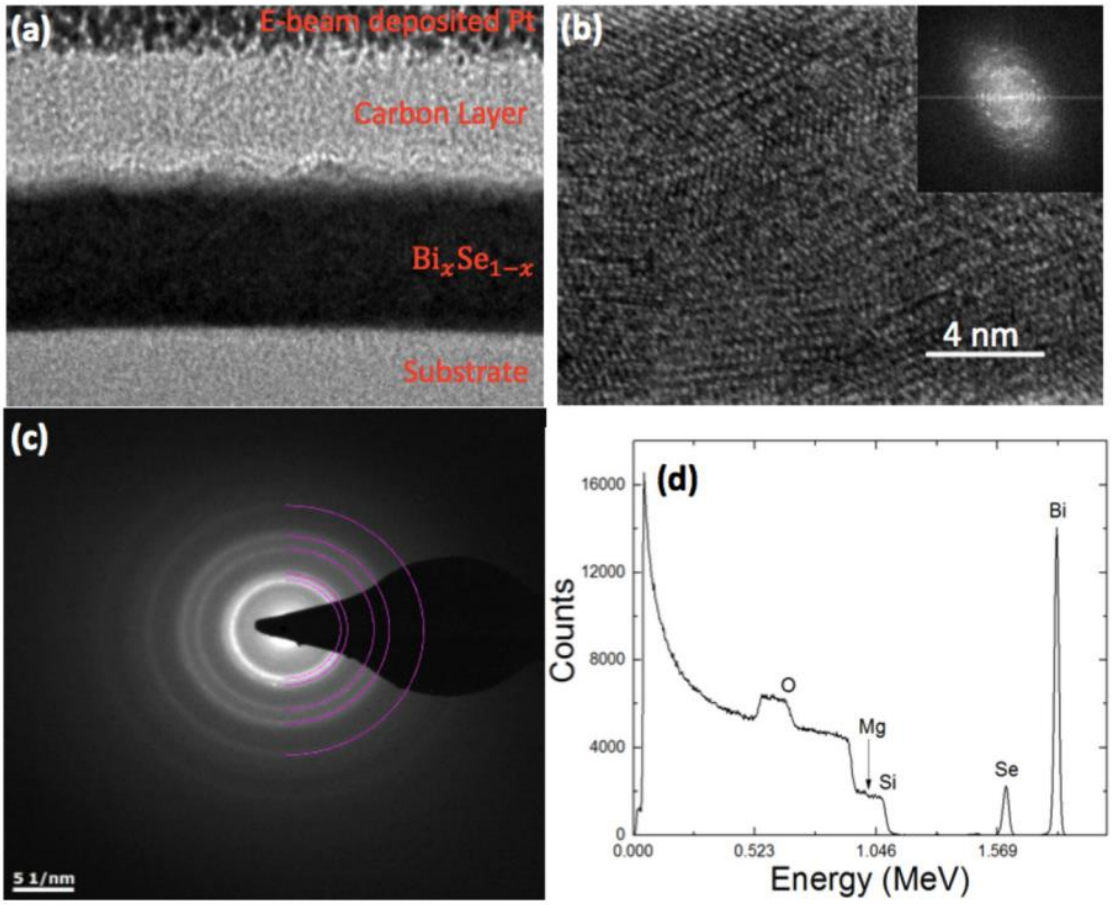

Figure 1-3.1.1: (a) High-angle annular dark-field (HAADF) scanning transmission electron microscopy (STEM) cross-sectional image at 380 000 magnification. (b) High-resolution transmission electron microscopy (TEM) image showing polycrystallinity of the Bi/Se film; inset: FFT of the TEM. (c) Selected-area electron diffraction (SAED) of the film and substrate showing diffused rings. (d) Rutherford Backscattering data of the sample. Sample stack: $Si/SiO_2/Bi_2Se_3$(20nm)/MgO(5nm) [54].

Figure 1-3.1.2 shows a continuous decrease in conductivity with temperature. This is very typical of semiconductors, suggesting a semiconducting bulk bandgap. Topological Insulators are generally known for their unique band structure, which contains a Dirac cone. However, under the effects of quantum confinement in polycrystalline films, a gap can open up, thereby creating the thermal jump of charge carriers with temperature [41]. Mahendra DC carried out several spin transport characterization on this film and found a high SHE and ISHE [41,59,62,63]. The result was attributed to quantum confinement effect inside the polycrystalline grainsof the topological insulator [41]. DFT calculations showed the presence of lowly dispersive bands that are created due to quantum confinement. These bands contribute to high SHE across the edges of the grains.

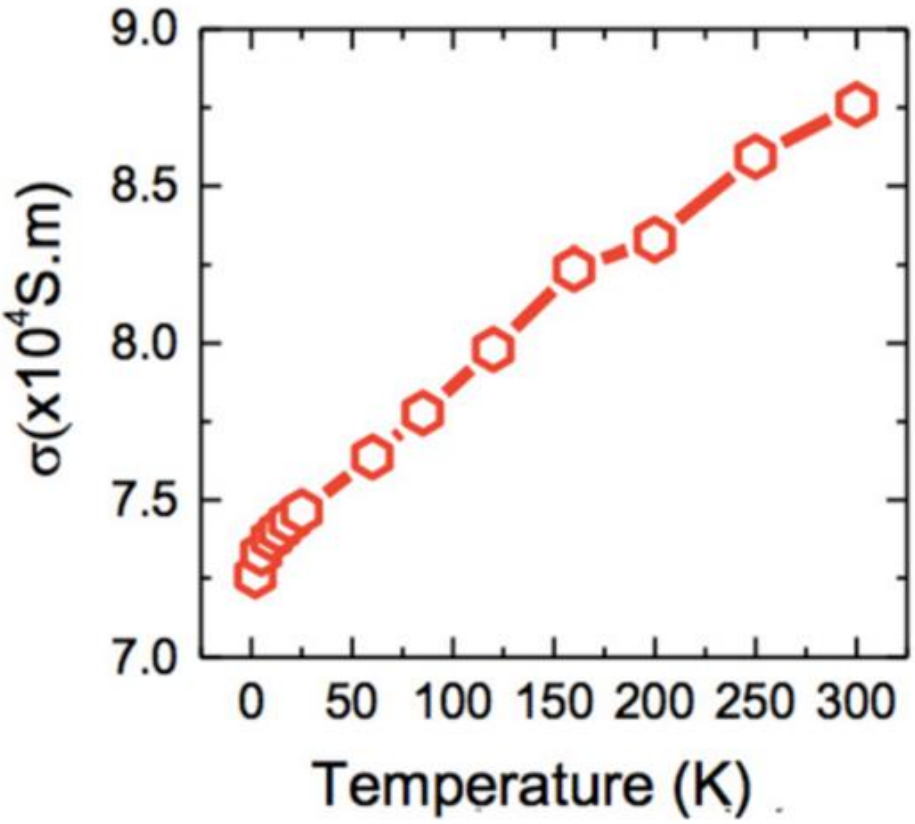

Figure 1-3.1.2: Conductivity of 20nm Bismuth Selenide thin film as a function of temperature. Sample stack: $Si/SiO_2/Bi_2Se_3$(20nm)/MgO(5nm) [54].

1-3.2 Effects of Gd-alloying

To explore more resistive spin Hall channels, we start by tuning material parameters through co-sputtering. We started with Bismuth Selenide as our key material. This material has shown great promise for spin Hall and inverse spin Hall effect. We look at Gd (rare earth weakly ferromagnetic material) as the other ingredient of the co-sputtering. These films are grown on top of thermally oxidized Si substrates. We deposit a FM layer (CoFeB 5nm) with in-plane magnetic anisotropy. This stack is then capped with MgO (2nm) and Ta (3nm) to protect the stack from oxidation. The resulting film was 60% Bismuth Selenide and 40% Gadolinium. This creates a very disordered film resulting in an alloy of the two materials.

1-3.2.1 TEM and EELS characterization

The entire film samples of BSG8 and BSG16 were used for interfacial, structure, and chemical characterization. Figures 1-3.2.1(a) and 1-3.2.1(b) show the large-scale scanning transmission electron microscopy–high angle annular dark field image (STEM-HAADF) and magnified HR-TEM image of the BSG8 sample, respectively. The sample shows relatively flat and sharp interfaces in the large-scale image (Figure 1-3.2.1(a)). Figure 1-3.2.1(b) shows that the BSG and CFB layers appear mainly amorphous in feature. The bottom MgO barrier exhibits textured characteristics characterized by small nano-crystallites, while the top MgO layer appears primarily amorphous. The interface chemical distribution has been characterized by electron energy loss spectroscopy (EELS). Figure 1-3.2.1(c) displays the different element maps drawn by EELS spectrum images on the region indicated by the red dashed rectangle zone marked in Figure 1-3.2.1

(a). Figure 1-3.2.1 (d) displays the element profile, and each data point presents an average of element intensity in a zone with 10nm width and 0.5nm depth. From the chemical maps and profile, several pieces of information can be drawn. The distribution of Gd and Se are not homogenous in the BSG layer. Gd tends to accumulate towards the bottom while, on the contrary, Se tends to segregate to the interface with CFB. Gd, Bi, and Se over concentration spots are visible. The mean atomic concentration of this area was evaluated as Bi 20%:Se 40%:Gd 40%. The ratio between Co and Fe in the CFB layer was estimated to be 1:4.

\

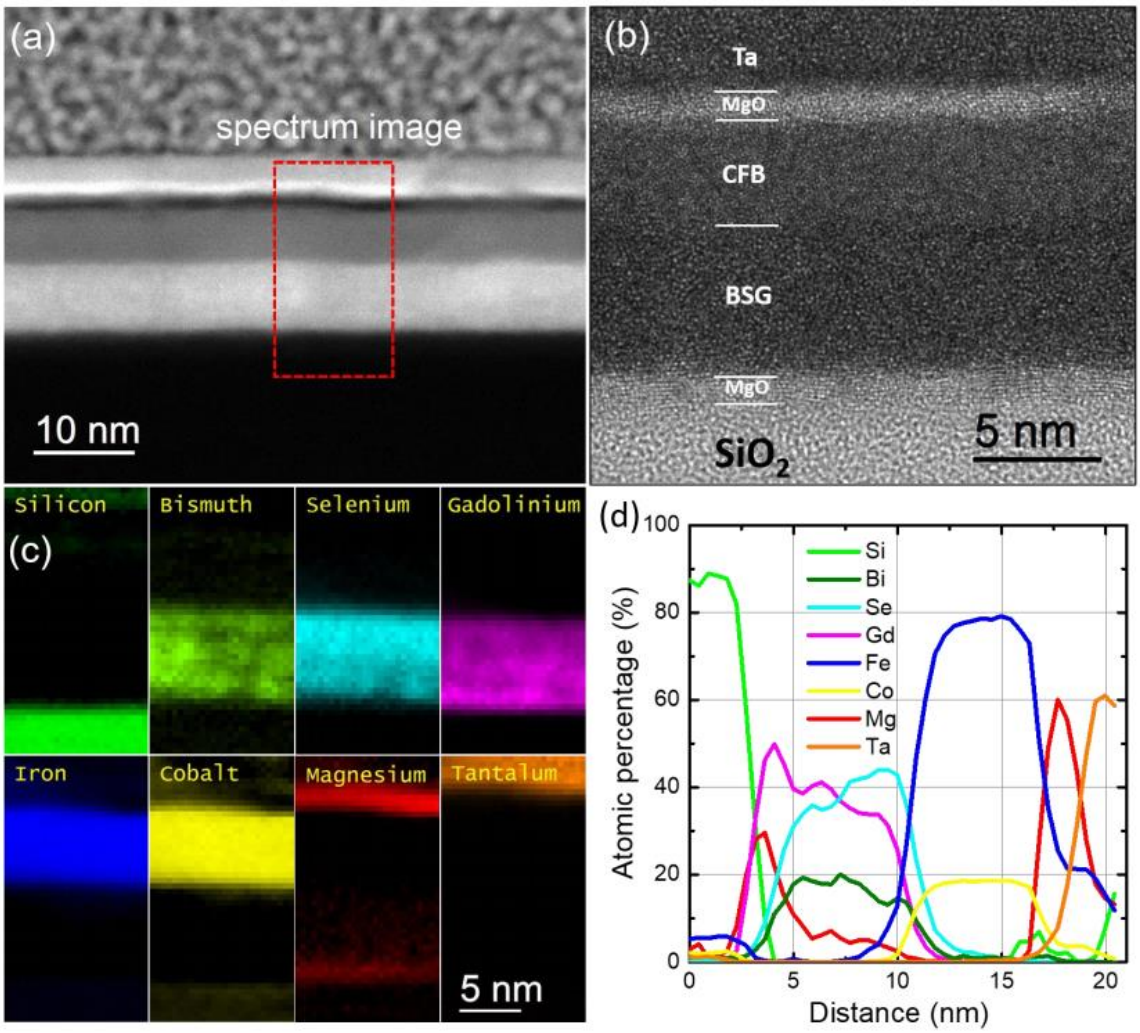

Figure 1-3.2.1: Structural and chemical characterization of BSG8 sample by TEM. (a) STEM HAADF image on the BSG8 sample at middle magnification. The red rectangle shows the region where the EELS spectrum images were recorded. (b) HRTEM image in magnified scale on the BSG8 sample. (c) Elemental maps of the stacks drawn from EELS spectrum images after quantitative processing with all the essential elements from the substrate to the capping layer. The tiny silicon signal visible in the Ta capping layer and the Mg signal inside the BSG layer is due to an artifact of processing because of the overlapping of different element edge peaks. (d) Elemental profiles across the multilayer structure drawn from EELS maps.
Sample stack: Si/SiO_2/MgO(2nm)/BSG(8nm)/CFB(5nm)/MgO(2nm)/Ta(2nm) [43].

Figure 1-3.2.2(a) shows the HRTEM image of the sample BSG16. It is found that the interface roughness becomes essential. By the guide of black dashed lines shown in Figure 1-3.2.2 (a), it is evident that the increase of interface roughness is mainly attributed to the thick BSG layer. CFB, MgO, and Ta layers follow well the morphology of the BSG layer. Some nanocrystals inside the BSG layer can be evidenced, as marked by the red dashed zones. Figure 1-3.2.2 (c-e) shows EDS element mapping images with the corresponding STEM-HAADF image in Figure 1-3.2.2 (b). From Figure 1-3.2.2 (b), many zones with brighter contrast can be observed inside the BSG layer due to an inhomogeneous chemical distribution and points out the segregation of some elements. From the chemical maps, the bight contrast zone (marked with red arrow) is identified to be Bi rich with less Se and Gd, which may also be correlated to the nanocrystals observed in Figure 1-3.2.2 (a). Therefore, during the growth of the thicker BSG layer, the enhanced segregation of chemical elements forms the Bi-rich nanocrystals, which results in a rough interface for the BSG16 sample.

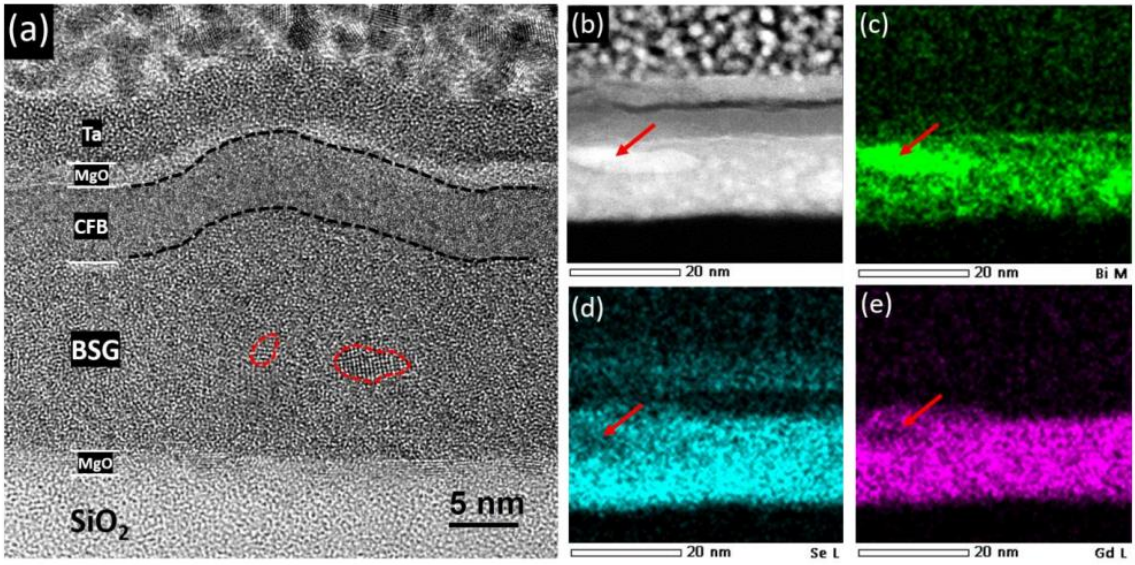

Figure 1-3.2.2: Structural and chemical characterization of BSG16 sample by TEM. (a) HRTEM image in magnified scale on the BSG16 sample. The black dashed lines guide the eyes to show the interface roughness due to the BSG layer. The red cycles show the zone where we can find nanocrystals. (b) STEM HAADF image and corresponding EDS elemental maps for (c) Bi, (d) Se, and (e) Gd. The red arrows indicate that the white contrast zone is due to the inhomogeneous element distribution with a Bi-rich character.
Sample stack: Si/SiO_2/MgO(2nm)/BSG(16nm)/CFB(5nm)/MgO(2nm)/Ta(2nm) [43].

1-3.2.2: Resistivity measurements

We performed resistivity measurements on Gd-alloyed Bismuth Selenide. BSG shows a very steady increase in resistivity with decreasing temperature. This kind of exponential temperature dependence is a sign of possible Mott variable range hopping (VRH) in the thin films during conduction [55][56]. In its simplest form, Mott hopping can be written by its characteristic temperature dependence [57][58]:

$$\sigma = \sigma_0 exp\left[-\left(\frac{T_0}{T}\right)^p\right], \quad (1\text{-}3.2.1)$$

Here σ_0 is the characteristic prefactor of VRH. The exponent *p* gives us information on the carrier conduction mechanism and may be divided into three subsets. In a bulk material, p=0.25 is attributed to a three-dimensional (3D) Mott VRH conduction wherein electron-electron (e-e) interactions are neglected. p=0.33 corresponds to a two-dimensional (2D) Mott VRH conduction in a 2D system. On the other hand, Efros-Shklovskii (ES) hopping mechanism includes long-range e-e interactions, which result in p=0.5 [58]. T_0 is the characteristic Mott or ES temperature. Figure 1-3.2.3 (b-d) display the resulting fits using ES-VRH, 2D-VRH and 3D-VRH, respectively. Rigorous data analyses, based on the residual sum of squares (RSS) for each fit, show the best fit matching with a Mott 3D VRH. This is a strong indication that a 3D Mott hopping takes place dominantly in our BSG film. The value of σ_0 obtained from the fit is $1.75\times10^{10}\Omega^{-1}\cdot cm^{-1}$. The value of T_0 obtained from the fit is 9.7×10^5K, which is relatively high, indicating that the amount of disorder in the film should be high.

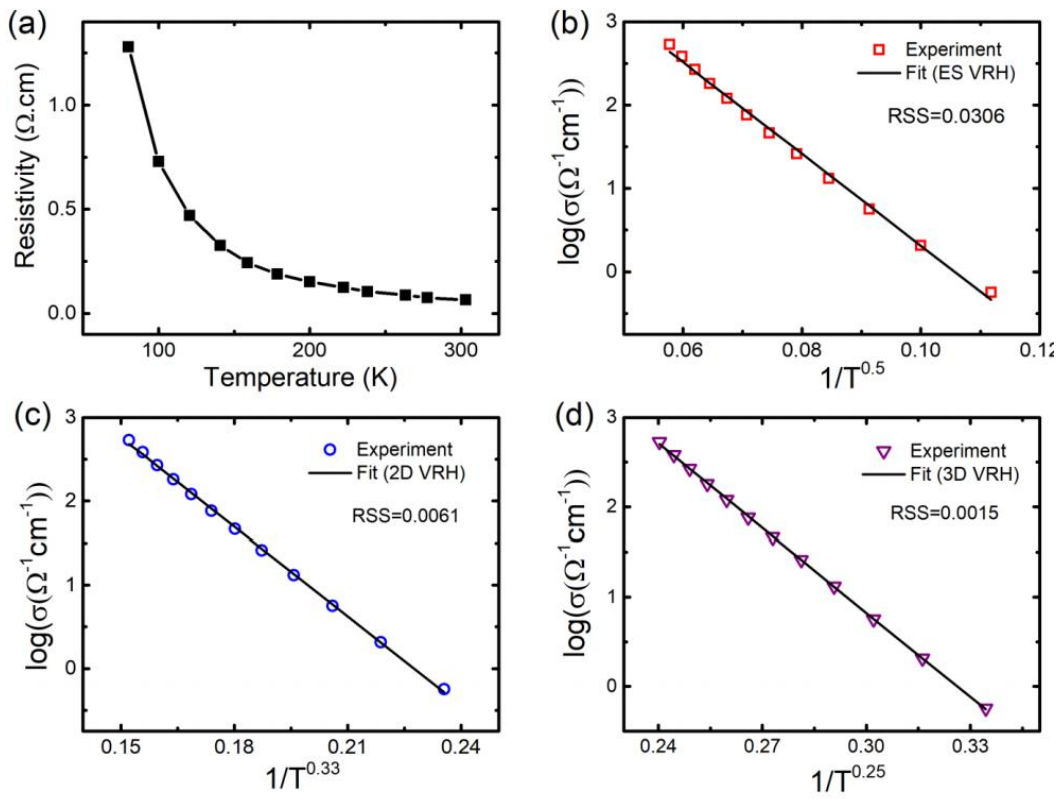

Figure 1-3.2.3: Temperature-dependent transport properties of a bare BSG sample. (a) Temperature-dependent resistivity. (b-d) Temperature vs log(conductivity) with various fits with known theoretical models: (b) ES VRH, (c) 2D VRH and (d) 3D VRH, respectively. Sample stack: Si/SiO_2/MgO(2nm)/BSG(16nm)/MgO(5nm) [43].

CHAPTER 1-4 ELECTRICAL CHARACTERIZATION

1-4.1: Spin pumping

We performed spin pumping measurements to characterize spin-to-charge conversion (ISHE) in CFB(5nm)/BSG(t = 6,8,12,16nm), hereby referred to as BSG6, BSG8, BSG12, BSG16. As described in section 1-1.5, the two major inputs to the spin pumping experiment are: 1) AC magnetic field, applied through a waveguide 2) DC magnetic field. The oscillations from AC and DC components will reach a resonance, given by the Kittel formula (equation 1-1.5.4). Under these circumstances, we get the maximum excitation of the electrons in the CFB layer, which are then injected into the FM layer. The key output is the DC voltage measured across the device created due to ISHE. Figure 1-4.1.1 shows the experimental results of spin pumping on a BSG6 sample with an AC excitation voltage of 2V (19.03 dBm).

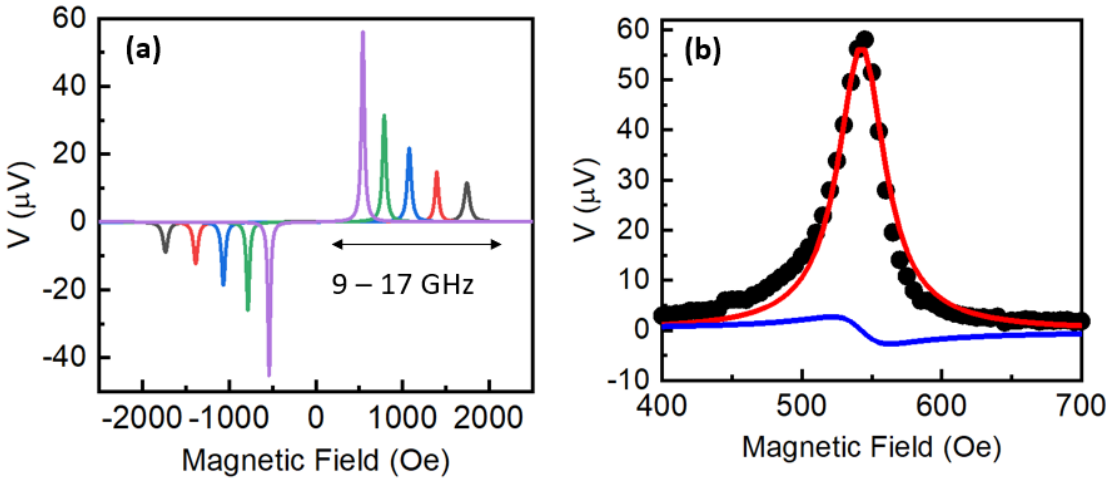

Figure 1-4.1.1: (a) DC voltage measured as a function of DC magnetic field for different frequencies of RF magnetic field. (b) Lorentzian fit of the 9 GHz peak. The black dots are the experimental data. The red curve is the symmetric component, and the blue curve is the anti-symmetric component.
Sample stack: Si/SiO_2/MgO(2nm)/BSG(6nm)/CFB(5nm)/MgO(2nm)/Ta(2nm) [43].

As we can see from Figure 1-4.1.1(a), there is a specific DC field where the output voltage is maximized for a given excitation frequency. The point of maxima corresponds to the resonance field for that given frequency. We can then extract this resonance field by combining symmetric and anti-symmetric Lorentzian fit into these peaks. The fit equation is given by [39]:

$$V = \frac{V_S \Delta H^2}{\Delta H^2 + (H_{ext} - H_0)^2} + \frac{V_A (H_{ext} - H_0)}{\Delta H (\Delta H^2 + (H_{ext} - H_0)^2)}, \qquad (1\text{-}4.1.1)$$

where V_S is the symmetric voltage, V_A is the anti-symmetric voltage, ΔH is the linewidth, H_0 is the resonance field, and H_{ext} is the external DC field.

Upon doing the Lorentzian fits, we get the symmetric and anti-symmetric voltage corresponding to the output DC voltage. And, we also get the linewidth and the resonance field, which allow us to calculate the spin current injected into the BSG layer. The key difference between the symmetric and anti-symmetric voltage is that the symmetric voltage is maximized at resonance, whereas the anti-symmetric voltage reaches zero, at resonance. The symmetric voltage is the one that contains the ISHE signal since it changes signs upon changing the magnetic field direction, which lines up with the behavior of ISHE.

Figure 1-4.1.2 shows the symmetric and anti-symmetric voltages for different excitation frequencies and thicknesses. We can see an increase in the voltage with decreasing frequency. This is a well-known behavior in spin pumping, attributed to the compensation between frequency

changes during spin pumping and the dynamic magnetic susceptibility [44]. The anti-symmetric component of the spin pumping voltage is mostly due to anisotropic magnetoresistance (AMR) and anomalous Hall effect (AHE). In a pure FM layer, only the anti-symmetric component will dominate [59].

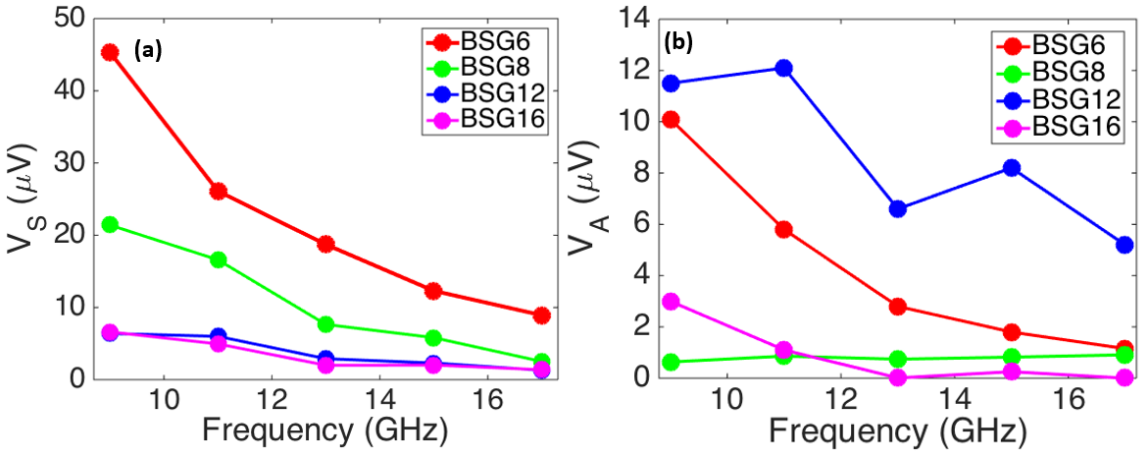

Figure 1-4.1.2: Symmetric (a) and antisymmetric (b) voltage as a function of excitation frequency for different thicknesses of the BSG layer.
Sample stack: Si/SiO_2/MgO(2nm)/BSG(6nm)/CFB(5nm)/MgO(2nm)/Ta(2nm) [43].

Once we know the symmetric voltage, we can simply calculate the charge current density from the device's resistance and cross sectional area. We use the frequency dependence of the resonance field and the linewidth to derive the saturation magnetization and the damping constant (α) of the FM layer, respectively.

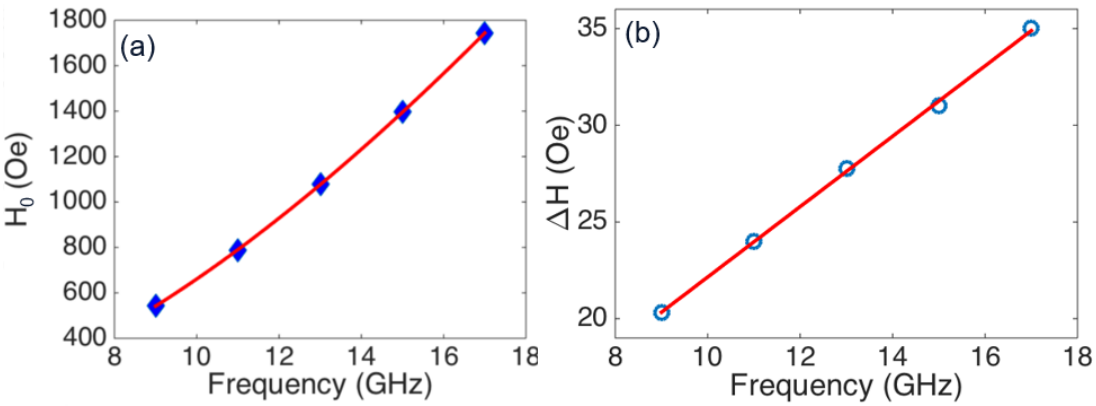

Figure 1-4.1.3: Dependence of resonance field (a) and linewidth (b) on excitation frequency, for BSG6. Sample stack: Si/SiO_2/MgO(2nm)/BSG(6nm)/CFB(5nm)/MgO(2nm)/Ta(2nm) [43].

Figure1-4.1.3 shows this dependence. The dependence of the resonance field with frequency is fitted with the Kittel formula (equation 1-1.5.4). This is used to derive the saturation magnetization of the FM layer. The dependence of linewidth with frequency is fitted by a linear curve, given as [39]:

$$\Delta H = \Delta_0 + \frac{4\pi}{\sqrt{3}\gamma}\alpha f, \qquad (1\text{-}4.1.2)$$

where α is the linewidth, γ is the gyromagnetic ratio, f is the frequency of RF field, α is the damping constant, and Δ_0 is the inhomogeneous line broadening. Figure (1-4.1.4) shows the obtained values of saturation magnetization and damping constant for different thicknesses of the BSG layer.

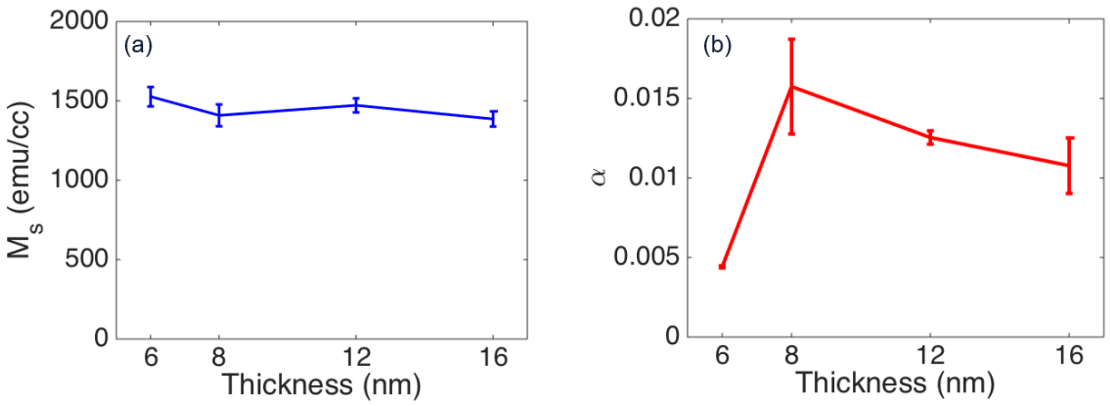

Figure 1-4.1.4: Saturation magnetization and damping constant for different thicknesses of BSG layer. Sample stack: Si/SiO_2/MgO(2nm)/BSG(6nm)/CFB(5nm)/MgO(2nm)/Ta(2nm) [43].

The values of saturation magnetization and damping constant are then combined to obtain the spin mixing conductance:

$$G = \frac{4\pi M_S t_{FM}}{g\mu_B}(\alpha - \alpha_0), \tag{1-4.1.3}$$

where α_0 is the intrinsic damping of CoFeB, g is the Lande's g-factor, M_S is the saturation magnetization, t_{FM} is the ferromagnet thickness, and μ_B is the Bohr magneton. Once we have the spin mixing conductance, we have all the required values to calculate the spin current density injected. The spin current density is combined with charge current density to obtain the spin-to-charge conversion efficiency (SCE). Figure 1-4.1.5(b) shows the final SCE obtained for different thicknesses of the BSG layer at 9 GHz excitation frequency. As we can see, the SCE shows a steady increase with decreasing thickness.

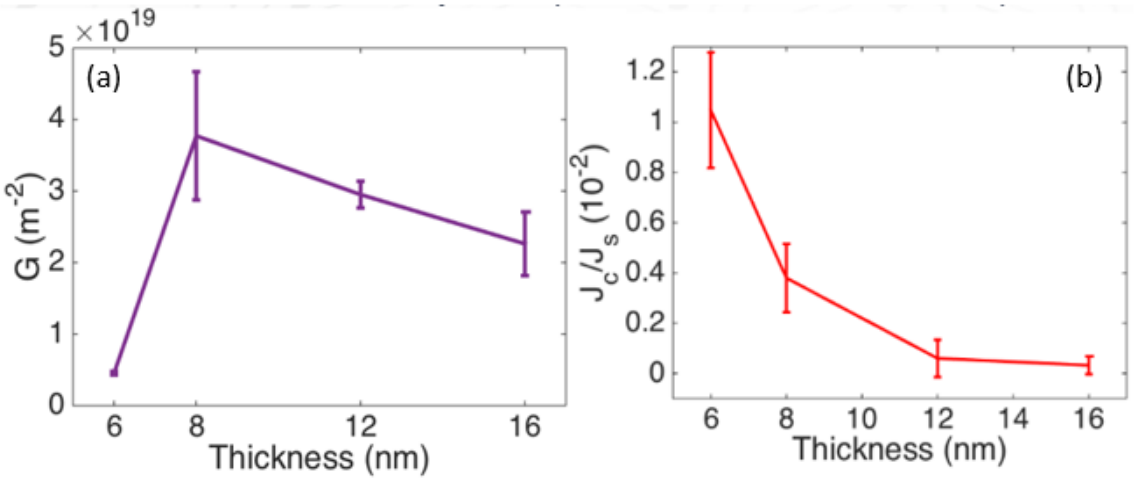

Figure 1-4.1.5: Spin mixing conductance and the SCE (9 GHz excitation frequency) of the devices for different thicknesses of the BSG layer.
Sample stack: Si/SiO_2/MgO(2nm)/BSG(6nm)/CFB(5nm)/MgO(2nm)/Ta(2nm) [43].

1-4.2 Second harmonic

We now characterize the thermal properties of our CoFeB(5nm)/BSG bilayer structures acquired by the second-harmonic Hall technique to ensure that it doesn't play a significant role in our spin pumping signal. To this end, the multilayer thin films were patterned into cross Hall bar structures with dimensions 10-20 μm wide and 30-50 μm long. Figure. 1-1.6.1 shows the schematic of the second harmonic measurement setup.

The second harmonic voltage is a combination of SOT and thermal effects (equation 1-1.6.1). The SOT is expected to be minimal due to the resistive spin Hall channel. The thermal voltage V_t is created when we have a thermal gradient perpendicular to the magnetization of the FM layer. This typically involves the ANE and SSE of the CoFeB layer. The NE is expected to create a linear dependence on the external magnetic field. We performed field sweeps to look at this possibility and found the NE to be negligible (Figure 1-4.1.6(a)). Hence, we simply neglect the

NE during our further second harmonic analysis. Figure. 1-4.1.6 (b) shows the second-order Hall signal at 3T external field at room temperature. As it can be seen, the data shows a pretty fair cosine shape that can be fitted to obtain the amplitude. Indeed, the field-like torque often manifests as a slight depression in the second harmonic Hall voltage around 90 and 270 degrees. The fitted amplitudes are then plotted against $\frac{1}{H_{ext}-H_{A,K}}$ and reported in Figure. 1-4.1.6 (c,d), further processed by a linear fitting. The slope of the linear fit allows us to determine the damping-like/field-like field, and the intercept gives out the thermal voltage contribution. The damping-like/field-like field is related to the spin current generated from the spin Hall channel: $H_{DL,FL} = \frac{\hbar J_S}{2eM_S t_{FM}}$. Here J_S is the spin current generated by the BSG layer, M_S is the saturation magnetization of the CoFeB layer and t_{FM} is the thickness of CoFeB. Using this relationship, we can calculate, in a model of a 3D (bulk) conduction for SHE, the equivalent spin Hall angle, which is defined as the ratio of the spin current generated from spin Hall channel over the charge current injected according to:

$$\zeta = \frac{J_S}{J_C} = \frac{2eM_S t_{FM} H_{DL,FL}}{\hbar J_{SH}} \tag{1.4.1.4}$$

where J_{SH} is the current density through the spin Hall channel calculated by current shunting. We have performed the angular dependent second order Hall measurement on the BSG/CFB bilayers with different thicknesses of BSG (6, 8, 12, 16nm). Figure 1-4.1.6 (f) shows the thermal voltage obtained from the fits. As expected, the thermal voltage (V_t) almost entirely dominates our second harmonic Hall voltage.

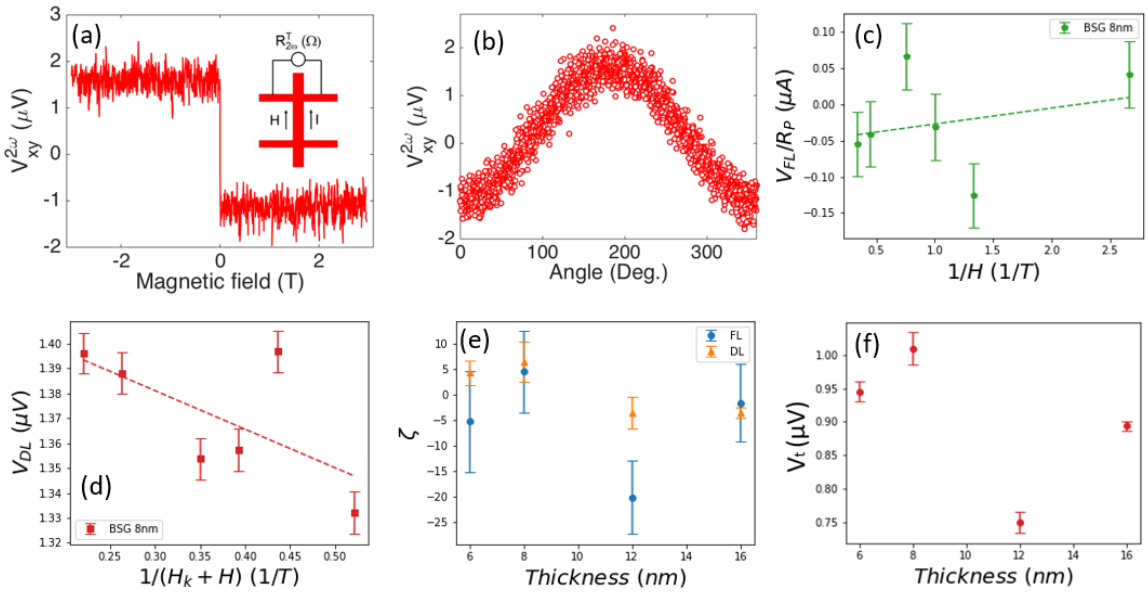

Figure 1-4.1.6: Magneto-transport characterization of spin-orbit torque. (a) Second harmonic transverse magnetoresistance response with the magnetic field at room temperature. (b) Second harmonic Hall resistance as a function of the angle at room temperature and external 3T magnetic field. (c) The amplitude of the second harmonic field-like signal as a function of $\frac{1}{H_{ext}}$. (d) Amplitude of second harmonic damping-like signal as a function of $\frac{1}{H_{ext}-H_k}$. The linear fitting allows obtaining the amplitude of damping like torque. (e) Spin Hall efficiencies as a function of the thickness of the BSG layer. (f) Thermal voltage for different thicknesses of BSG layer. Sample stack: Si/SiO_2/MgO(2nm)/BSG(8nm)/CFB(5nm)/MgO(2nm)/Ta(2nm) [43].

Figure 1-4.1.7 shows the first harmonic voltage of the same device and conditions as in Figure. 1-4.1.6. As one can observe, the thermal effects (NE, ANE, SSE, etc.) are absent in the first harmonic signal, as it doesn't show any of their characteristic angle dependence. The first harmonic voltage is typically a consequence of the planar Hall effect (PHE) present in the bilayer. This signal is susceptible to the sample orientation and tilt and will usually vary due to human error caused during sample mounting. That's why it can be challenging to obtain a perfect sinusoidal-type signal from the first harmonic. Nevertheless, the difference between the highest and lowest

first harmonic voltage will give us a good sign of how the first and second harmonic voltages compare.

$$\Delta V_{xy}^{1\omega} = \frac{\max(V_{xy}^{1\omega}) - \min(V_{xy}^{1\omega})}{2}. \quad (1\text{-}4.1.5)$$

Figure 1-4.1.7 (b) shows the difference between the maximum and minimum first harmonic voltage for different thicknesses. As one can see, it is much larger than the obtained thermal second harmonic voltage (1 μV) at 1 mA RMS current.

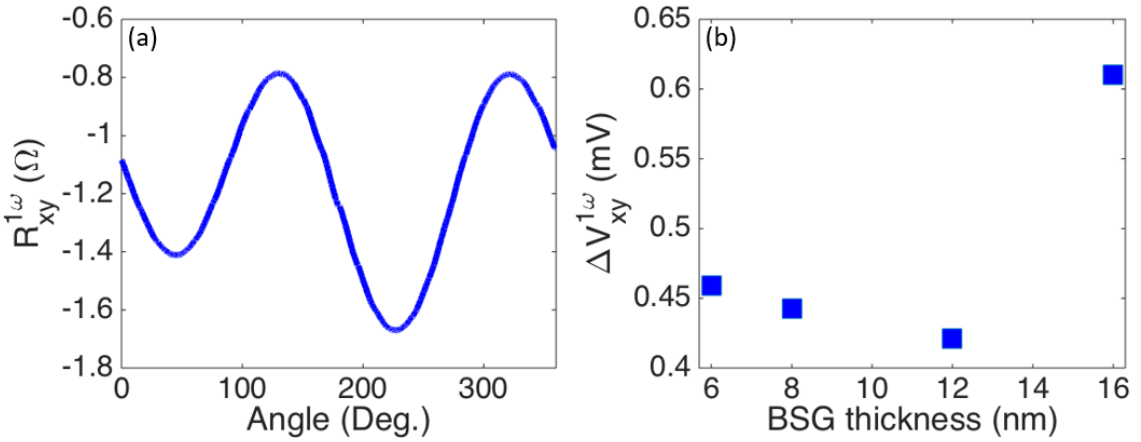

Figure 1-4.1.7: (a) First harmonic resistance as a function of in-plane angle, at 3T external field. (b) The difference in maximum and minimum first harmonic voltage for different thicknesses of BSG, at 3T external magnetic field.
Sample stack: Si/SiO_2/MgO(2nm)/BSG(8nm)/CFB(5nm)/MgO(2nm)/Ta(2nm) [43].

So far, we have looked at the Hall signals. We also look at the longitudinal first and second harmonic. Figure 1-4.1.8 shows the first and second harmonic longitudinal signals. The first harmonic is the AMR signal and is much larger than the second harmonic (thermal effects). The second harmonic longitudinal signal shows a good sinusoidal behavior.

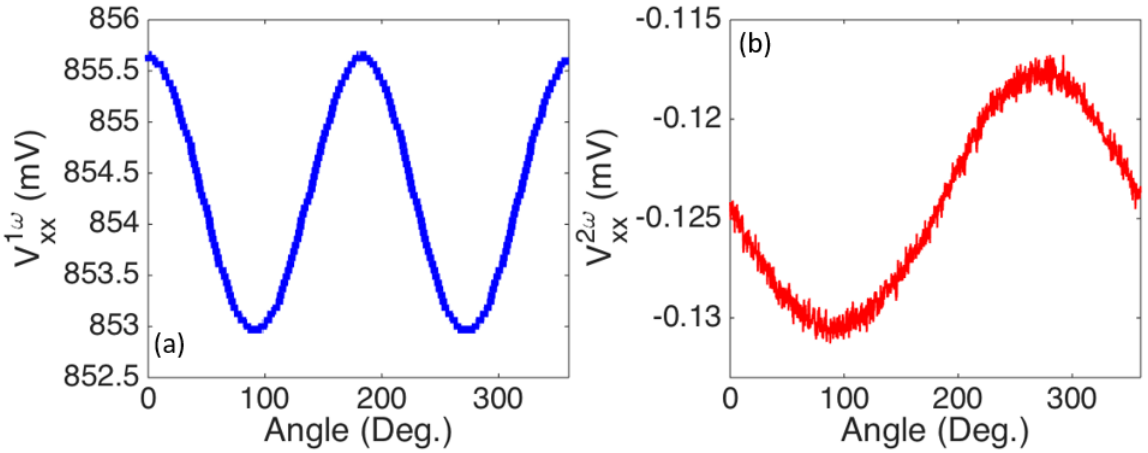

Figure 1-4.1.8: First (a) and second (b) harmonic longitudinal voltage, as a function of in-plane angle, at 3T external magnetic field.

Sample stack: Si/SiO_2/MgO(2nm)/BSG(8nm)/CFB(5nm)/MgO(2nm)/Ta(2nm) [43].

CHAPTER 1-5: DISCUSSION

We start by removing/explaining all the possible artifacts that can contribute to the DC spin pumping signal. The first significant artifact that can come into play is the spin-pumping of the CoFeB layer. To remove that, we look at the spin pumping voltage obtained for a single layer of CoFeB [59]. The signal is almost entirely made out of the anti-symmetric voltage. The spin pumping (symmetric part) is minimal (~ 4 μV) [59]. Our most resistive channel (6nm) shows a stable symmetric voltage of 45 μV, which is much greater than any possible spin pumping effects of the CoFeB layer. This points to the fact that the spin pumping of CoFeB is not a dominant signal in our spin pumping measurement.

Now, we look at possible thermal origins. Several thermal effects can come into play. The sources of the thermal effects arise from the temperature gradient created across the ferromagnet and/or spin Hall channel thickness. However, the thermal effects that do contribute to the spin pumping signal can be of three primary kinds: 1) Spin Seebeck effect (SSE) 2) Nernst effect (NE) 3) Anomalous Nernst effect (ANE). These were separated using the second harmonic. The NE is found to be small and hence neglected (Figure 1.4.1.6 (a)). The SOT contribution in the device is also negligible, which can be seen fluctuating around the value of zero (Figure 1-4.1.6(e)). This happens because the thermal effects are pretty significant in this experimental structure. These effects are created via Joule heating and scale parabolically with the current. Furthermore, the charge current is mostly shunted through the ferromagnetic layer, which is more conductive than the spin Hall channel. This means that almost all the measured voltage in the second harmonic setup is the consequence of SSE and ANE. As shown in Figure 1-4.1.6 (f), the thermal voltage (SSE and ANE) is around 1 μV.

The remaining thermal voltage (ANE+SSE) doesn't show any proper thickness dependence, unlike our spin pumping results, which increases quite heavily with decreasing thickness. This indicates that the temperature gradient doesn't vary much with the thickness of Gd-BiSe. Hence, the Gd-BiSe layer doesn't contribute too much to Joule heating. This is expected since most of the current will be confined to the FM layer due to resistivity differences. The FM layer is the only one that contributes to Joule heating. Using parallel-resistor model, with constant total injected current ~ *I*, Joule heating created due to Gd-BiSe layer is: $I_{BSG}^2 R_{BSG} \sim I^2 R_{CFB}^2 / R_{BSG}$. Similarly, the Joule heating for CFB is: $I_{CFB}^2 R_{CFB} \sim I^2 R_{CFB}$. Here we assume that ($R_{BSG} >> R_{CFB}$). This shows that the Joule heating from the CFB layer is dominant and the BSG layer doesn't play a major role. therefore showing the thickness independence. Furthermore, the first harmonic signal is much bigger than the thermal voltage and expected to dominate our spin pumping signal. In spin pumping, the current density is much lower (a few μAs, channel width ~ 620 μm). That's why it is reasonable to assume that the effects of thermal voltage in the measured DC voltage should be pretty negligible.

This leaves us with ISHE as the major source for spin pumping. We now attempt to explain the possible physics/mechanisms behind the ISHE. The increase in SCE with decreasing thickness is expected (see section 1-1.3). Spin pumping is inherently an interfacial effect that dominates at lower thicknesses. However, the ideal drift-diffusion model doesn't give a good fit for our case. This means that there might be other factors that might be affecting the thickness dependence of SCE. Since our material is amorphous, devoid of any exciting band structure or density of states, the possible mechanisms for ISHE must be from extrinsic effects. The presence of disorder in the film could be a vital scattering source, which would explain the existence of ISHE in the film. The lower thickness shows a higher SCE, which corresponds to a more disordered film, as evident from

the TEM characterization of the films. Furthermore, the TEM suggests that the interface for 16nm film is rougher than 8nm film. Rough interfaces can cause higher spin loss at the interface and thereby decrease the spin injection efficiency. This can result in a lower SCE for higher thickness.

CHAPTER 1-6: CONCLUSION

In the first part of the thesis, we characterized the material, electrical and spin transport properties of BSG films. Sputtered Bismuth Selenide films were polycrystalline with grains. These grains showed order inside them but are oriented at different angles with respect to each other. SAED showed diffused diffraction rings corresponding to the polycrystallinity of the films. Rutherford backscattering spectroscopy showed the chemical composition of the films, which turned out to be slightly Bi overconcentrated. This Bi overconcentration is an effect of the high volatility of Se. BSG films were grown by co-sputtering of bismuth selenide with gadolinium. TEM and EDX were used for the material and chemical analysis of the films. The TEM images showed an amorphous film for thinner samples (8nm). Thicker samples show occasional crystallites of Bi present in an amorphous matrix. The chemical fingerprint of these crystallites was analyzed via EDX. Following that, we performed basic electrical characterization of the samples: resistivity as a function of temperature. The resistivity of the films increased exponentially with decreasing temperature. This change in resistivity was attributed to 3D variable range hopping inside the film

Finally, we performed spin pumping measurements on these films using a 5nm in-plane CoFeB film. Two different inputs: an AC magnetic field and a DC external field were used to excite the ferromagnetic layer. Both these inputs cause precession of the magnetization at different frequencies. At FMR, the CoFeB layer pumps spin into the BSG layer. This spin is then converted into charge current via ISHE, which results in a DC voltage output across the terminals of the device. The symmetric peaks of the spin pumping signals were analyzed to obtain the ISHE signal, resonance field, and linewidth. The frequency dependence of the resonance field and the linewidth gave us the saturation magnetization and the ferromagnet's damping constant, respectively. They

are combined to obtain the spin mixing conductance and, finally, the spin current injected into the BSG layer. The charge current generated can be calculated using simple Ohm's law. The ratio of the charge-to-spin current density gives us the SCE for different thicknesses. The SCE increases with decreasing thickness, a highly desirable trait for device scaling. The sources of the ISHE were attributed to the extrinsic scattering events, and the thickness dependence of the SCE was analyzed.

CHAPTER 2-1: INTRODUCTION

*Parts of this section of the thesis have been reproduced verbatim from Sahu et al. Appl. Phys. Lett. **117**, 202405 (2020)*

2-1.1 Motivation

In the first part of the thesis, we looked at one of many ways to keep technological progress moving after the end of Moore's law. Spintronic uses the electron's spin to improve the information processing in electronic systems. This is further supported by the fact that spintronics has several advantages for memory applications [74-78]. The major driving force, so far, has been the use of spintronics in Von-Neumann (VN) architectures [79-81]. VN architectures rely on the separation of logic components of a system from its memory components. VN architecture helps in doing several operations efficiently. However, there are specific tasks (such as facial recognition, image recognition, object identification, etc.) where the VN architecture is not very competent. To solve these problems, researchers have come up with a new hardware architecture, called neuromorphic computing where logic and memory components are united [82-84].

Neuromorphic architectures are inspired by the way nervous systems work [83,85,86]. They typically consist of single units, called neurons, that transmit information. These neurons are connected through junctions called synapses [87]. Usually, millions of neurons in a neuromorphic system would be connected via synapses. Neuromorphic devices hold the key to making artificial intelligence (AI). Today, most of these systems are only implemented at a software level, called neural networks [88]. However, a perfect AI requires emulating a nervous system at the software and hardware levels [87,89]. The ionic effect is desirable for neuromorphic hardware devices

because of its similarity to an actual nerve cell [90-92]. Such devices rely on ionic movement to change electrical properties (resistivity, carrier concentration, mobility, etc.) of the underlying material.

We can divide the neuromorphic devices into two simple categories 1) reversible 2) irreversible. As the name suggests, reversible devices have a reversible ionic movement, and their electrical properties can be altered bidirectionally. Irreversible devices can change their electrical properties unidirectionally. Such irreversibility has applications for one-time-programmable (OTP) systems (such as read-only memory, applications specific integrated circuits, OTP-field programmable gate arrays, etc.), an area that has largely been neglected by the spintronic research community [98-100]. We attempt to expand this sphere of knowledge by creating an irreversible magneto-ionic device for OTP applications. Figure 2-1.1.1 shows the typical schematic of an irreversible CMOS device for OTP applications.

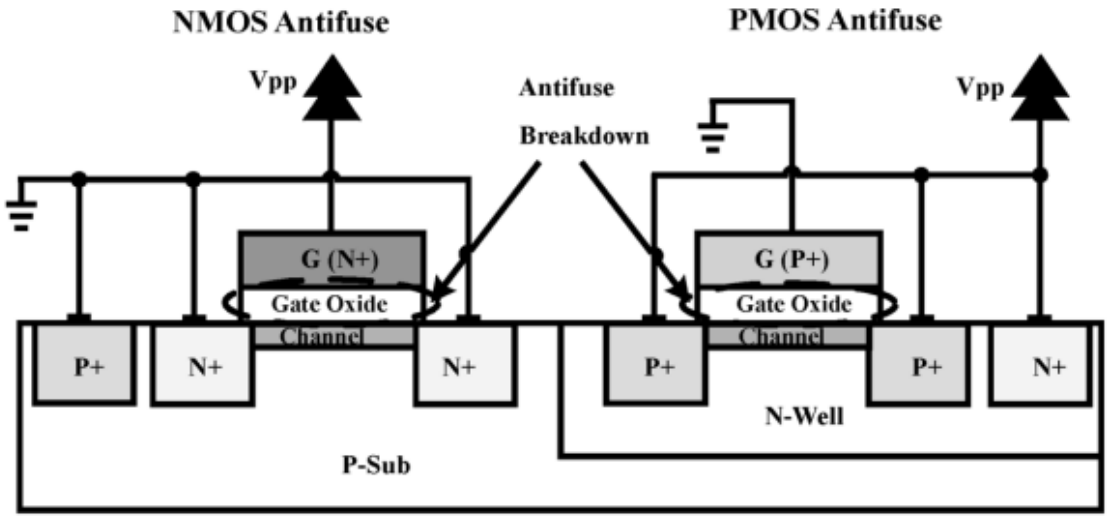

Figure 2-1.1.1: Cross-sectional view of nMOS and pMOS anti-fuse OTP devices in standard CMOS process. Printed with permission [99].

The inclusion of ionic movement into spintronic and magnetic devices remains a challenge. Recently, some work from Beach's group (MIT), W. Wang's (University of AZ), and K. Liu's (Georgetown University) group showed promise in creating a working magneto-ionic device [93-97, 104, 141-143]. In the second part of the thesis, we design a new kind of magneto-ionic device. This magneto-ionic device is characterized by three basic properties: 1) It can do memory operations through magnetization reversal 2) The change in the magnetic property is driven by ionic movement 3) The changes to the magnetic properties are irreversible. The irreversibility of the magneto-ionic device is possible due to the choice of our ionic dielectric (section 2-1.2.4). However, there are several hurdles in making a working device. Firstly, we need a magnetic layer sensitive to the chemical reactions at the surface/interface. This can be overcome by using a magnetic layer with interfacial anisotropy [93,95,101,102]. In interfacial magnetic anisotropy, the magnetic properties are susceptible to the interfacial atomic concentration and can be manipulated easily through ionic movement. Secondly, operating a magneto-ionic device usually relies on chemical reactions to change the coercivity of the magnetic layer. The magnetization of the magnetic layer isn't affected too much. We use an exchange bias structure to solve this problem. The FM of interest (with interfacial anisotropy) is antiferromagnetically coupled to another ferromagnet.

The initial effort of this project was to observe voltage-controlled exchange coupling (VCEC), as mentioned in Zhang et al. [140], through a gated device. This mechanism uses gate voltage to manipulate the exchange coupling constant between two ferromagnets in a synthetic antiferromagnet (SAF) structure. This was one of the original objectives of this project. However, the irreversible magneto-ionic effect was accidentally discovered during the experiment due to our sputtered SiO_x gate. Therefore, instead of studying the VCEC effect, we observed and studied a

change in the exchange bias field, which resulted from the magneto-ionic effect from the gate dielectric.

2-1.2 Magneto-ionic devices

Figure 2-1.2.1 shows the picture of a magneto-ionic system. It typically consists of a FM layer (interfacial anisotropy) with an ionic gate on top of it. This ionic gate contains mobile ions, which can be moved by using the appropriate gate voltage. The polarity of the gate voltage would dictate the direction of movement of the ionic species.

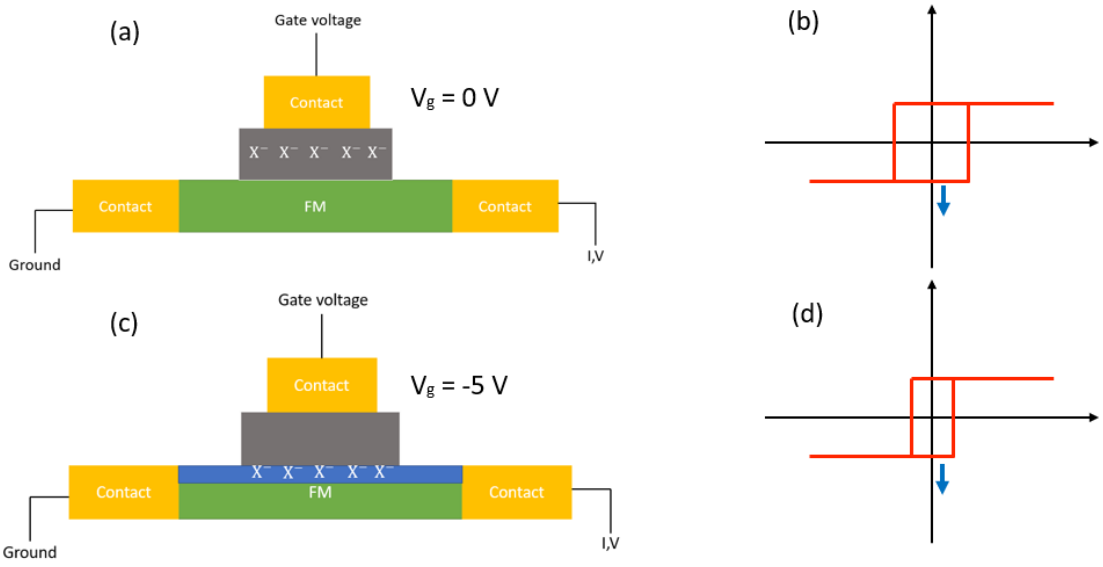

Figure 2-1.2.1: Magneto-ionic device schematic. (a) and (c) show the effects of gate voltage on the mobile ions. (b) and (d) show the respective M-H curves for the device under different gate voltages. The blue arrow corresponds to the direction of the ferromagnet at the respective gate voltage.

I have assumed that the mobile ions are negatively charged (like oxygen ions in our experiment). And the magnetic anisotropy to be perpendicular magnetic anisotropy (PMA). The

application of a negative gate voltage will push the negative ions towards the magnetic layer. The negative ions can then chemically react with the FM layer, changing its magnetic properties (coercivity, dead layer thickness, etc.). Upon applying a positive gate voltage, the ions may be pulled back, and the magnetic anisotropy can be restored. However, this reversibility of the magneto-ionic devices is heavily dependent on the chemical bonds formed during the reaction process. If it forms strong bonds during the reaction process, the chemical reaction will end up being irreversible. This is what we observe in our experiment.

The blue arrows in figure 2-1.2.1 show how the magnetic properties change in an irreversible chemical reaction. The application of negative gate voltage changes the coercivity and the effective thickness of the FM layer, but it doesn't affect the magnetization direction very much. If we design a FM layer with the initial magnetization pointing downwards, it will continue to point downwards after applying a negative gate voltage. Ideally, we would like to observe a field-free magnetization switching of the FM layer at negative gate voltage. To achieve this, we add an exchange bias in the form of a weak synthetic antiferromagnet (SAF). This is done by adding a non-magnetic metal layer (spacer) followed by another ferromagnet (FM2). The second ferromagnet (FM2) will create an exchange bias over the first ferromagnet (FM1). Under the effects of this exchange bias, the hysteresis curve will be shifted (exchange bias field: H_{eb}) by an amount inversely proportional to the thickness of the FM1 layer. A negative gate voltage will force the FM1 into a monostable state (Figure 2-1.2.2). This would allow us to obtain a field-free magnetization switching of the FM1 layer for irreversible devices.

Furthermore, the electrochemical reaction will also result in a change of thickness of FM1, thereby increasing the exchange bias field. Figure 2-1.2.2 (blue arrows) shows the complete field-free reversal of magnetization of the FM1 layer. Additionally, exchange bias field can provide us

with important information regarding the interfacial chemical reaction, such as the change in effective thickness of FM1, the penetration depth of mobile ions, etc.

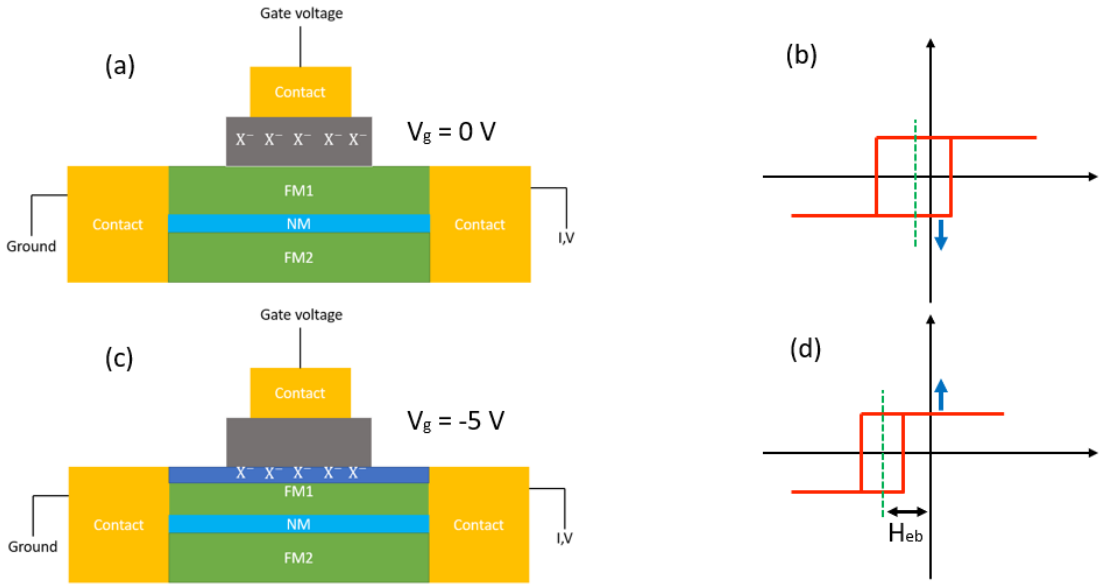

Figure 2-1.2.2: Magneto-ionic device schematic under the effects of exchange bias. (a) and (c) show the movement of ions during the application of gate voltage (b) and (d) show the respective M-H curve. The green dotted line is the center of the M-H curve. The shift in the center is due to the exchange bias field (d). The blue arrows represent the direction of the magnetization.

2-1.2.1 CoFeB/MgO Interfacial PMA

CoFeB/MgO-based interfacial perpendicular anisotropy is used as FM1 [103,104]. The magnetic anisotropy of CoFeB is complicated and intriguing. Mathematically, K_{eff} is the difference in the area under the M-H curve for the easy axis and the hard axis alignment.

$$K_{eff} = \frac{1}{2}\mu_0 M_S H_k. \qquad (2\text{-}1.2.1)$$

Here M_S is the saturation magnetization and H_k is the anisotropy field of the FM layer. The magnetic anisotropy changes with the thickness of CoFeB. Typically, the magnetic anisotropy changes its sign around 1.5nm thickness of CoFeB. This change in sign signifies that the easy axis has moved from in-plane (> 1.5nm) to the out-of-plane direction (< 1.5nm). This is due to the decreased dominance of bulk anisotropy of the CoFeB compared to interfacial anisotropy in ultra-thin regimes [105]. The effective magnetic anisotropy is given by

$$K_{eff} = K_b + \frac{K_i}{t}, \qquad (2\text{-}1.2.2)$$

where K_i is the interfacial anisotropy constant, K_b is the bulk anisotropy constant and t is the thickness of the FM. Equation 2-1.2.2 shows the contributions of bulk and interfacial anisotropies to the effective anisotropy of the CoFeB layer (Figure 2-1.2.3). The actual physics behind the interfacial anisotropy can be pretty complicated, and several first-principle DFT calculations have attempted to show this [106-109]. The critical ingredient is the overlapping of atomic orbitals between transition metals (Co and Fe) and oxygen (from the MgO layer). The overlapping of orbitals changes the electron population in the bands, thereby affecting the magnetic anisotropy of the film. This makes interfacial PMA incredibly sensitive to the oxygen population. However, as we go t < 0.8nm, the FM layer goes into a thermally unstable state (Figure 2-1.2.3), creating superparamagnetic domains. This is seen as a decrease in the magnetic anisotropy constant.

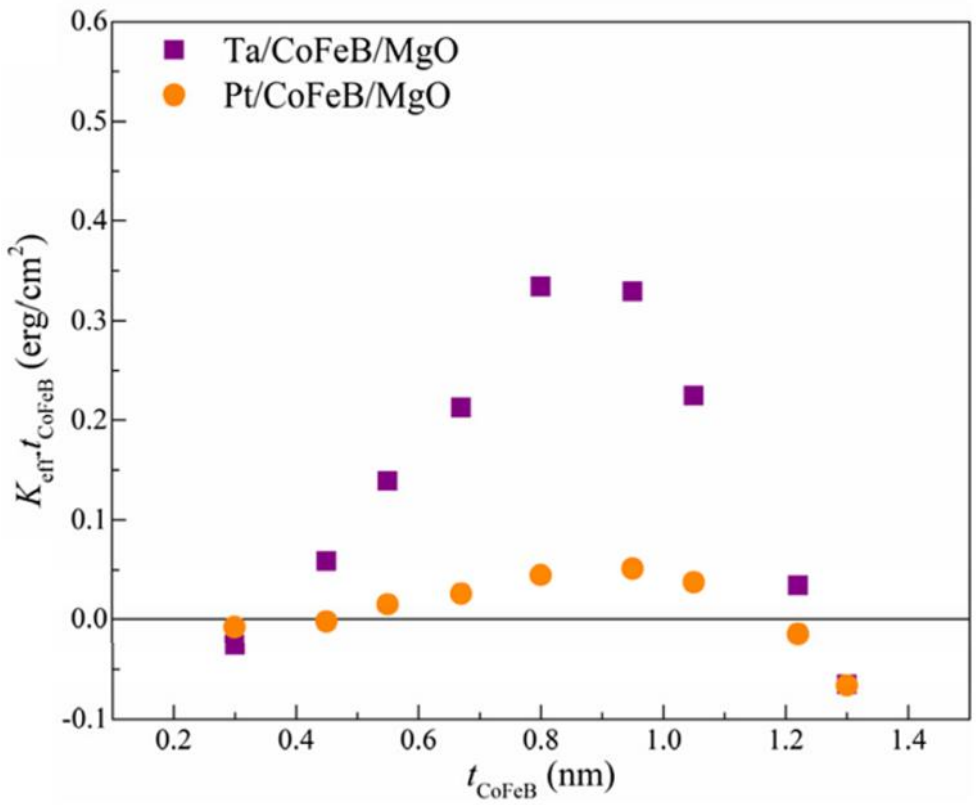

Figure 2-1.2.3: Change in magnetic anisotropy energy per unit area with thicknesses of CoFeB layer with two different underlayers (Ta and Pt) and 2nm MgO as the capping layer. Printed with permission [134].

Interfacial PMA provides a great avenue to design a magneto-ionic device using CoFeB/MgO as the magnetic layer and oxygen ions as the mobile ions. This would ensure that the gate voltage and the mobile ions have significant control over the magnetic anisotropy of the FM layer. Typically, the negative gate voltage (negative oxygen ions) will result in an overoxidized CoFeB/MgO interface. This will lower the magnetic anisotropy and thickness of the CoFeB, reducing the PMA properties.

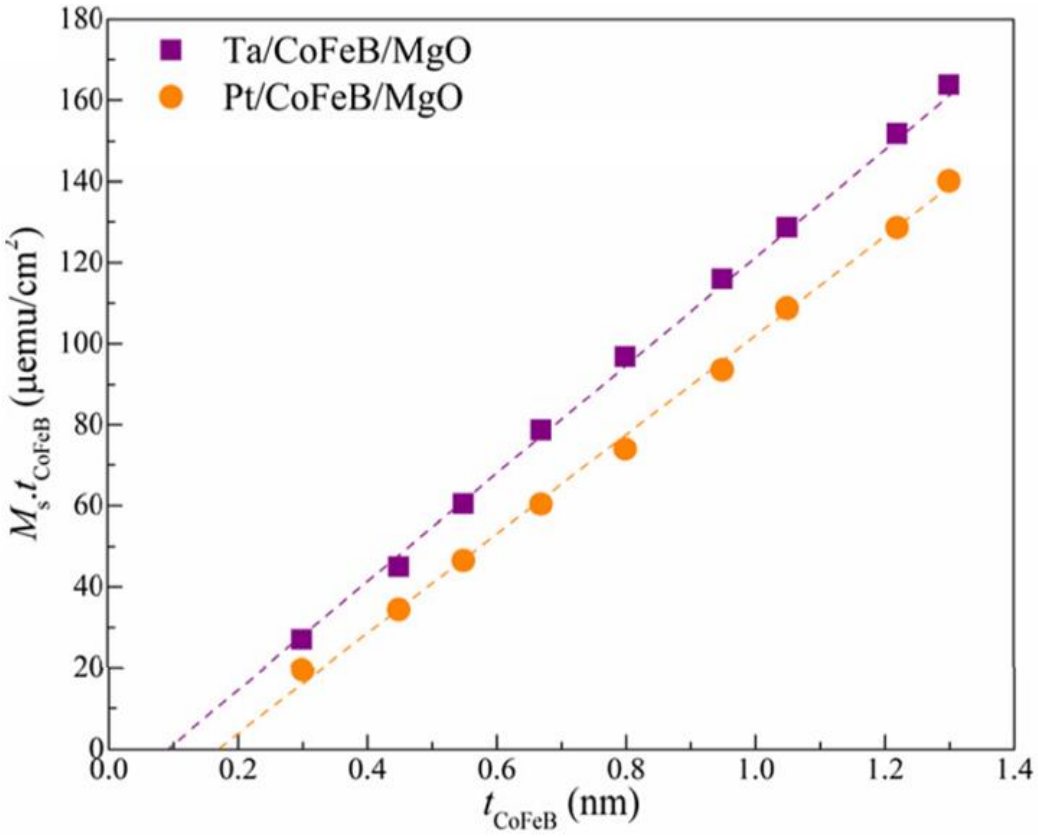

Figure 2-1.2.4: Change is magnetic moment per unit area with respect to thicknesses of CoFeB with Ta and Pt underlayers and 2nm MgO as the capping layer. Printed with permission [134].

Figure 2-1.2.4 shows how the moment per unit area is affected by the thickness of the CoFeB layer. The magnetization of the thin film falls to zero for a non-zero thickness of the CoFeB, called the dead layer. This happens because some part of the CoFeB layer is oxidized due to the adjacent MgO layer. The dead layer doesn't contribute to the magnetic anisotropy of CoFeB. As the negative oxygen ions are accelerated towards the CoFeB/MgO interface, they undergo electrochemical reactions with the CoFeB and over oxidize the interface. Changes in dead layer thickness and the overoxidation of the interface contribute to the changes in magnetic anisotropy.

It is essential to point out that the magnetic anisotropy for multi-domain structures can be different and vary depending on the size, shape, etc of the device [137, 138]. Multi-domain structures can give rise to additional factors that can affect the coercivity such as demagnetization field, domain wall pinning, etc. Demagnetization field can affect the effective magnetic field inside the FM layer. This is represented by a demagnetizing factor that depends on the FM layer's geometry, aspect ratio and shape. Domain wall pinning occurs when a domain wall is stuck at a local energy minimum and doesn't switch easily. This can happen when the FM layer has defects due to the fabrication steps such as bad lift-off, over-etching of the film, etc. These factors can affect the coercivity and exchange bias field of the FM layers.

2- 1.2.2 $[Co(0.3nm)/Pd(0.7nm)]_3$ PMA

The next task is to design the FM2 layer, which will apply an exchange bias field on FM1. The critical requirement for this layer is to have an anisotropy much larger than the FM1 (CoFeB) layer. The material system we chose for our experiment is $[Co(0.3nm)/Pd(0.7nm)]_3$ superlattice structure [118-120]. This magnetic structure has a much higher coercivity (two orders of magnitude larger) than the CoFeB PMA layer. The magnetic anisotropy is similar to equation 2-1.2.2. The interfacial anisotropy is a consequence of the interface between Co and Pd layers. This interfacial contribution favors PMA (just like CoFeB/MgO) and becomes a dominant effect for ultra-thin films.

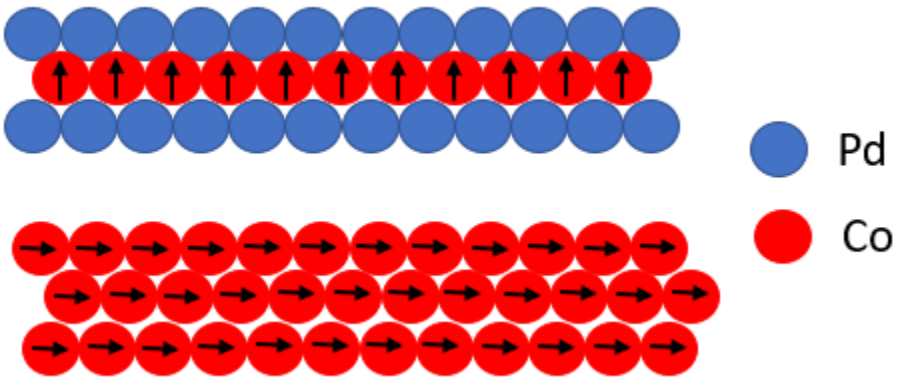

Figure 1-1.2.5: The effects of interfacial anisotropy in $[Co(0.3nm)/Pd(0.7nm)]_3$ multilayer. Multilayers have a dominant interfacial anisotropy that gives rise to PMA, whereas bulk films have an in-plane anisotropy.

The volumetric bulk anisotropy is complex and can contain several contributions. The bulk magnetic anisotropy in superlattice systems can be divided into at least two components: 1) Shape anisotropy 2) Magnetocrystalline anisotropy [108,121,122]. Shape anisotropy is a consequence of long-range dipole interactions. This tends to align the magnetization along the long axis of the device/thin film. For the case of a thin film, the shape anisotropy is along the in-plane direction. This becomes a dominant term for higher thickness and plays a significant role in in-plane magnetic anisotropy. Magnetocrystalline anisotropy arises due to the preferential direction of the magnetization vector along a specific crystallographic orientation. The first-order contribution is due to the coupling between the orbital motion of the electrons with the crystal electric field [123]. The second-order effect is the interaction between magnetic dipoles. For $[Co(0.3nm)/Pd(0.7nm)]_3$ superlattice, the direction of magnetocrystalline anisotropy is (111). The magnetocrystalline anisotropy is also affected by the lattice strain on the magnetic layer. This is sometimes described by a different contribution called magneto-elastic anisotropy. The effects of lattice strain are

typically dominant at the interface. However, the strain can spread to several atomic layers of the ultra-thin film and is often considered a term for the bulk anisotropy.

2-1.2.3 Exchange bias

We use a gate voltage-dependent exchange bias field on the CoFeB layer to enable field-free magnetization reversal [110-113]. An exchange bias is created by placing $[Co(0.3nm)/Pd(0.7nm)]_3$ layer next to the CoFeB layer separated by a non-magnetic Ta layer [114].

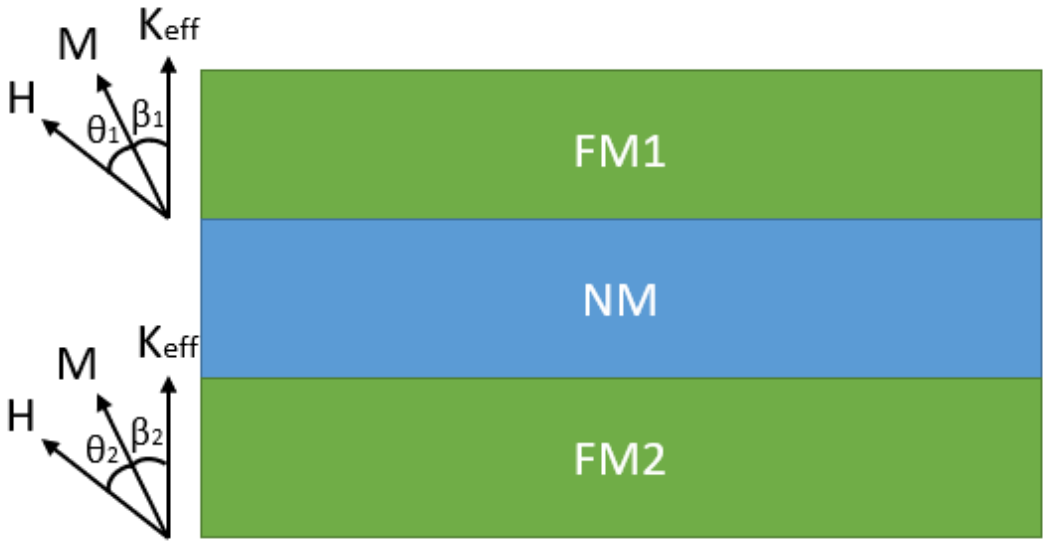

Figure2-1.2.6: Schematic of a typical exchange bias system. The magnetic anisotropies (K_{eff}) are in the out-of-plane direction. The angles θ and β are defined as the angle between magnetization (M) -field (H) and magnetization (M) -anisotropy (K), respectively.

Figure 2-1.2.6 shows the typical structure for creating an exchange bias system. The FM2 can be an antiferromagnetic or a ferromagnetic film. The FM2 will generate an exchange bias field on FM1, which will result in a shift of the magnetic hysteresis loop of the CoFeB layer. This shift in the magnetic hysteresis is called the exchange bias field. To derive the exchange bias field, we

need to use Stoner-Wolfharth (SW) model for the structure [115]. It must be noted that the SW model is designed for single domain structures. Here we make four critical simplifying assumptions:

1) The magnetic anisotropy directions are all out-of-plane;

2) The magnetic field is only applied in the out-of-plane direction;

3) The anisotropy constant of the FM2 is much higher than the anisotropy constant of FM1;

4) The magnetic field applied is much less than the coercivity of FM2.

These assumptions line up well with our experiment (minor loop measurement). The first two assumptions allow us to simplify the SW energy equation, whereas the third and fourth assumptions signify that the energy of the FM2 layer is effectively constant. The SW model allows us to write the total energy per unit area as

$$E_A = [-\mu_0 H M_{F1} t_{F1} Cos(\theta - \beta_1) + K_{F1} t_{F1} Sin^2(\beta_1)] + [-\mu_0 H M_{F2} t_{F2} Cos(\theta - \beta_2) + K_{F2} t_{F2} Sin^2(\beta_2)] + J_{eb} Cos(\beta_1 - \beta_2), \quad (2\text{-}1.2.3)$$

where H is the magnetic field, $M_{F1/F2}$ is the saturation magnetization of FM1/FM2, $t_{F1/F2}$ is the thickness of FM1/FM2, $K_{F1/F2}$ is anisotropy constant of FM1/FM2, and J_{eb} is the exchange coupling constant. The respective angles are shown in Figure 2-1.2.6. Here the term in the first bracket is the energy of the FM1, and the one in the second bracket is the energy of FM2. The energy of each FM layer consists of Zeeman energy, which depends directly on the applied external magnetic field. The anisotropy energy depends on the anisotropy constant. The last term is the exchange interaction energy. Under the assumptions that the FM2 has a much larger anisotropy

constant and the magnetic field applied is much smaller than the coercivity of the FM2 layer, we can assume $\beta_2 \sim 0$. This means the FM2 layer stays fixed and doesn't move under the application of small magnetic fields. Furthermore, we also assume that the magnetic field is only applied in the out-of-plane direction ($\theta \sim 0$). Equation 2-1.2.3, then simplifies into

$$E_A = [-\mu_0 H M_{F1} t_{F1} Cos(-\beta_1) + K_{F1} t_{F1} Sin^2(\beta_1)] + [-\mu_0 H M_{F2} t_{F2}] + J_{eb} Cos(\beta_1). \quad (2\text{-}1.2.4)$$

To find the energy minima for β_1, we take the derivative i.e $\frac{\partial E_A}{\partial \beta_1} = 0$. This yields us the non-trivial conditions for which the energy is minimized to be

$$[\mu_0 H M_{F1} t_{F1} + 2K_{F1} t_{F1} Cos(\beta_1)] - J_{eb} = 0. \quad (2\text{-}1.2.5)$$

Now, we apply the conditions for the coercive field of FM1 i.e $\beta_1 = 0,\pi$ and $H = H_{c1}, H_{c2}$. This gives us the coercive switching fields as

$$H_{c1} = \frac{J_{eb} - 2K_{F1} t_{F1}}{\mu_0 M_{F1} t_{F1}}, \quad (2\text{-}1.2.7)$$

$$H_{c2} = \frac{J_{eb} + 2K_{F1} t_{F1}}{\mu_0 M_{F1} t_{F1}}. \quad (2\text{-}1.2.7)$$

From here, one can write the exchange bias field as simply: $H_{eb} = \frac{H_{c1} + H_{c2}}{2}$. This gives us the final expression for the exchange bias field

$$H_{eb} = \frac{J_{eb}}{\mu_0 M_{F1} t_{F1}}. \quad (2\text{-}1.2.8)$$

This equation is similar to the Meiklejohn-Bean model used for exchange bias between the FM layer and AFM layers [115]. Typically, most fabricated devices are expected to be multi-domain structures. There could be additional coupling between the domains in multi-domain

devices, which would require micromagnetic simulations to analyze. One of the key properties of using an exchange bias is that the exchange bias field depends on the thickness of the FM1 layer. Ionic movement decreases the effective thickness of the FM1 layer. This change in thickness of the FM1 layer can impact the exchange bias field, causing it to increase in magnitude.

The exchange coupling constant (J_{eb}) plays a crucial role in determining the exchange interaction between the two ferromagnets. The exchange coupling can be a consequence of several different contributions. However, there are two major mechanisms can that are known to create exchange bias: 1) RKKY interaction 2) Dipole-Dipole Interaction. RKKY theory considers the interaction between nuclear spins of the fixed atoms via the conduction electrons through hyperfine interaction [116]. The exchange interaction is given by

$$H(R_{ij}) = \frac{I_i . I_j}{4} \frac{|\Delta_{k_m k_m}|^2 m^*}{(2\pi)^3 R_{ij}^4 \hbar^2} \left[2k_m R_{ij} Cos(2k_m R_{ij}) - Sin(2k_m R_{ij})\right], \quad (2\text{-}1.2.9)$$

where R_{ij} is the distance between nuclei i and j, I_i is the nuclear spin of atom i, $\Delta_{k_m k_m}$ is the matrix element representing the strength of hyperfine interaction, m^* is the effective mass of the electron, and k_m is the Fermi momentum

P. Bruno et al uses a comprehensive quantum mechanical model to write down the coupling constant between ferromagnets under exchange coupling [117]. Figure 2-1.2.7 shows the results of calculations as to how the interlayer exchange interaction varies as a function of the thickness of the spacer layer.

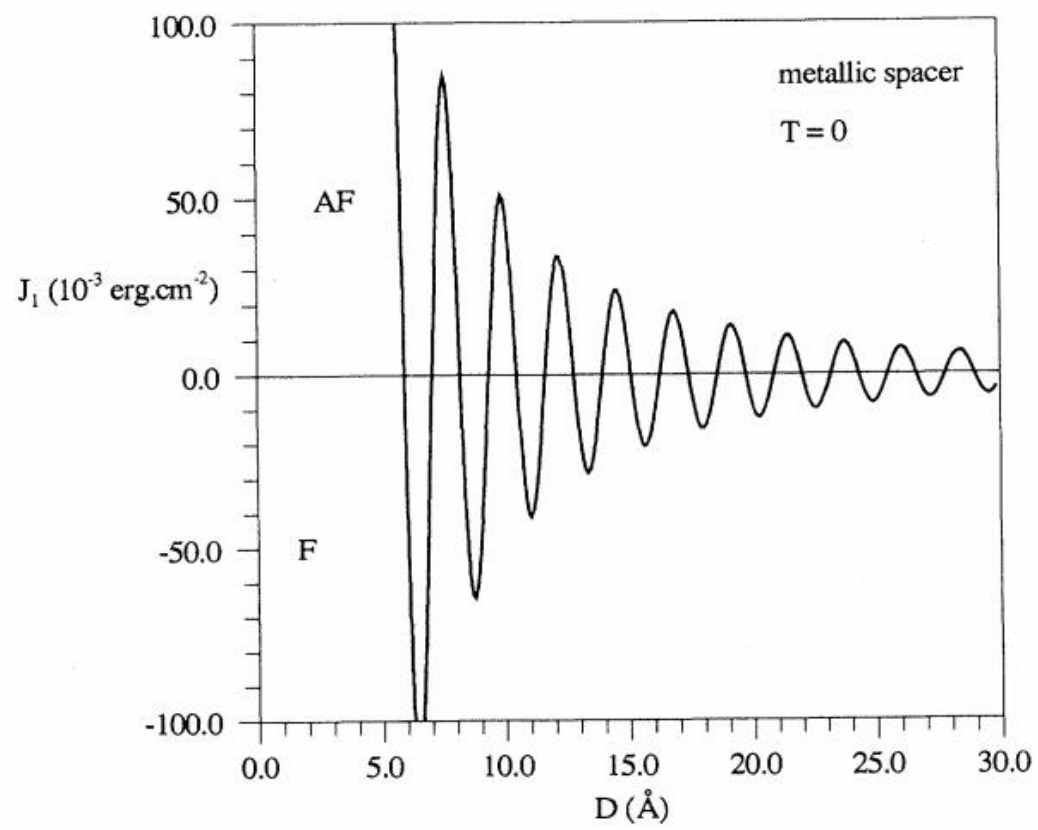

Figure 2-1.2.7: Interlayer exchange coupling, at T = 0, for the free-electron model, in the case of a metallic spacer. Please refer to Bruno et al. Printed with permission [117].

As one can see, the coupling constant shows damped oscillation with respect to the spacer layer thickness. A positive value of the coupling constant corresponds to the antiferromagnetic coupling, whereas a negative value corresponds to ferromagnetic coupling. The properties of the spacer layer play a significant role in deciding the exchange bias between the FM layers. We used a spacer layer of 1nm Ta to separate CoFeB (FM1) from the $[Co(0.3nm)/Pd(0.7nm)]_3$ layer, which shows a weak antiferromagnetic coupling.

2-1.2.4 Ionic gate

The ionic gate is a very crucial component of the magneto-ionic device. This layer contains the mobile ions that are manipulated using a gate voltage [128]. There are several kinds of materials used for the ionic gate. Magnetic layers, being metals, don't usually respond well to a pure electric field. Magneto-ionic effects are the simplest in terms of operation. The disadvantage of using ionic movement is the speed of operation since ionic movements are not the fastest physical mechanisms. Geoff Beach's group at MIT has been a pioneer of magneto-ionic devices using, GdO_x as the gate dielectric [93-97]. This is promising since GdO_x is an effective supplier of mobile and can also sustain PMA in materials like Co. Furthermore, GdO_x has a high dielectric constant which allows one to achieve high operating gate voltage. This results in reversible magneto-ionic effects. Another possible alternative is to use ion gels [139]. Unfortunately, ion gels are challenging to integrate with microelectronic fabrication technology, limiting their applicability in actual devices.

For our experiment, we use a much more well-known dielectric: SiO_x. SiO_x is used quite extensively in microelectronics fabrication. This makes SiO_x much more accessible to implement in actual devices for applications. The quality of dielectrics is heavily dependent on the thin film deposition technique. Typically, atomic layer deposition (ALD) will give a very high-quality film with a low concentration of mobile ions. Chemical vapor deposition (CVD) will give an intermediate quality with some mobile ions but not enough to create a significant change in the interfacial PMA of the CoFeB. Sputtering will provide us with the highest concentration of mobile ions and makes a good candidate for an ionic gate. Typically, the mobile ions in these systems are the oxygen ions and can be moved back and forth by a gate voltage. Sputtered SiO_x can have very reactive ionic species, creating the irreversibility necessary to make OTP devices.

The ionic migration through the gate dielectric can be written using a drift-diffusion model, to analyze the migration of oxygen ions and vacancies through the dielectric. The ion-vacancy generation-combination is given by the exponential dependency [129]:

$$P_g = f_0 exp\left[-\left(E_g - \gamma eE\right)/(k_B T)\right], \quad (2\text{-}1.2.10)$$

$$P_r = C_{ion}\, f_0 exp[-(E_r - \gamma eE)/(k_B T)], \quad (2\text{-}1.2.11)$$

where P_g and P_r are the generation and recombination rate of ion-vacancy pairs, respectively; f_0 is the vibration frequency of ions surrounding the vacancy; C_{ion} is the ion concentration; E_g and E_r are the formation and recombination energy respectively; E is the applied electric field; γ is the contribution of bond polarization to the local electric field. The rate of drift and diffusion in the oxide layer is dependent on the oxygen migration barrier (E_m) and the lattice constant (a) of the SiO_x layer. The drift velocity is given by:

$$V_{ion} = af_0 exp\left(\frac{-E_m}{k_B T}\right) sinh\left(\frac{eaE}{2k_B T}\right). \quad (2\text{-}1.2.12)$$

The parameters for lattice constant and oxygen energy migration barrier is given in table 2-1.2.1 [129]:

Parameter	Parameter name	Parameter value
f_0	Vibration frequency	10^{13} /s
E_m	Oxygen migration barrier	0.1 - 0.5 eV
a	lattice parameter	2 - 8 Å

Table: 2-1.2.1. Parameters used for the analysis of mobile ions in SiO_x dielectric.

Our sputtered gate oxide would be a low crystallinity SiO_x layer, which leads to a range of lattice constants and the oxygen migration energy barrier, compared to the results obtained from the single crystalline structures. Figure 2-1.2.8 shows the ionic velocity for different lattice constants and oxygen energy migration barriers at different E-fields. As expected, increasing the lattice constant, and decreasing the oxygen energy migration barrier increases the ionic velocity.

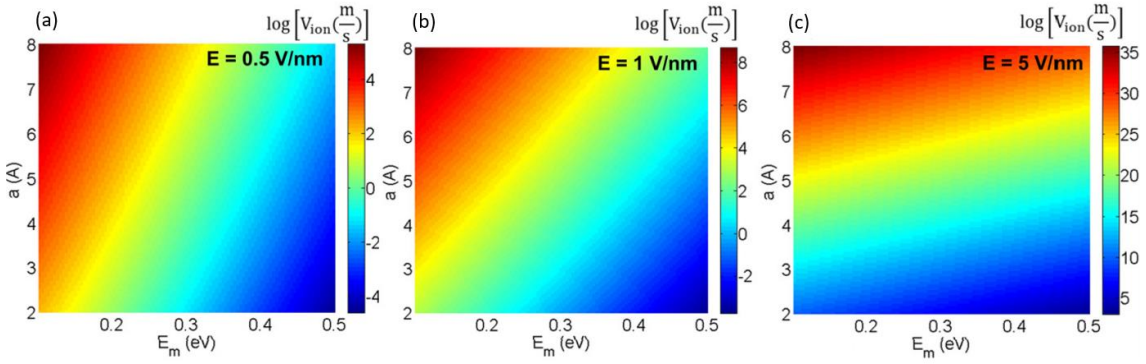

Figure 2-1.2.8: Ionic velocity in the gate dielectric for a range of different lattice constants and Oxygen energy migration barriers (equation 2-1.2.12). This analysis is repeated with three different E-fields.

At low E-fields, the ionic velocity is sensitive to the migration energy barrier. A small change in the migration energy barrier will cause a significant change in ionic velocity. However, at higher E-fields, the situation is reversed. The lattice constant plays a considerable role (at higher E-fields), which affects the ionic velocity. In our experiment, the maximum E-field we reach is ~ 0.05 V/nm. Hence it is fair to say that, in our experiment, we are very much in the lower E-field regime, where the oxygen migration barrier dominates.

CHAPTER 2-2: STACK DESIGN

The stack is grown on thermally oxidized silicon substrates using DC magnetron sputtering. A key bottleneck in making the stack is to ensure that the films have the correct crystallographic orientation. The crystallographic orientation will ensure a good PMA. This is especially important for the $[Co(0.3nm)/Pd(0.7nm)]_3$ layer, which requires an out-of-plane crystallographic orientation of (111). We need to first understand the fundamental forces that play a role during the growth of textured thin films. Typically, there are two significant contributions: 1) Surface Energy 2) Lattice strain

Surface energy always plays a significant role during any thin-film growth. Thin-film growth is a thermodynamic process and requires low surface energy at a steady-state. The surface energy is a consequence of the extra energy needed to hold the surface atoms compared to the bulk atoms. One of the vital deciding factors behind surface energy is the number of dangling bonds present at the surface. These dangling bonds increase the surface energy and make the film unstable. In most fcc metals, the film's surface energy is a vital function of the out-of-plane crystallographic orientation [130]. For fcc metals, Figure 2-2.1.1 shows the dangling bonds present in each crystallographic orientation.

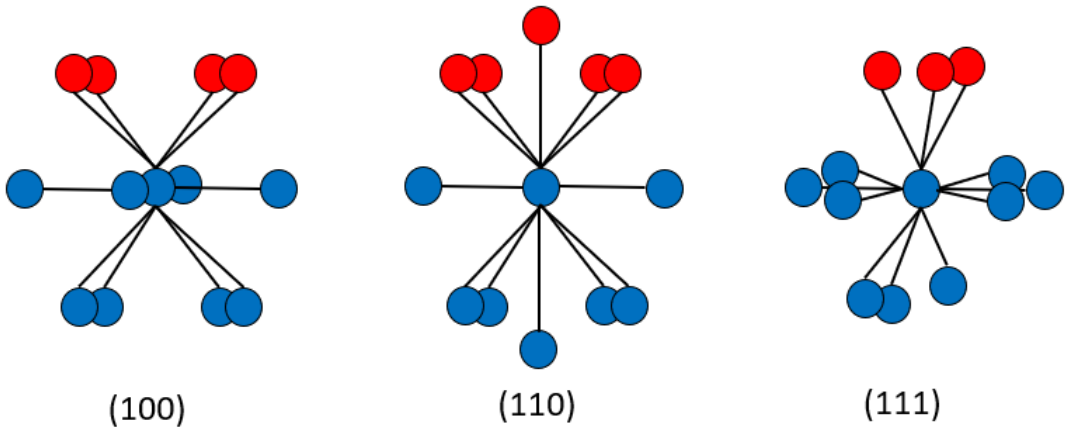

Figure 2-2.1.1: Atomic arrangement for fcc metals for different crystal orientations. The red dots are the surface atoms that result in dangling bonds and increase surface energy.

As one can observe, (100), (110), (111) have four, five, and three dangling bonds respectively at the surface. Hence, (111) has the lowest surface energy, (100) has the second-lowest surface energy, and (110) has the highest surface energy. This trend is also verified by theoretical DFT calculations [130]. Hence, when we grow fcc metals on amorphous substrates, the surface energy becomes the deciding factor for the out-of-plane crystallographic orientation. However, surface energy only plays a critical role in deciding the texture along the out-of-plane direction. It doesn't contribute to the in-plane texture of the film.

The second contribution during the thin film growth is lattice strain. Lattice strain arises when a seed layer (layer below the thin film) acts as an atomic template to develop the original film. This requires a meticulous selection of materials. The key motivation is to use the lattice of the seed layer to grow the film along with the appropriate orientation. This would mean that the lattice constants of the seed layer must be close to the lattice constant of the original film. Figure 2-2.1.2 shows how the lattice matching of two different thin films looks like.

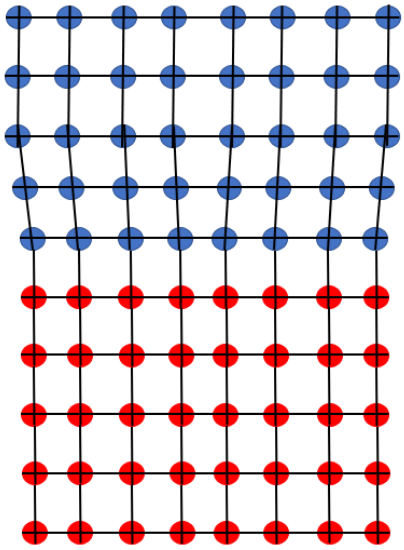

Figure 2-2.1.2: Lattice matching between two different thin films. The red dots are the seed layer atoms, whereas the blue dots are the thin film grown on top of the seed layer.

During heteroepitaxial thin film growth, the lattice constants are not precisely equal. Hence, at the interface, we get some degree of lattice strain. However, as we increase the film thickness, the lattice strain will slowly relax into the original lattice constant. For our experiment, the key material for out-of-plane texture is $[Co(0.3nm)/Pd(0.7nm)]_3$ structure. These films need to have (111) out-of-plane textures to ensure good PMA. A well-known seed layer for $[Co(0.3nm)/Pd(0.7nm)]_3$ multilayer is Pd (111) thin film. Being a fcc metal, Pd can be grown on top of amorphous substrates with (111) out-of-plane texture due to surface energy. Hence, this combination (Pd + $[Co(0.3nm)/Pd(0.7nm)]_3$) works well to ensure that we get a well-textured $[Co(0.3nm)/Pd(0.7nm)]_3$ layer. Unfortunately, Pd can't be directly grown on a thermally oxidized Si substrate due to low adhesion. Hence, we have to use an adhesion layer (5nm Ta) to ensure that Pd sticks to the wafer properly. Hence the complete stack looks like Figure 2-2.1.3.

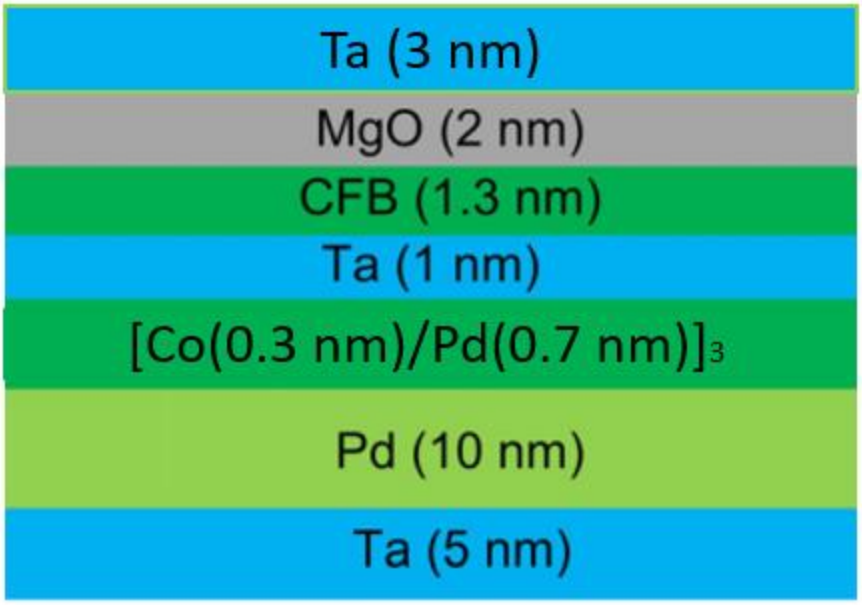

Figure 2-2.1.3: The complete stack used for the magneto-ionic devices.

In the above stack, CoFeB is the FM1, which will be altered due to magneto-ionic effects at the interface between CoFeB and MgO. $[Co(0.3nm)/Pd(0.7nm)]_3$ layer is the FM2 which provides the exchange bias to the CoFeB layer. Ta is the spacer layer that separates the FM1 and FM2 layer. The spacer layer decides the nature of exchange bias between FM1 and FM2 (weak antiferromagnetic). To grow $[Co(0.3nm)/Pd(0.7nm)]_3$ (111), we use Pd (111) as the seed layer. The $[Co(0.3nm)/Pd(0.7nm)]_3$ multilayer consists of 0.3nm of Co and 0.7nm of Pd and this structure is repeated three times to give us around 3nm of $[Co(0.3nm)/Pd(0.7nm)]_3$ structure. And finally, Ta (5nm) is used as an adhesion layer to ensure that the films stick to the substrate correctly. The 3nm of Ta on top is a capping layer to protect the stack from oxidation. This layer is removed during fabrication before the deposition of the ionic gate dielectric.

CHAPTER 2-3: METHODS

2-3.1 Material growth and characterization

The thin-film stack for this experiment was grown by DC magnetron sputtering (except the ionic dielectric, which was grown by RF sputtering). For details on DC magnetron sputtering, please refer to section 1-2.1.1. For material characterization, we used two different techniques to characterize the crystallinity and chemical profile of this film: 1) TEM (+ EDX chemical mapping) 2) X-ray diffraction (XRD). The details of TEM are given in section 1-2.1.2.

2-3.1.1 Rapid thermal annealing

Rapid thermal annealing (RTA) is a primary thermal treatment done to improve film crystallinity and properties. In RTA, the wafer of interest is heated using a furnace to very high temperatures, which can go up to 1000 C in industrial manufacturing. These rapid thermal spikes can be generated by using high-intensity light sources (lamps or lasers). Such high temperatures create a sudden spike in the thermal energy of the atoms of the wafer. RTA is often used to repair defects in films.

2-3.1.2 X-Ray diffraction

X-ray diffraction (XRD) is one of the most common experimental techniques used to characterize thin films' crystallinity and crystallographic orientations. In our stack, the crystallographic orientation, particularly the out-of-plane texture, is essential for ensuring good PMA of the $[Co(0.3nm)/Pd(0.7nm)]_3$ multilayers. In XRD, we expose our film to beams of X-rays. These X-rays undergo reflections from the atomic layers present in the stack. These reflections then combine to create a series of diffraction patterns. Bragg's law governs the interference of the reflected X-

rays. The typical 1D XRD doesn't provide enough information about the texture of the film. To get more information about the texture, we will need to look at how the crystallographic orientation of the film varies along the off axis. This can be achieved by using an XRD with a 2D detector.

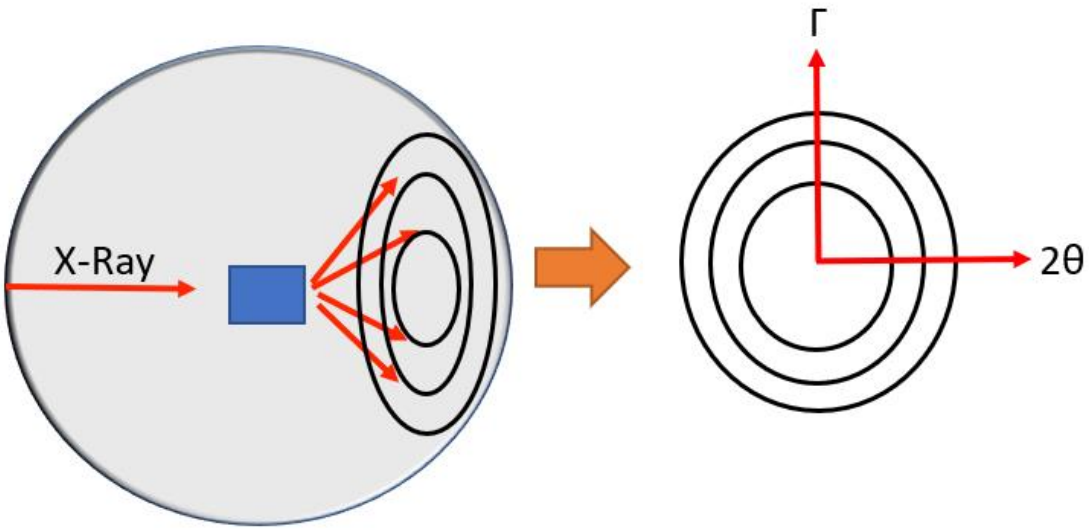

Figure 2-3.1.1: Schematic of a 2D XRD system and the diffraction rings.

Figure 2-3.1.1 shows the schematic of a 2D XRD system which allows us to capture patterns of the diffraction rings. Each diffraction ring corresponds to a specific 2θ value. We also get information about the spread of peaks in off-axis. Here Γ is defined as the angle the rings subtend in the off-axis directions. This gives us crucial information about the spread of the texture in Γ direction. For a powder texture, Γ spread will be high since a specific crystal orientation will be randomly distributed in real space. If a film is textured, the spread in Γ will be small. The scale of the detector (highest value of Γ) depends on the diameter of the detector and the distance of the detector from the sample stage. For Bruker D8, this maximum value of Γ is around 17 deg from the center (Γ = 0 deg) [Ref: Guichuan Yu from Charfac].

2-3.2 Fabrication process flow

The fabrication process flow consists of all the basic steps described in section 1-2.2: Lithography, etching, e-beam evaporation, etc. RTA was performed at 200 C for 30 mins after the deposition of the stacks. The fabrication process flow is divided into three steps.

In step 1, We pattern the stack into Hall bars. This is done by using simple photolithography to define the Hall bar area. This is followed by ion mill dry etching to remove the material.

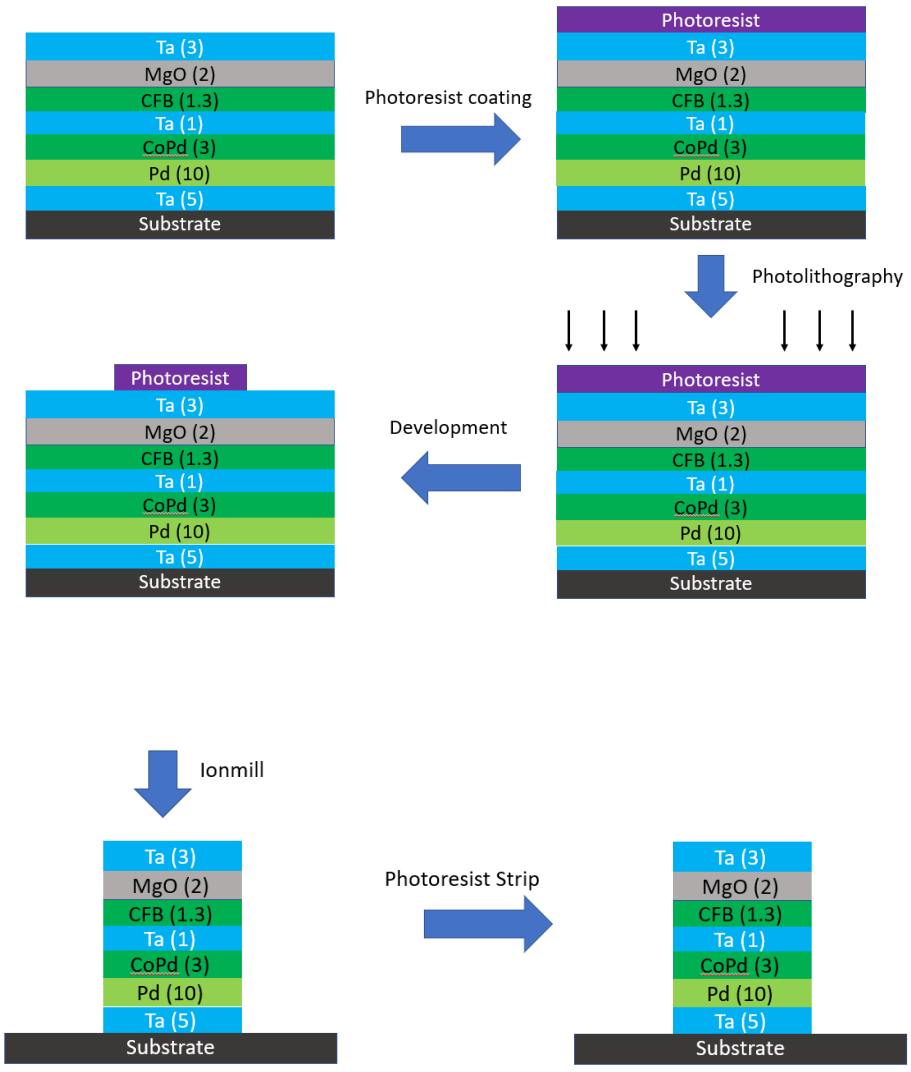

Figure 2-3.2.1: Process flow of the first step of the patterning process.

In the second step, we deposit the ionic gate dielectric. This is done by doing a second step to photolithography to define a specific window for dielectric deposition and then an ionmill step to get rid of Ta capping. We deposit 100nm of SiO_x via RF sputtering followed by a lift-off.

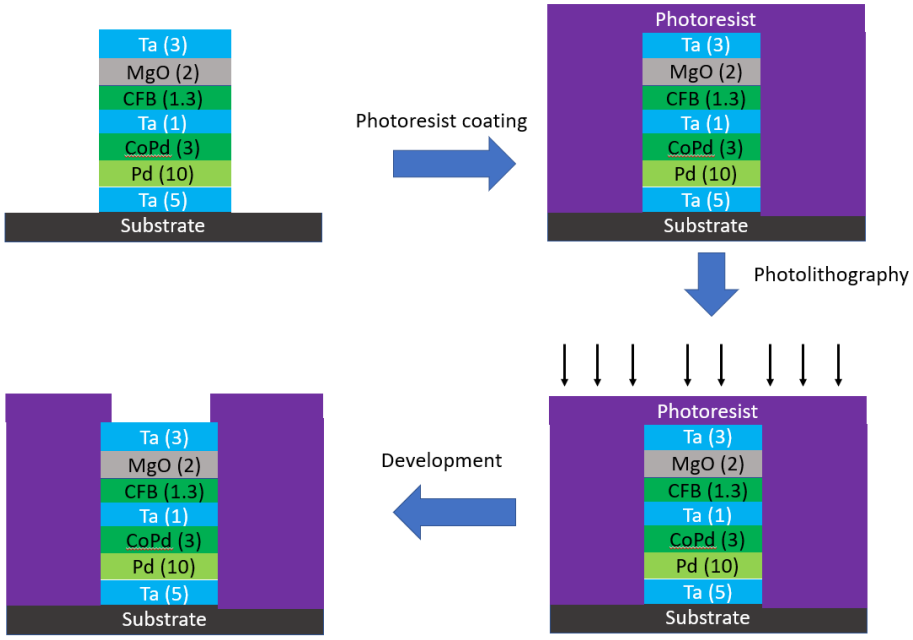

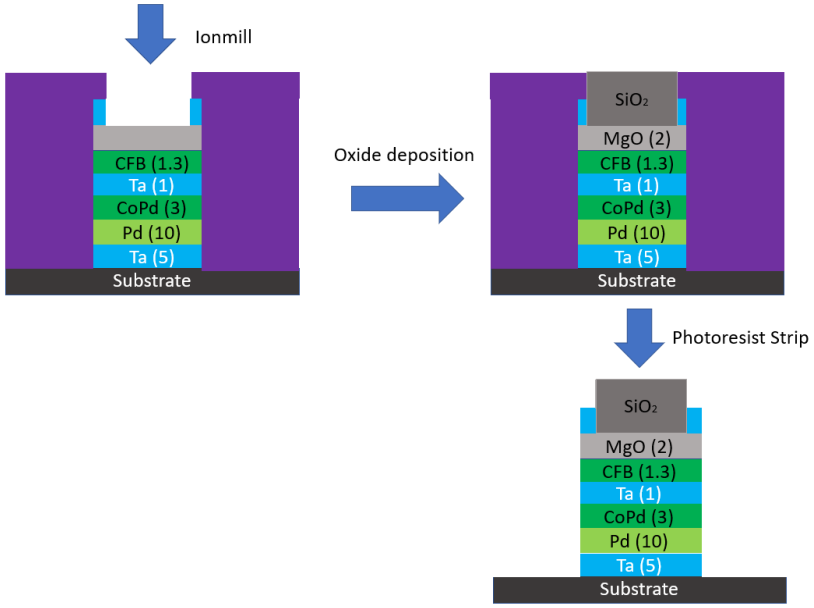

Figure 2-3.2.2: Process flow of the second step of the patterning process.

In the third and final step of the patterning process, we do the third photolithography step to define the contact regions, followed by ion mill to remove capping. Then we deposited 10nm of Ti followed by 100nm of Au for the contact. This was completed with another lift-off.

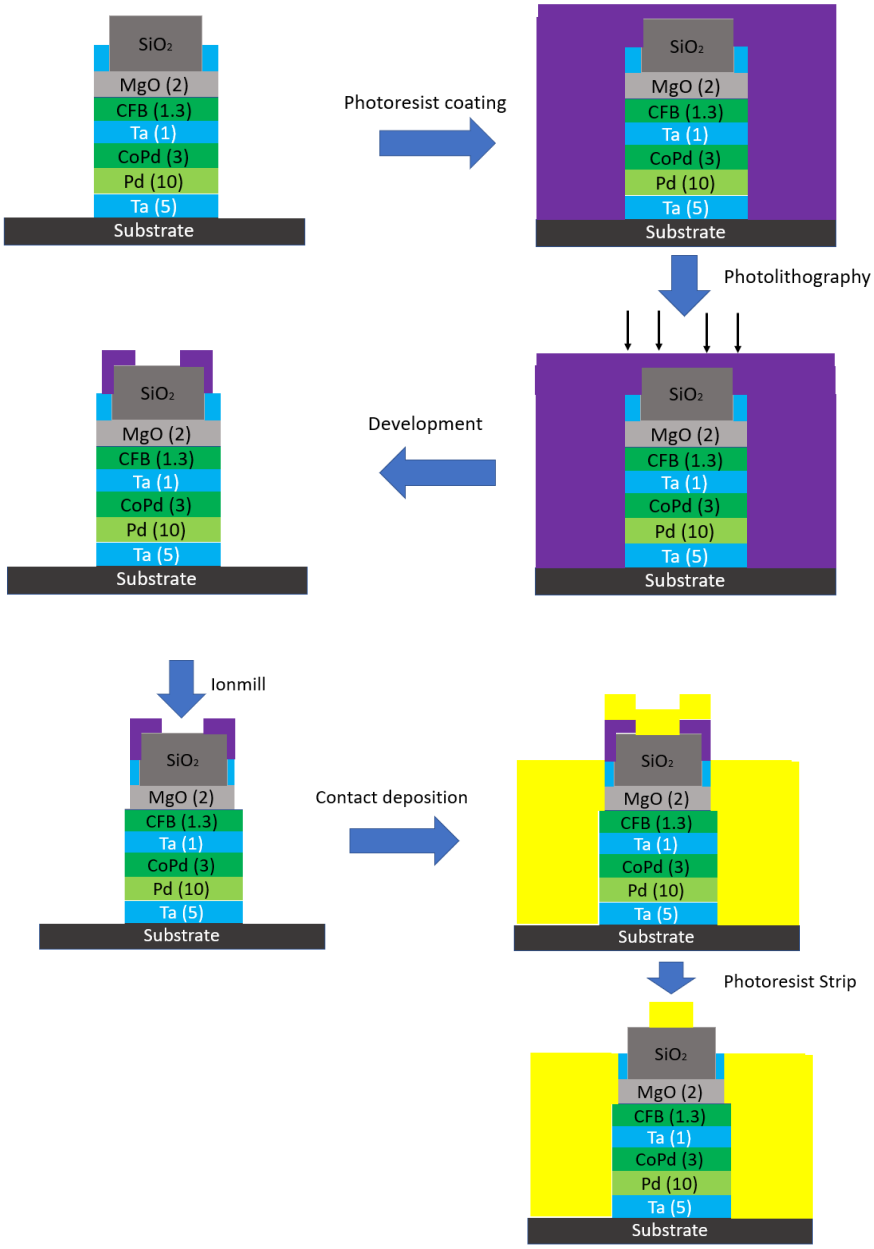

Figure 2-3.2.3: Process flow of the third step of the patterning process.

Figure 2-3.2.4 shows the device dimension of the Hall bar structure. The dimensions of the device is different from the device used in Sahu et al [102]. This changes the magnetic properties of the device to some extent (multi-domain structures have variations based on device size).

However, this device shows better magnetic properties and is capable of doing field-free irreversible switching.

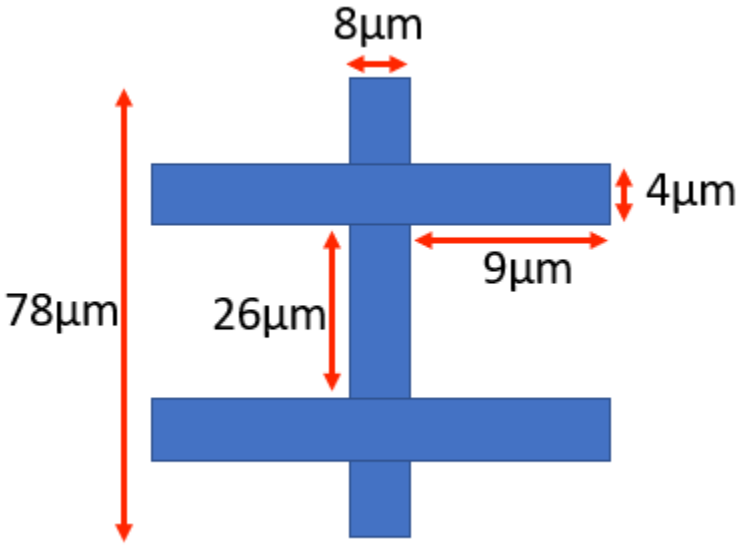

Figure 2-3.2.4: Dimensions of the Hall bar device shown in the thesis.

2-3.3 Magnetic and electrical measurements

Figure 2-3.3.1 shows the testing setup for anomalous Hall effect (AHE) measurement. In this setup, we inject a charge current through the long axis of the Hall bar. The AHE signal is measured through the cross-Hall bar, which is fed into a nanovoltmeter. A typical AHE curve would consist of a hysteresis. However, things can become complicated when you have more than one magnetic layer. To study the magnetic properties of our stack, we perform two different kinds of M-H curves: 1) major loop 2) minor loop. Experimentally, the only difference between the major and the minor loop is the range of magnetic field used for the M-H curve measurement.

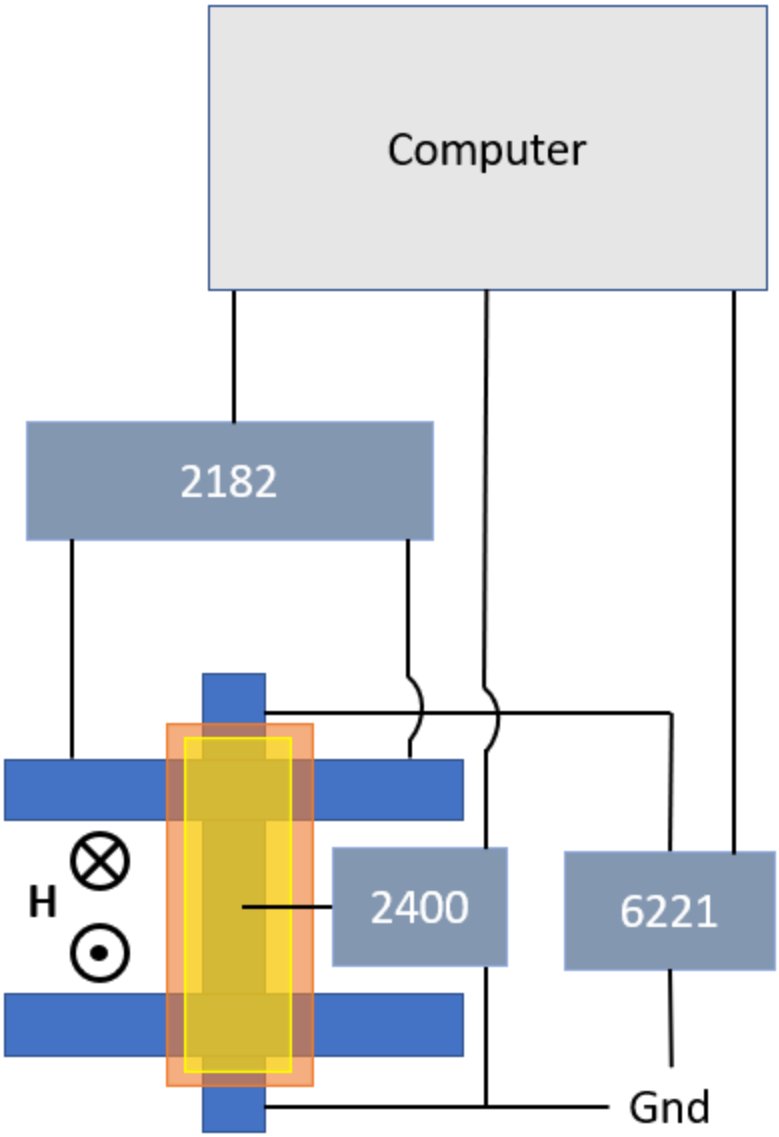

Figure 2-3.3.1: Setup for AHE signal measurement.

The magnetic field is swept over a very large range (6000 Oe). This magnetic field range is large enough to manipulate both the CoFeB (FM1) and $[Co(0.3nm)/Pd(0.7nm)]_3$ (FM2) layers. In the minor loop, the range of magnetic field sweep is very small, typically 300 Oe. In such a situation, we can only see the AHE curve from the CoFeB layer. The minor loop is quite important

and allows us to characterize the exchange bias between CoFeB and $[Co(0.3nm)/Pd(0.7nm)]_3$ layers. The measurement was done using Quantum Design PPMS system. The current supply is given by using 6221 Keithley's current source. The voltage is measured using a 2182 nonovoltmeter, and the gate voltage is supplied using a 2400 voltage source.

CHAPTER 2-4: MATERIAL CHARACTERIZATION

2-4.1 TEM and EDX characterization

We performed TEM and EDX to characterize the material and chemical properties of the stack. Figure 2-4.1.1. shows the EDX image mapping of the stack. We can see all the different film layers present in the stack. The Fe signature (dark green) is a good indication of the presence of the 1.3nm thick CoFeB layer. This Fe signature is combined with a part of the Co signal (orange), which signals the alloying of Co and Fe. The Mg signal (light blue), combined with oxygen signal (light green), shows the 2nm thick MgO layer above the CoFeB layer. The Ta signal (magenta) shows three distinct layers. The first/top one corresponds to the capping layer. One can see that the capping is mixed with oxygen signal, indicating oxidation of the Ta capping layer. The second layer is a very thin distinct layer present between CoFeB and the $[Co(0.3nm)/Pd(0.7nm)]_3$ layer. This ultra-thin layer (1nm) corresponds to the spacer layer between the two ferromagnets. The spacer layer is relatively continuous without any significant breaks in the imaging area. The third layer of 5nm Ta corresponds to the adhesion layer placed just below the Pd layer. Finally, the Co and Pd signal (yellow) show us the region and interface between 10nm Pd (111) and the 3nm $[Co(0.3nm)/Pd(0.7nm)]_3$ (111) layers.

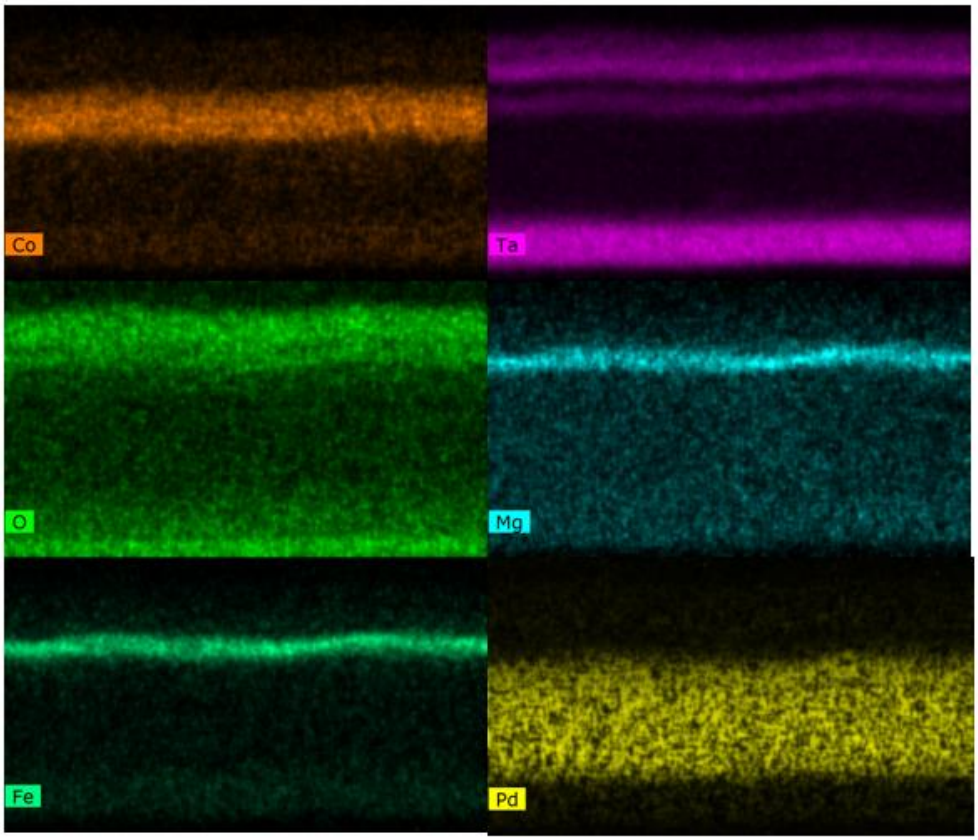

Figure 2-4.1.1: EDX mapping of the different elements in our stack. Each element is given by a distinct color shown in the figures' bottom left corner.
Stack: $Si/SiO_2/Ta(5nm)/Pd(10nm)/[Co(0.3nm)/Pd(0.7nm)]_3/Ta(1nm)/CFB(1.3nm)/MgO(2nm)$.

A key observation (Figure 2-4.1.1) is the diffusion of the Co through the 1nm Ta space layer, as Co appears as a single layer instead of two distinct layers. We suspect this diffusion to be a consequence of the annealing step performed after the thin film deposition. Figure 2-4.1.2 shows the HRTEM image of the stack, specifically of the Pd and the $[Co(0.3nm)/Pd(0.7nm)]_3$ layer.

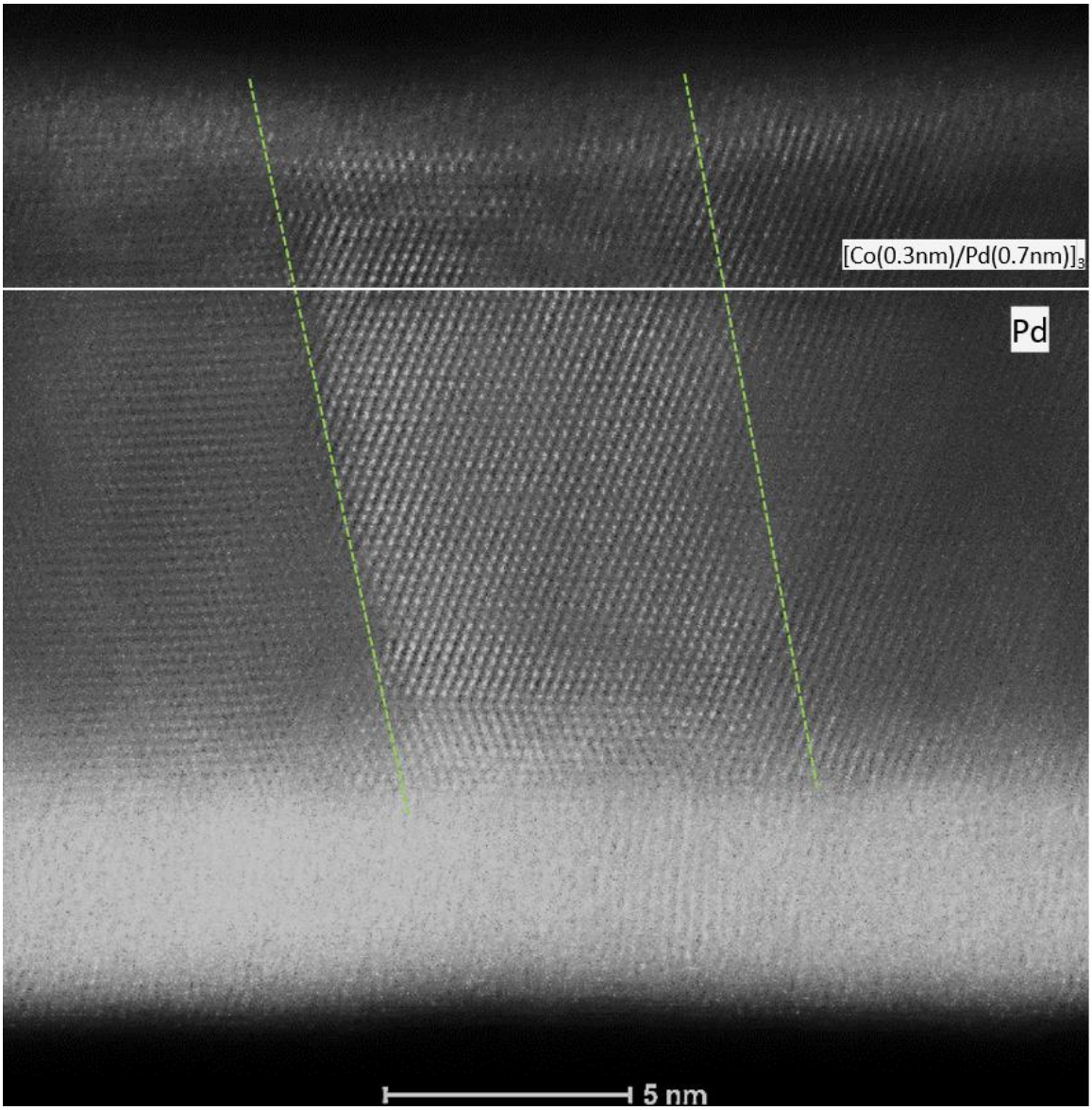

Figure 2-4.1.2: Cross-sectional HRTEM image of the stack. The green dotted line separates out a grain structure. The white line is a guide to the eye for the separation between $[Co(0.3nm)/Pd(0.7nm)]_3$ and Pd layers.
Stack: $Si/SiO_2/Ta(5nm)/Pd(10nm)/[Co(0.3nm)/Pd(0.7nm)]_3/Ta(1nm)/CFB(1.3nm)/MgO(2nm)$.

One can notice the presence of strong polycrystallinity in the Pd layer. We can see that the Pd (111) is made of several different grains, separated by a grain boundary (shown by green dotted

lines). These grains extend through the entire thickness of the Pd layer and have a lateral size of approximately 7-8nm in diameter. The region just above the Pd layer is the $[Co(0.3nm)/Pd(0.7nm)]_3$ layer structure, which shows some texture. The $[Co(0.3nm)/Pd(0.7nm)]_3$ layer follows the texture of the Pd (111) very well. This is also seen across several grains of Pd (111). In the $[Co(0.3nm)/Pd(0.7nm)]_3$ layer, there are regions of difference in contrast. Figure 2-4.1.3 shows the magnification of the regions with a distinction between the regions of dark and bright. The yellow region has higher brightness compared to the light blue region. The dotted white line approximately separates the Pd (111) from the $[Co(0.3nm)/Pd(0.7nm)]_3$ layer. The yellow region shows an area of higher crystallinity with respect to the blue regions. We cannot conclude from these TEM results if the regions of high and low crystallinity of the $[Co(0.3nm)/Pd(0.7nm)]_3$ layer have any chemical contrast. These low and high crystallinity regions are interspersed with each other.

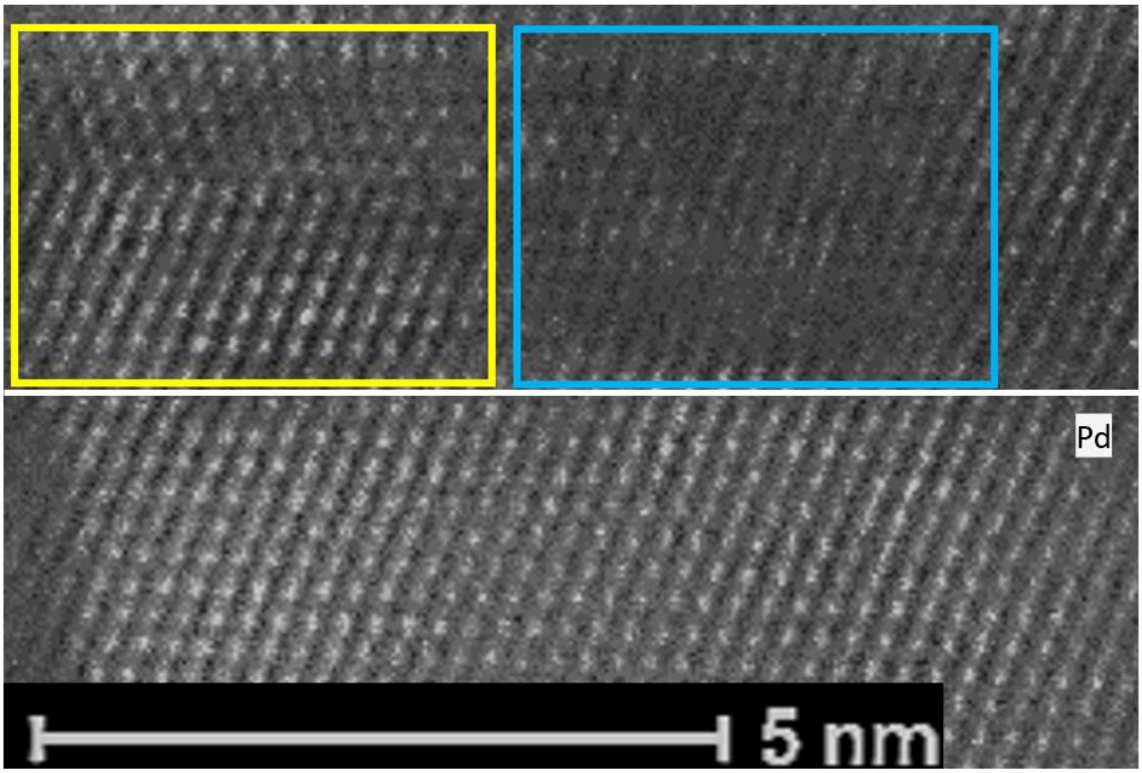

Figure 2-4.1.3: Magnification of the grains of Pd and $[Co(0.3nm)/Pd(0.7nm)]_3$ region which show regions of strong contrast. The yellow and blue squares separate regions of different contrast. Stack: $Si/SiO_2/Ta(5nm)/Pd(10nm)/[Co(0.3nm)/Pd(0.7nm)]_3/Ta(1nm)/CFB(1.3nm)/MgO(2nm)$.

2-4.2 XRD characterization

We also performed XRD on this sample to discern the crystallinity and crystallographic orientation of the films. Figure 2-4.2.1 shows the XRD data of the sample using a 2D detector of the Bruker D8. In this system, the machine is parked a specific 2θ value, and the signal is obtained. This allows us to get peaks from a range of different 2θ values as well as Γ spread of the crystallographic orientations. We have obtained two separate signals, centered at 2θ ~ 45 deg and 2θ ~ 70 deg. The horizontal axis gives us the value of 2θ, whereas the vertical axis gives us the Γ spread of the peaks.

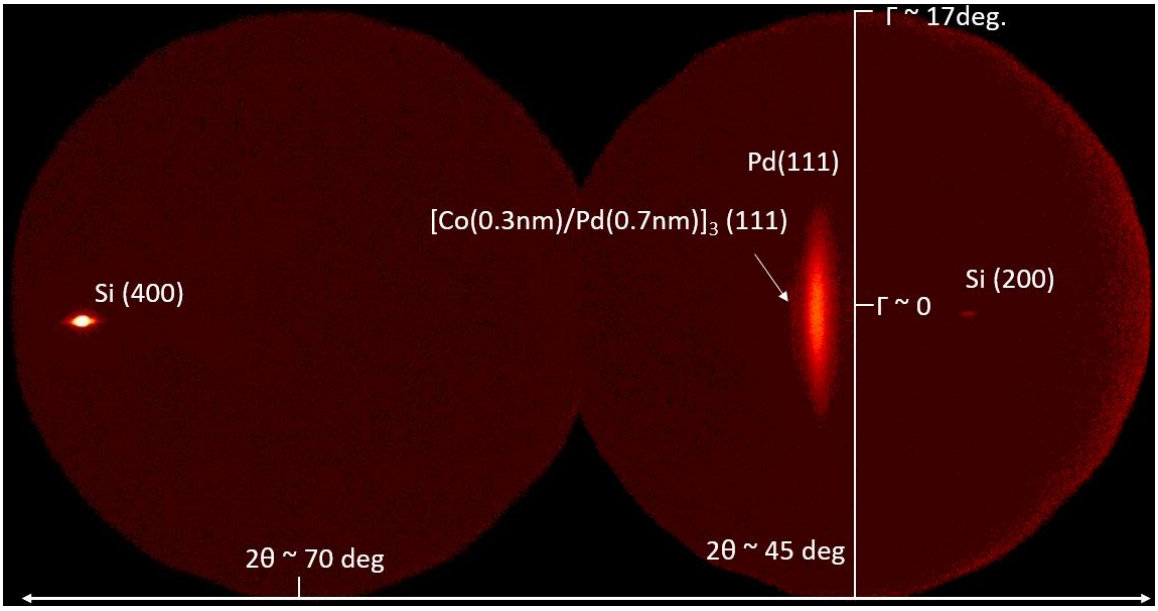

Figure 2-4.2.1: XRD data from 2D Bruker D8 detector. The horizontal axis of the circle corresponds to the 2θ. The center of the circle along the horizontal axis is shown (2θ = 70°, 45°). The vertical axis is the Γ spread of the peaks. The white line approximately shows the Γ spread. Stack: Si/SiO_2/Ta(5nm)/Pd(10nm)/[Co(0.3nm)/Pd(0.7nm)]$_3$/Ta(1nm)/CFB(1.3nm)/MgO(2nm).

We can notice several peaks that have come up. The high-intensity sharp peak is from the single-crystalline Si substrate corresponding to (400) crystallographic orientation. For the 2θ ~ 45 deg scan, we can see two major peaks. There is a very small low-intensity sharp peak corresponding to Si(200). There is a prominent high-intensity peak at the center of the 2θ ~ 48 deg scan. This peak corresponds to Pd (111), and a slight bulge across this peak is identified as [Co(0.3nm)/Pd(0.7nm)]$_3$ (111) peak. As one can see, the Pd (111) peak has some spread in Γ but doesn't form an entire circle (like a powder sample). This tells us that Pd (111) and [Co(0.3nm)/Pd(0.7nm)]$_3$ (111) have a preferential texture in the out-of-plane direction. The peaks can be integrated across Γ to obtain the 2θ scan of XRD.

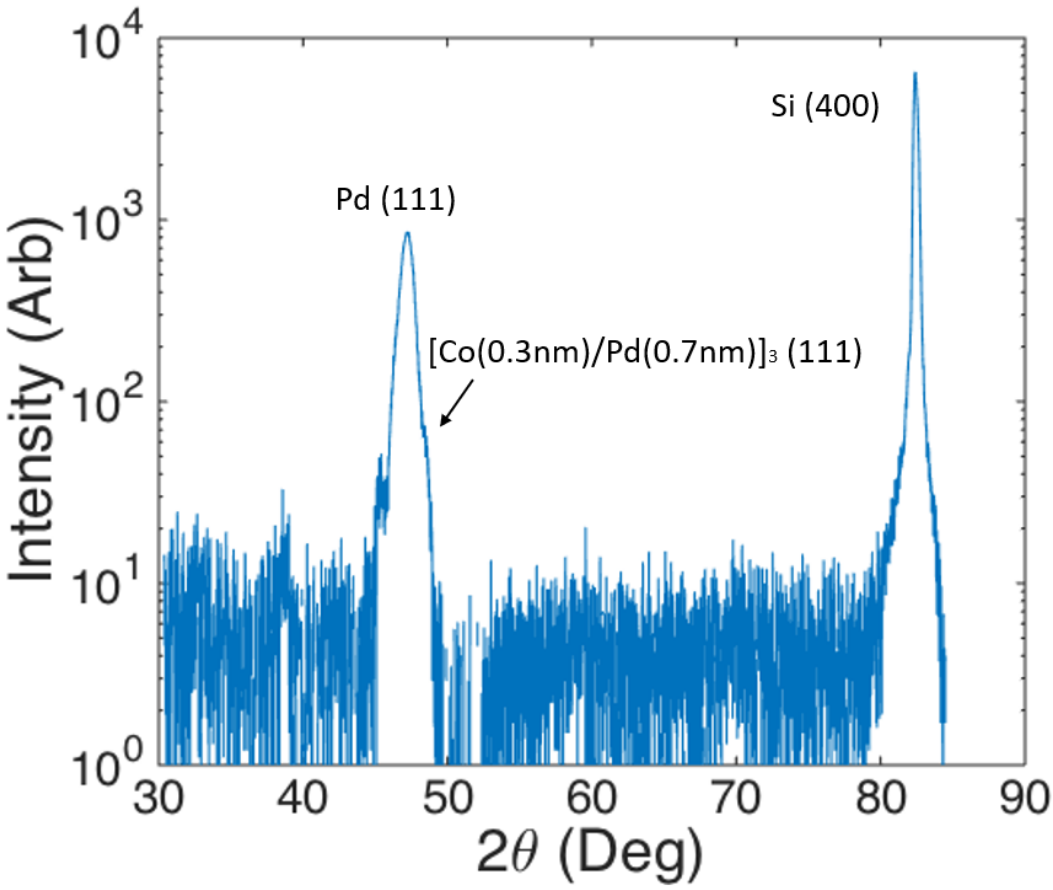

Figure 2-4.2.2: XRD characterization of the stack obtained by integrating the peaks in Γ. Stack: Si/SiO_2/Ta(5nm)/Pd(10nm)/[Co(0.3nm)/Pd(0.7nm)]$_3$/Ta(1nm)/CFB(1.3nm)/MgO(2nm).

CHAPTER 2-5: MAGNETIC AND ELECTRICAL CHARACTERIZATIONS

We performed AHE measurements (perpendicular magnetic field) on the annealed and fabricated stack to study the magnetic properties of the films. This was done by first completing the major loop measurement. Figure 2-5.1.1 shows the M-H for the major loop measurement.

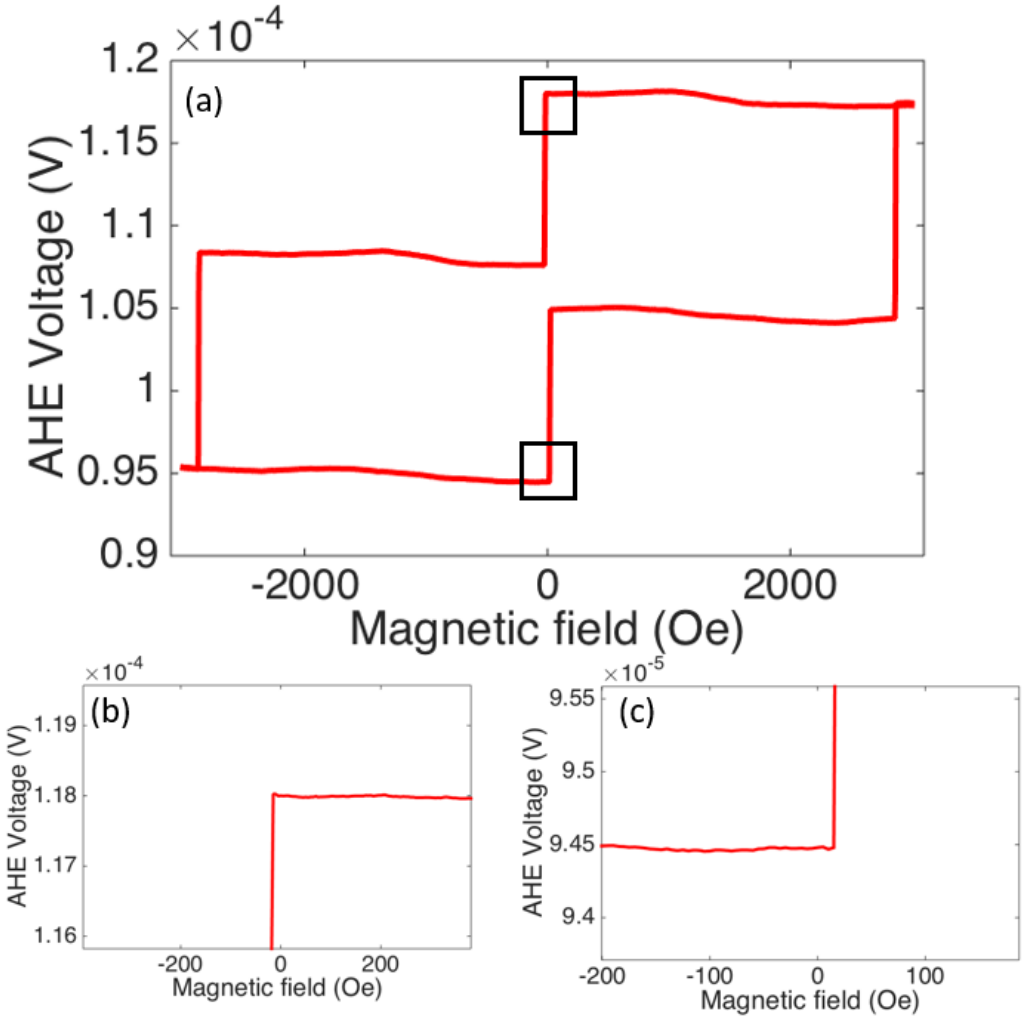

Figure 2-5.1.1: (a) AHE curve of the major loop measurement in the virgin state. The green and blue arrows correspond to the magnetization direction of CoFeB and $[Co(0.3nm)/Pd(0.7nm)]_3$, respectively. The switching close to 0 Oe is magnified to show the switching field of the CoFeB layer(b,c).Stack:Si/SiO_2/Ta(5nm)/Pd(10nm)/$[Co(0.3nm)/Pd(0.7nm)]_3$/Ta(1nm)/CFB(1.3nm)/MgO(2nm)/SiO_x (100nm) [102].

The major loop shows good switching behavior and squareness, indicating good PMA in the ferromagnets. We can observe very clear two-step switching in this M-H curve. Each switch corresponds to the magnetization reversal of one of the FMs. The blue arrow corresponds to the direction of the $[Co(0.3nm)/Pd(0.7nm)]_3$ layer, and the green arrow corresponds to the magnetization direction of the CoFeB layer. When we apply a large negative magnetic field (~ -3000 Oe), the magnetizations of both the FMs ($[Co(0.3nm)/Pd(0.7nm)]_3$ and CoFeB) are pulled down. Then, we slowly start increasing the magnetic field, and just around 0 Oe, we observe the first switch. This switch corresponds to the magnetization reversal of the CoFeB layer. CoFeB, being the softer of the two ferromagnets, is expected to switch first. As we further increase the magnetic field, we observe a second switch around ~ 2800 Oe. This switch corresponds to the switching of the $[Co(0.3nm)/Pd(0.7nm)]_3$ layer. We observe a similar behavior during the reverse scan. If one zooms in and follows the actual switching field of the CoFeB layer, it switches just after crossing 0 Oe during the field sweeps. The major loop is not enough to tell us the nature of the coupling between the two ferromagnets.

To further verify the magnetic properties and the exchange bias, we performed the minor loop measurement. In this measurement, we keep the $[Co(0.3nm)/Pd(0.7nm)]_3$ layer fixed (pointing downwards), and we simply measure the AHE signal of the CoFeB layer. The field sweep range is small (~ 300 Oe) to ensure that we don't affect the magnetization of the $[Co(0.3nm)/Pd(0.7nm)]_3$ layer. Figure 2-5.1.2 shows the leftward shift of the AHE curve of the

CoFeB layer. This shift is a result of the exchange bias field (section 2-1.2.2), from the $[Co(0.3nm)/Pd(0.7nm)]_3$. This ensures that one of the states (up or down) of the CoFeB layer is more stable than the other under no magnetic field. The minor loop clearly shows a bi-stable state of the CoFeB layer at 0 Oe. However, the leftward shift of the hysteresis indicates that the upward condition of the CoFeB is slightly more stable than the downward state of the CoFeB, while the $[Co(0.3nm)/Pd(0.7nm)]_3$ is pointing down. This indicates a weak anti-ferromagnetic coupling between the two FM layers [76,123,141,142].

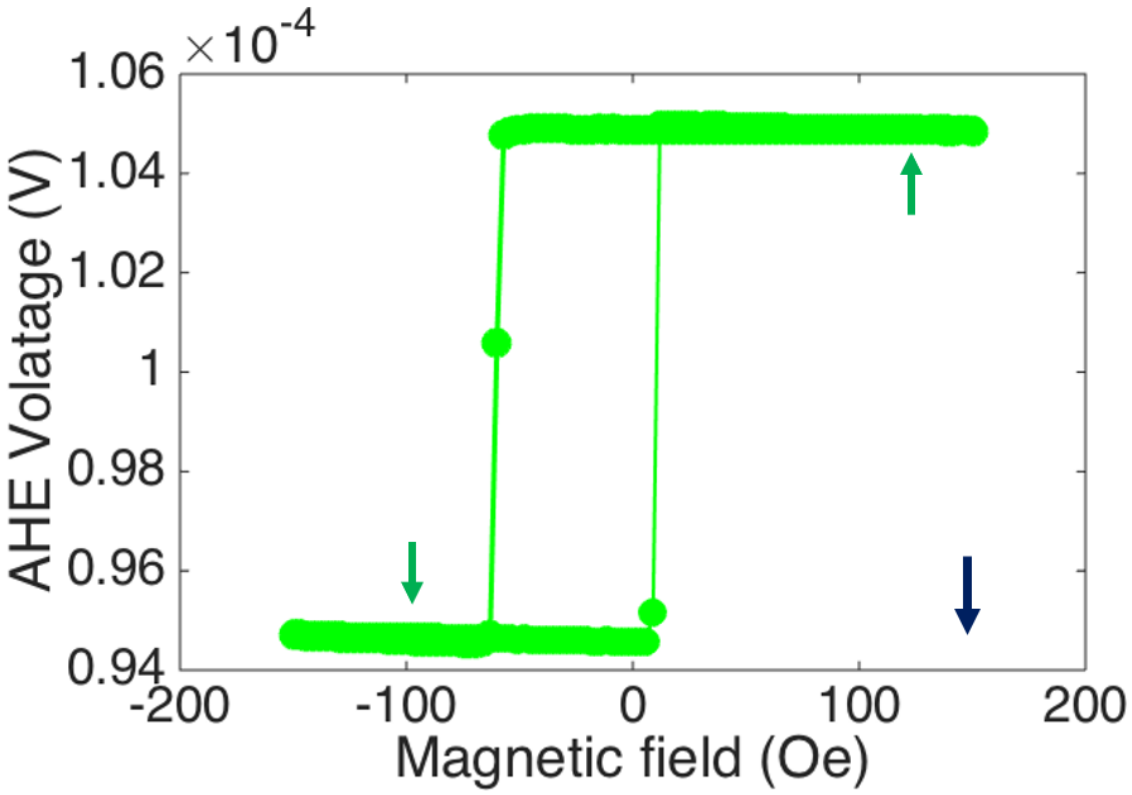

Figure 2-5.1.2: AHE minor loop of the CoFeB layer with $[Co(0.3nm)/Pd(0.7nm)]_3$ layer fixed in the downward direction. Red dotted line shows the shift in the M-H curve along X-axis due to the exchange bias field from $[Co(0.3nm)/Pd(0.7nm)]_3$ layer.
Stack:$Si/SiO_2/Ta(5nm)/Pd(10nm)/[Co(0.3nm)/Pd(0.7nm)]_3/Ta(1nm)/CFB(1.3nm)/MgO(2nm)/SiO_x$ (100nm) [102].

Next, we measure the minor and the major loop of the device under the effects of gate voltage (Figure 2-5.1.3). As one can see, under positive gate voltage, there is no change in the magnetic properties of the CoFeB layer. Upon applying a negative gate voltage, we see a permanent, irreversible change in the magnetic properties of the CoFeB layer. This irreversible change is a strong sign of the electrochemical reactions happening at the interface between the CoFeB and MgO layers. The change in the minor loop is observed as a change in coercivity of the film, which decreases with negative gate voltage. The CoFeB layer has gone from a bi-stable state at 0 Oe to a monostable state at the lowest gate voltage. This indicates that the anti-ferromagnetic coupling with $[Co(0.3nm)/Pd(0.7nm)]_3$ layer has gotten more robust under negative gate voltage. The CoFeB and $[Co(0.3nm)/Pd(0.7nm)]_3$ layers will now only have an antiferromagnetic coupling between them. This change in coupling can be characterized by simply measuring the exchange bias field on the CoFeB layer, given by the shift in the center of the minor loop.

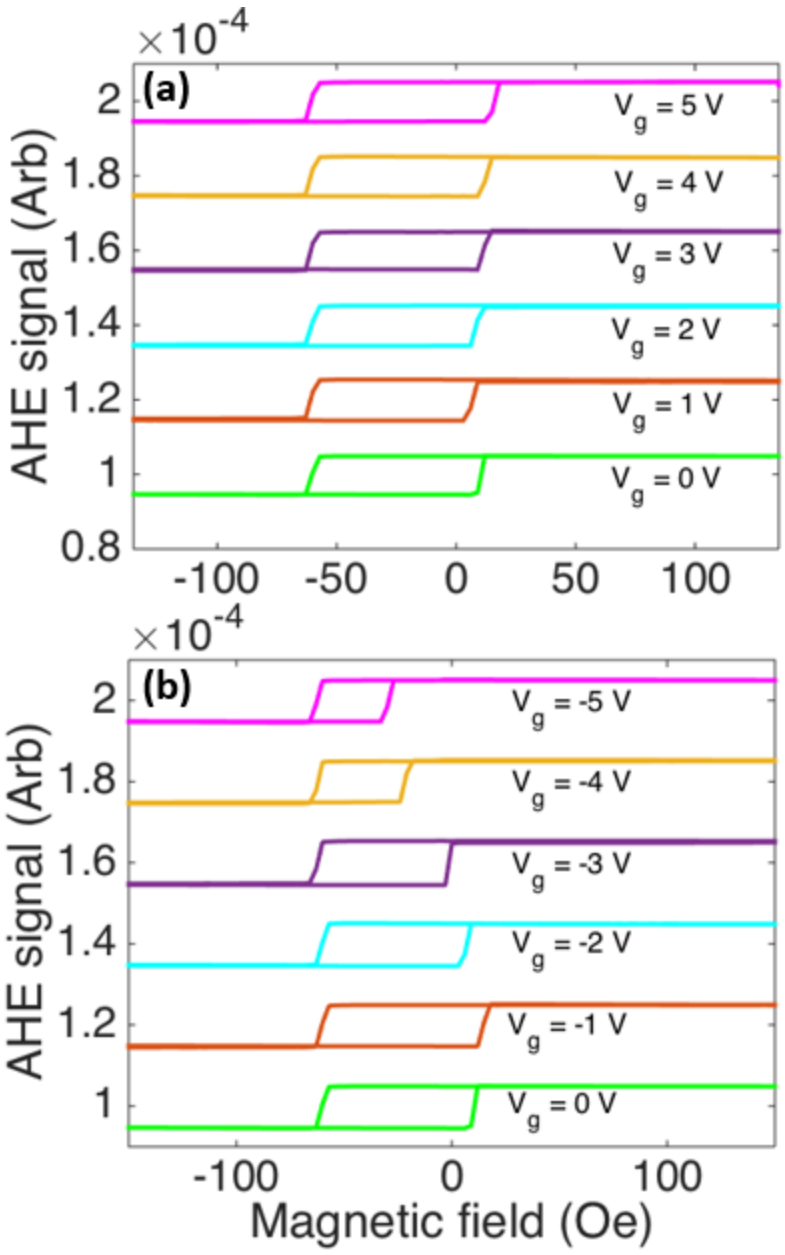

Figure 2-5.1.3: Change in the minor loop for the applied positive (a) and negative (b) gate voltages. Stack: Si/SiO_2/Ta(5nm)/Pd(10nm)/$[Co(0.3nm)/Pd(0.7nm)]_3$/Ta(1nm)/CFB(1.3nm)/MgO(2nm) /SiO_x (100nm) [102].

To realize if the ionic movement has affected the $[Co(0.3nm)/Pd(0.7nm)]_3$ layer, we also look at the major loop of the device. Figure 2-5.1.4 shows the changes in the major loop of the stack with respect to the gate voltage. The two-step switching shows some changes under the influence of negative gate voltage. The switch observed close to 0 Oe is the switching of the CoFeB layer and the switching observed at higher fields is due to the switching of the $[Co(0.3nm)/Pd(0.7nm)]_3$ layer. As evident from the figure, the switching field of CoFeB is the only one affected by the gate voltage. This change can be seen by the cross-over of the CoFeB switching field across 0 Oe. At V_g = -5 V, the switching field of CoFeB has completely crossed across 0 Oe, and the coupling has turned into a solid antiferromagnetic coupling with $[Co(0.3nm)/Pd(0.7nm)]_3$ layer. The switching field of the $[Co(0.3nm)/Pd(0.7nm)]_3$ layer is not affected by the gate voltage, which is a sign that the mobile Oxygen ions have not reached the $[Co(0.3nm)/Pd(0.7nm)]_3$ layer (Supplementary 2-S1).

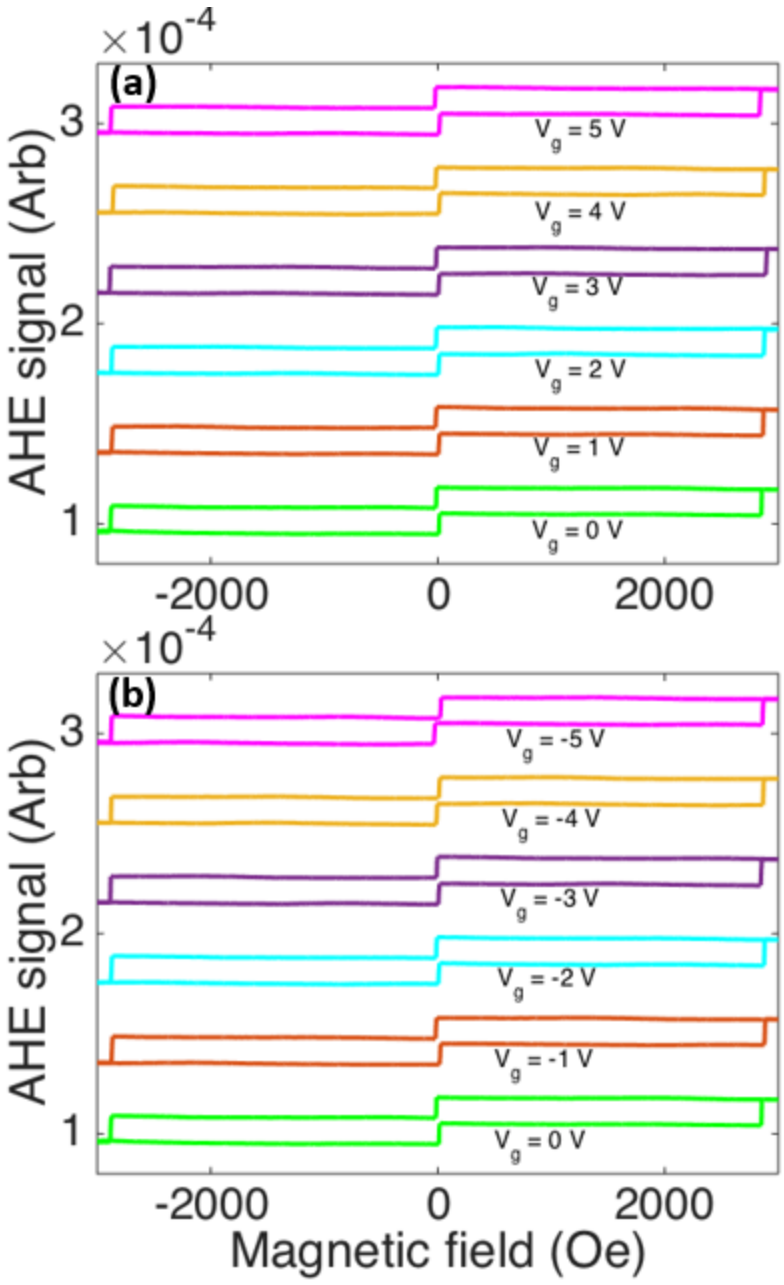

Figure 2-5.1.4: Change in the major loop with respect to different gate voltages. Stack: $Si/SiO_2/Ta(5nm)/Pd(10nm)/[Co(0.3nm)/Pd(0.7nm)]_3/Ta(1nm)/CFB(1.3nm)/MgO(2nm)/SiO_x$ (100nm) [102].

These changes in magnetic properties are summarized in Figure 2-5.1.5. The gate voltage is applied between +- 5 V, beyond which we observe a breakdown of the gate dielectric. The coercivity (Figure 2-5.1.5a) decreases quite significantly from about 36 Oe in the virgin state to about 16 Oe at V_g = -5 V. There is no change in the AHE coefficient, indicating that the saturation magnetization is not affected too much by the gate voltage (Supplementary 2-S1). Figure 2-5.1.5 (b) shows the change in the exchange bias field on the FM1 layer. At V_g = -5 V, the exchange bias field has almost doubled in its magnitude.

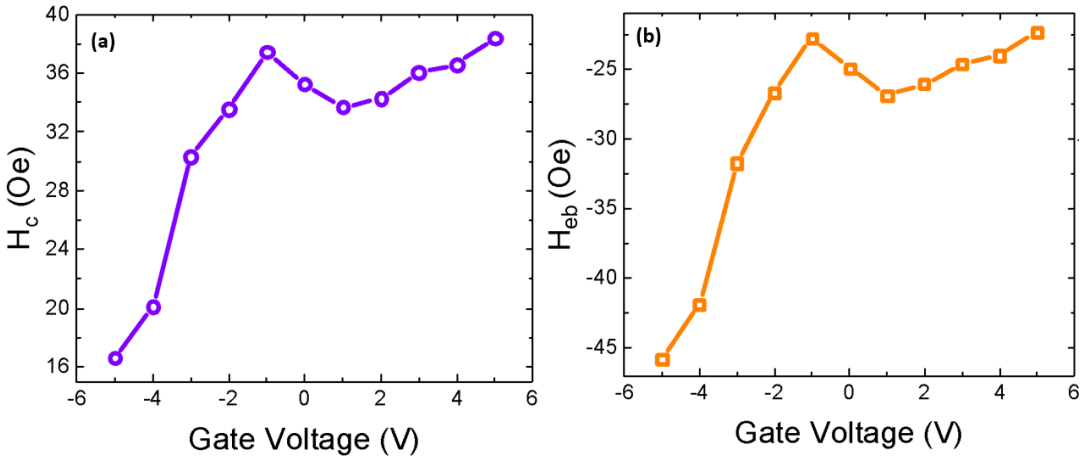

Figure 2-5.1.5: Change in coercivity (a), exchange bias field (b), of CoFeB layer, with respect to the gate voltage.
Stack:Si/SiO_2/Ta(5nm)/Pd(10nm)/[Co(0.3nm)/Pd(0.7nm)]$_3$/Ta(1nm)/CFB(1.3nm)/MgO(2nm)/Si O_x (100nm) [102].

CHAPTER 2-6: DISCUSSION

To understand these changes in magnetic properties, we need to look at the underlying mechanisms behind these changes. We believe that negatively charged mobile oxygen ions cause these changes in the magnetic properties. When we apply a negative gate voltage, these mobile oxygen ions are activated and move towards the CoFeB/MgO interface. We notice that the magnetic properties don't change too much at V_g = -1, -2 V but start changing quite suddenly at V_g < -2 V. As mentioned in section 2-1.2.4, the movement of oxygen ions is expected to be dominated by the ionic migration energy barrier. As a result, the oxygen migration is supposed to be activated once the magnitude of the gate voltage is strong enough to overcome the obstacle.

The PMA, in CoFeB, is possible due to careful overlapping of the atomic orbitals between transition metals and oxygen. As these oxygen ions move towards the CoFeB/MgO interface, they over oxidize this interface, disturbing the orbital overlapping. Therefore, this destroys the PMA of the CoFeB layer, leading to a decrease in coercivity. There could be two sources of exchange bias field increase: 1) exchange coupling constant 2) decrease in thickness of FM1. The simplest way to affect the exchange coupling constant is for the oxygen ions to reach the Ta spacer layer. This would lower the conductivity of the Ta layer, thereby decreasing the exchange coupling. If that happens, the ionic movement can be divided into two parts a) when the Oxygen is present inside CoFeB (low gate voltage magnitude) b) when Oxygen moves into the Ta layer (high gate voltage magnitude). In the first part of the operation, we shouldn't see too much change in the coupling constant. As we lower the gate voltage further, we would see a transition in the exchange bias field, since the coupling constant would be affected (reduced) due to the movement of Oxygen into the Ta layer. However, our experimental data shows that the exchange bias field constantly increases

in magnitude, with no signs of transition. Moreover, the fact that the $[Co(0.3nm)/Pd(0.7nm)]_3$ layer coercivity has not been affected by the negative gate voltage means that the mobile oxygen ions have not yet reached the $[Co(0.3nm)/Pd(0.7nm)]_3$ layer. Furthermore, there is no change in saturation magnetization and the squareness of the loop at V_g = -5V, which shows that the CoFeB PMA has not entirely been destroyed. All these signs point to the fact that the oxygen movement is restricted to only the top half of the CoFeB layer without destroying the whole magnetism of the CoFeB layer. The second possibility contributing to an increase in the exchange bias field is the decrease in thickness of the FM1 layer. The overoxidation of the CoFeB/MgO interface increases the thickness of the dead layer. This increase in the thickness of the dead layer lowers the effective thickness of the FM1 layer, thereby increasing the exchange bias field.

It should be noted that the SW model, used to derive exchange bias field (section 2-1.2.3), is based on the assumption that the FM1 is a single domain. However, the 1/thickness dependence is observed in several exchange bias experiments particularly when the FM1 thickness is lower than the domain wall width [136]. With 1/thickness behavior, the decrease in effective thickness is estimated to be around ~ 45% at V_g = -5 V, assuming no changes in saturation magnetization or the exchange coupling constant.

Next, we try to analyze the final magnetic anisotropy of the CoFeB layer, after applying a large negative gate voltage. The results point to a reduction of interfacial PMA of the CoFeB layer. Two significant effects might come into play 1) Bulk anisotropy 2) Thermal fluctuations (superparamagnetic domains). The CoFeB anisotropy in the virgin state was a combination of bulk in-plane anisotropy and interfacial perpendicular anisotropy. The interfacial anisotropy dominates due to the orbital overlapping. Once this interfacial PMA is reduced (after applying negative gate voltage), the bulk anisotropy can become a player deciding the magnetic anisotropy. However, it

is also well known that the FM layer might go into a superparamagnetic state when the thickness goes too low due to spontaneous thermal switching of the magnetic domains. Both these mechanisms can lead to a decrease in PMA and can explain the experimental data.

We used a thermally oxidized Si substrate for the growth of our films. This is particularly advantageous for industry applications, which typically use these substrates. However, this can be improved if we use a more crystalline substrate to grow the magnetic layers epitaxially. Zhang et al used MgO substrate to develop L10 phase of FePd layers [140]. This allows us to design high anisotropy materials which can be used for MRAM-based applications. This is highly desirable for sizeable thermal stability magnetic devices.

We also discuss the kinetics of the mobile oxygen ions. Two significant sources dictate the movement of oxygen ions: lattice constant and migration energy barrier (section 2-1.2.4). The lattice constant dominates at high electric fields. In this case, the time of gate voltage exposure can come into play. Hence, if we apply a gate voltage for long enough, we will deplete the oxygen ions from the gate dielectric. But, at a low electric field (like our case), the migration energy barrier dominates the movement of oxygen. In that case, only the oxygen ions that are stuck inside a well with lower potential depth than the gate voltage will escape. This is particularly advantageous for applications since the oxygen movement will no longer depend on the time of exposure of the gate voltage.

A key disadvantage of using the magneto-ionic device for VN systems is the speed. Since the magneto-ionic effect is not the fastest physical mechanism, this may not be a significant concern for neuromorphic applications. In neuromorphic systems, speed is not a critical concern. The focus is on power consumption. The ionic movement is advantageous for these systems since they can emulate a neuron very well. Another concern is the irreversibility of the device. The irreversibility

is dependent on the choice of the ionic gate. The irreversibility is undesirable, which requires devices to be programmed multiple times (eg: RAM). However, for applications that need to be programmed only once (eg: ROM), the irreversibility is useful as we demonstrated in trhis thesis for the first time.

CHAPTER 2-7: CONCLUSION

In this second part of the thesis, we designed a magneto-ionic device for OTP and neuromorphic applications. We started by creating a device that would allow us to switch the magnetization of the ferromagnet at zero magnetic field. For that, we used exchange bias as one of the ways to engineer the device. The exchange bias was created by designing a FM1/NM/FM2 structure. We deposited the film stack using DC magnetron sputtering. The FM1 layer was CoFeB with interfacial PMA. The interfacial PMA is key to making magneto-ionic devices work since it can be affected by ionic movement. The second FM layer, which would provide exchange bias, was chosen to be $[Co(0.3nm)/Pd(0.7nm)]_3$ layer. $[Co(0.3nm)/Pd(0.7nm)]_3$ layer has a strong PMA that can create a good exchange bias system with the CoFeB layer. The spacer layer between them was a 1nm thin Ta layer. This spacer layer (and its thickness) are key to determining the kind of exchange bias present in the stack. Pd (111) was used to grow $[Co(0.3nm)/Pd(0.7nm)]_3$ (111), to enhance the PMA through magnetocrystalline anisotropy of the $[Co(0.3nm)/Pd(0.7nm)]_3$ layer.

Material characterization of the film was done by using HRTEM and XRD. EDX allowed an analysis of the chemical signatures of different thin films, which showed each layer distinctly. The EDX mapping also helped us analyze the effects of different atomic diffusions that might come into play during the high-temperature annealing process. HRTEM shed light on the crystallinity of Pd (111) and $[Co(0.3nm)/Pd(0.7nm)]_3$ (111) thin films. Furthermore, we used XRD to characterize the crystallinity of the films. We observed two key peaks coming from the film stack coming from Pd (111) and $[Co(0.3nm)/Pd(0.7nm)]_3$ (111). Both the peaks indicated texture in the film along the out-of-plane direction.

Magnetic characterization sheds light on the magnetic anisotropies of the films and the exchange bias between them. The stack showed good PMA properties with a two-step switching for a major loop. We also verified the weak anti-ferromagnetic coupling by measuring the minor loop and characterized the exchange bias field. These stacks were then fabricated into Hall bars with a top SiO_x ionic gate.

Electrical measurements of the minor loop showed strong irreversible changes in the magnetic properties of the CoFeB layer at negative gate voltage. This change in the magnetic properties of the CoFeB layer is attributed to interfacial overoxidation, driven by ionic movement from the gate dielectric. We saw a decline in the coercive field, whereas the exchange bias field increased in magnitude. Each of these magnetic properties and the changes in them was analyzed.

SUPPLEMENTARY FOR PART-2

2-S1 Other magnetic parameters

In this section, I will show the magnetic parameters of the magneto-ionic device that are not affected. Two major parameters are unaffected and key to understanding the underlying mechanism/physics: Saturation magnetization of CoFeB layer and coercive field of $[Co(0.3nm)/Pd(0.7nm)]_3$ layer. The changes in saturation magnetization of CoFeB can become an important player in the exchange bias field, as the exchange bias field is inversely proportional to the saturation magnetization.

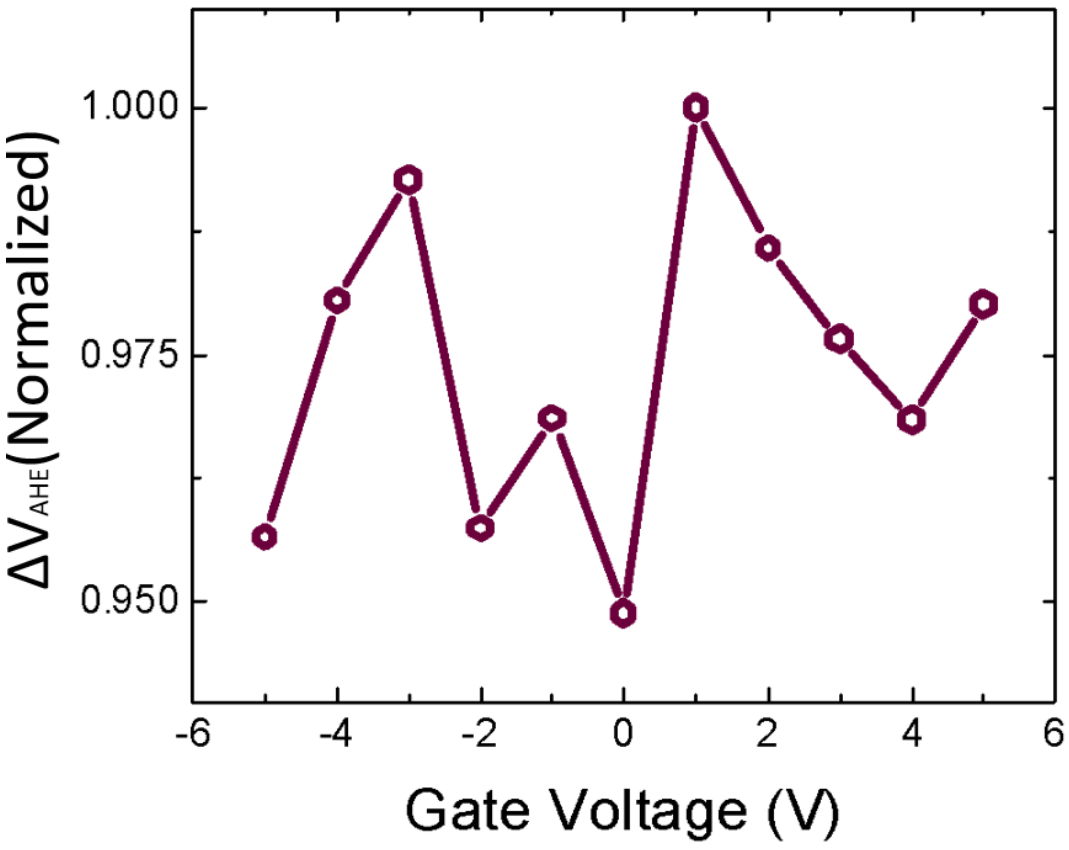

Figure 2-S1.1: Changes in ΔV_{AHE} of the CoFeB layer, from the minor loop, with respect to the gate voltage.
Stack:Si/SiO_2/Ta(5nm)/Pd(10nm)/[Co(0.3nm)/Pd(0.7nm)]$_3$/Ta(1nm)/CFB(1.3nm)/MgO(2nm)/Si O_x (100nm) [102].

The saturation magnetization of the CoFeB layer is given by the difference between the high-state and low-state AHE voltage obtained. We define the normalized ΔVAHE as:

$$\Delta V_{AHE} = \frac{V_{AHE}^{HS} - V_{AHE}^{LS}}{\max\left(V_{AHE}^{HS} - V_{AHE}^{LS}\right)}, \quad (2\text{-}3.1.1)$$

where V_{AHE}^{HS} is the AHE voltage for the high state and V_{AHE}^{LS} is the AHE voltage for the low state. Figure 2-S1.1 shows this value changes with respect to the gate voltage. ΔV_{AHE} is a good indication of the saturation magnetization of the FM layer. This shows us that the saturation magnetization of the CoFeB layer in the device is not affected too much by the ionic movement. Next, we look at the switching field of the [Co(0.3nm)/Pd(0.7nm)]$_3$ layer, which gives us the coercivity of the film. This is obtained from the major loop of the device.

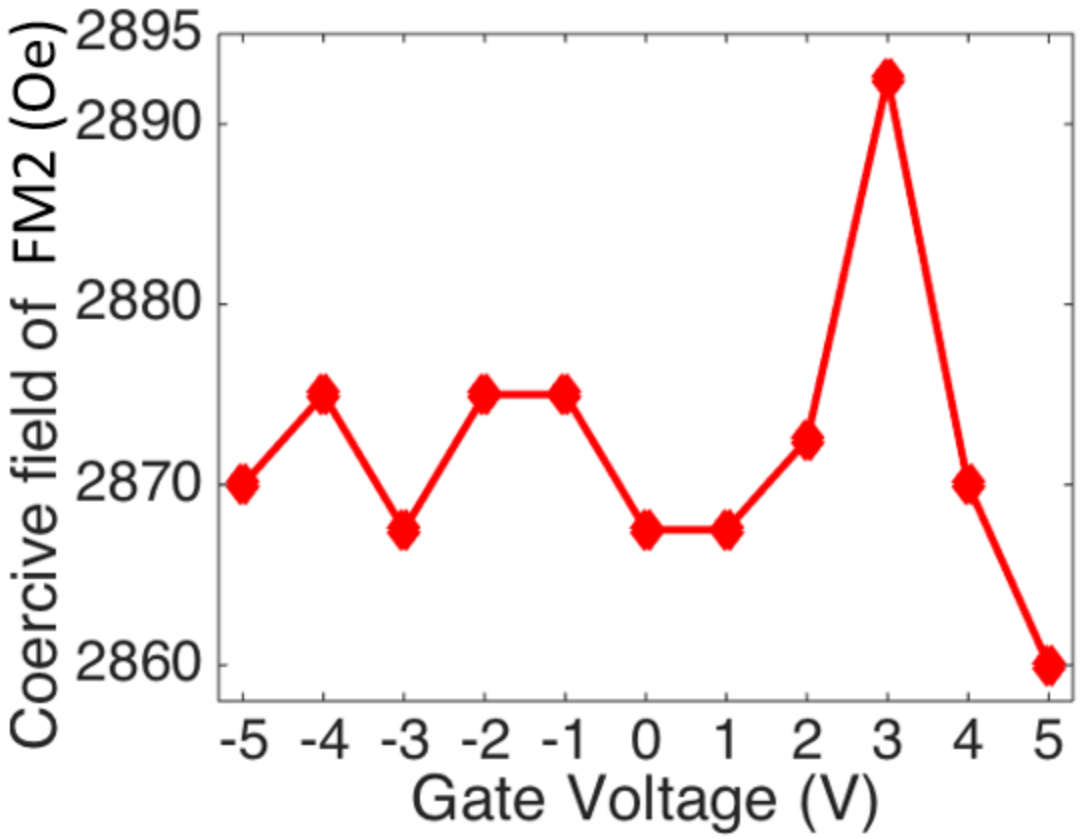

Figure 2-S1.2: Effect of gate voltage on the coercive field of the $[Co(0.3nm)/Pd(0.7nm)]_3$ layer. Stack:$Si/SiO_2/Ta(5nm)/Pd(10nm)/[Co(0.3nm)/Pd(0.7nm)]_3/Ta(1nm)/CFB(1.3nm)/MgO(2nm)/SiO_x$ (100nm) [102].

Figure 2-S1.2 shows the change in the coercive field of the $[Co(0.3nm)/Pd(0.7nm)]_3$ layer for gate voltage. The coercive field of the $[Co(0.3nm)/Pd(0.7nm)]_3$ layer doesn't show any major changes for gate voltage. This shows that the coercivity is quite constant (~ 2870 Oe) and the ionic movement hasn't affected the $[Co(0.3nm)/Pd(0.7nm)]_3$ layer yet. This is a sign that the mobile Oxygen ions have probably not reached the $[Co(0.3nm)/Pd(0.7nm)]_3$ layer at Vg ~ -5 V. These

results support the idea that the mobile Oxygen ions are still limited only to the CoFeB layer and the change in exchange bias field is a result of mostly changes in the thickness of the CoFeB layer.

REFERENCES

[1] E. Mollick, “Establishing Moore ’ s Law,” in IEEE Annals of the History of Computing, **28**, 3 (2006).

[2] Gordon E. Moore, “Cramming more components into integrated circuits” Electronics, **38**, 8 (1965).

[3] JP Wang et al., “A Pathway to Enable Exponential Scaling for the Beyond-CMOS Era” Proceedings of 54th Annual Design Automation Conference, **16**, 1 (2017).

[4] H. Zhang et al. “Topological insulators in Bi_2Se_3, Bi_2Te_3 and Sb_2Te_3 with a single Dirac cone on the surface,” Nat. Phys.,**5** ,438 (2009).

[5] T. Yokoyama and S. Murakami, “Spintronics and spincaloritronics in topological insulators,” Phys. E Low-Dimensional Syst. Nanostructures, **55** , 1 (2014).

[6] C. Felser and X. L. Qi, “Topological insulators,” MRS Bulletin, **39**, 10 (2014).

[7] J. Puebla et al. “Spintronic devices for energy-efficient data storage and energy harvesting,” Commun. Mater., **1**, 24 (2020).

[8] J. Åkerman et al. “CMOS-compatible spintronic devices : a review,” Semicond. Sci. Technol. **31**, 113006, (2016).

[9] J. Torrejon et al., “Neuromorphic computing with nanoscale spintronic oscillators,” Nature, **547**, 428 (2017).

[10] W. F. Egelhoff Jr et al., “Physical Critical challenges for picoTesla magnetic-tunnel-junction sensors,” Sensors Actuators A, **155**, 217 (2009).

[11] X. Wang et al. “Spintronic Memristor Temperature Sensor,” IEEE Elec. Dev. Lett., **31**, 1 (2010).

[12] P. Villard et al., “A GHz Spintronic-Based RF Oscillator,” IEEE J. Solid-State Circuits, **45**, 1, (2010).

[13] R. Ramesh, “A new spin on spintronics” Nat.Mat.. **9**, 380 (2010).

[14] S. Ikeda et al., “A perpendicular-anisotropy CoFeB – MgO magnetic tunnel junction,” Nat. Mater., **9**, 721 (2010).

[15] S. Tehrani et al., “Recent Developments in Magnetic Tunnel Junction MRAM,” IEEE Trans. Magn.,**36**, 5, (2000).

[16] N. Liebing et al. “Tunneling Magnetothermopower in Magnetic Tunnel Junction Nanopillars,” Phys. Rev. Lett., **107**, 177201, (2011).

[17] J. Mathon and A. Umerski, “Theory of tunneling magnetoresistance of an epitaxial Fe/Mgo/Fe (001) juntion” Phys. Rev. B, **63**, 220403 (2001).

[18] J. Inoue and S. Maekawa, “Theory of tunneling magnetoresistance in granular magnetic films,” Phys. Rev. B, **53**, R11927(R), (1996).

[19] M. D. Stiles and A. Zangwill, “Anatomy of spin-transfer torque,” Phys. Rev. B, **66**, 014407, (2002).

[20] J. D. Costa et al. “High power and low critical current density spin transfer torque nano-oscillators using MgO barriers with intermediate thickness,” Sci. Rep., **7**, 7237, (2017).

[21] L. Desplat and J-V. Kim "Quantifying the Thermal Stability in Perpendicularly Magnetized Ferromagnetic Nanodisks with Forward Flux Sampling," Phys. Rev. Appl., **14**, 064064, (2020).

[22] S. Manipatruni et al., "Scalable energy-efficient magnetoelectric spin–orbit logic," Nature, **565**, 35 (2019).

[23] M. Kurpas et al. "Spin-orbit coupling and spin relaxation in phosphorene : Intrinsic versus extrinsic effects," Phys. Rev. B, **94,** 155423 (2016).

[24] L.H. Thomas, "The motion of spinning electron," Nature, **117**, 2945 (1926).

[25] P. B. Ndiaye et al. "Dirac spin-orbit torques and charge pumping at the surface of topological insulators," Phys. Rev. B, **96**, 014408 (2017).

[26] A. R. Mellnik et al., "Spin-transfer torque generated by a topological insulator," Nature, **511**, 449, (2014).

[27] L. Ortiz at al. "Generic helical edge states due to Rashba spin-orbit coupling in a topological insulator," Phys. Rev. B, **93**, 205431 (2016).

[28] F. Auvray et al. "Spin accumulation at nonmagnetic interface induced by direct Rashba–Edelstein effect," J. Mater. Sci. Mater. Electron.,**29**, 15664, (2018).

[29] G. Dresselhaus, "Spin-Orbit Coupling Effects in Zinc Blende Structures" Phys. Rev., **100**, 580, (1955).

[30] E. Saitoh et al., "Conversion of spin current into charge current at room temperature : Inverse spin- Hall effect Inverse spin-Hall effect," Appl. Phys. Lett. **88**, 182509 (2006).

[31] B. F. Miao at al. “Inverse Spin Hall Effect in a Ferromagnetic Metal,” Phys. Rev. Lett., **111**, 066602, (2013).

[32] O. Mosendz et al., “Detection and quantification of inverse spin Hall effect from spin pumping in permalloy/normal metal bilayers,” Phys. Rev. B, **82**, 214403 (2010).

[33] K. Ando and E. Saitoh, “Observation of the inverse spin Hall effect in silicon,” Nat. Commun., **3**, 629 (2012).

[34] K. L. Wang et al. “Spintronics of Topological Insulators,” Handbook of Spintronics (Springer, Dordrecht, 2015).

[35] V. Galitski and I. B. Spielman, “Spin – orbit coupling in quantum gases,” Nature, **494**, 49 (2013).

[36] A. Manchon et al. “New perspectives for Rashba spin – orbit coupling,” Nat. Mat.,**14**, 871 (2015).

[37] T. Sugimoto and K. Fukutani, “Electric-field-induced nuclear-spin flips mediated by enhanced spin – orbit coupling,” Nat. Phys. **7**, 307 (2011).

[38] Y. Wen et al., “Temperature dependence of spin-orbit torques in Cu-Au alloys,” Phys. Rev. B, **95**, 104403 (2017).

[39] M. Jamali et al., “Giant Spin Pumping and Inverse Spin Hall Effect in the Presence of Surface and Bulk Spin-Orbit Coupling of Topological Insulator Bi_2Se_3,” Nano Lett., **15**, 7126 (2015).

[40] N. H. D. Khang et al., “A conductive topological insulator with large spin Hall effect for ultralow power spin–orbit torque switching,” Nat. Mater., **17**, 808 (2018).

[41] M. DC et al., “Room-temperature high spin-orbit torque due to quantum confinement in sputtered $Bi_xSe_{(1-x)}$ films,” Nat. Mater., **17**, 800 (2018).

[42] Y. Lv et al., “Unidirectional spin-Hall and Rashba-Edelstein magnetoresistance in topological insulator-ferromagnet layer heterostructures,” Nat. Commun., **9**, 111 (2018).

[43] P. Sahu et al., “Room Temperature Mott Hopping and Spin Pumping characterization og Amorphous Gd-alloyed Bismuth Selenide,” arXiv:1911.03323.

[44] K. Harii et al. “Frequency dependence of spin pumping in $Pt/Y_3Fe_5O_{12}$” Phys, J Appl, **105**, 116105, (2011).

[45] Y. T. Chen et al., “Theory of spin Hall magnetoresistance (SMR) and related phenomena,” J. Phys. Cond. Mat., **28**, 103004 (2016).

[46] A. Fert et al. “Perpendicular magnetoresistance in magnetic multilayers: Theoretical model and discussion” J. Appl. Phys., **75**, 6693, (1994).

[47] J. Kim et al., “Spin-Hall effect MRAM based cache memory: A feasibility study,” in Device Research Conference - Conference Digest, DRC, 2015, pp. 117–118. (2015).

[48] L. Liu, et al. “Spin-Torque Switching with the Giant Spin Hall Effect of Tantalum,” Science., **336**, 6081 (2012).

[49] C. O. Avci et al. “Unidirectional spin Hall magnetoresistance in ferromagnet/normal metal bilayers,” Nat. Phys., **11**, 570 (2015).

[50] S. S. Zhang and G. Vignale, “Theory of unidirectional spin Hall magnetoresistance in heavy-metal / ferromagnetic-metal bilayers,” Phys. Rev. B, **94**, 140411, (2016).

[51] C. O. Avci et al. “A multi-state memory device based on the unidirectional spin Hall magnetoresistance,” Appl. Phys. Lett., **110**, 203506, (2018).

[52] D. Harrison, “Theory of the sputtering process,” Phys. Rev., **102**, 1473 (1956).

[53] N. Roschewsky et al., “Spin-orbit torque and Nernst effect in Bi-Sb/Co heterostructures,” Phys. Rev. B, **99**, 195103 (2019).

[54] P. Sahu et al. “Weak antilocalization and low-temperature characterization of sputtered polycrystalline bismuth selenide,” Appl. Phys. Lett. **112**, 122402, (2018).

[55] M. Zubair Ansari and N. Khare, “Thermally activated band conduction and variable range hopping conduction in Cu_2ZnSnS_4 thin films,” J. Appl. Phys., **117**, 025706 (2015).

[56] V. P. Arya et al. “Effect of magnetic field on Mott’s variable-range hopping parameters in multiwall carbon nanotube mat,” J. Phys. Condens. Matter, **24**, 245602, (2012).

[57] N. F. Mott, “Conduction in non-crystalline materials,” Philos. Mag.,**19**, 160 (1969).

[58] A. L. Efros and B. I. Shklovskii, “Coulomb gap and low temperature conductivity of d isordered systems,” J. Phys. C Solid State Phys., **8**, 4 (1975).

[59] M. DC, “High Charge-to-Spin and Spin-to-Charge Conversion Enhanced by Quantum Confinement Effect in Sputtered Topological Insulator Thin Films,” UMN Phd thesis,. January, (2019).

[60] T. J. Peterson et al. “Annealing Temperature Effects on Spin Hall Magnetoresistance in Perpendicularly Magnetized W/CoFeB Bilayers”, IEEE Transaction on magnetics, **55**, 2 (2018).

[61] X. Tao et al. "Self-consistent determination of spin Hall angle and spin diffusion length in Pt and Pd: The role of the interface spin loss" Science Advance **4**, 6 (2018).

[62] M. DC et al. “Observation of High Spin-to-Charge Conversion by Sputtered Bismuth Selenide Thin Films at Room Temperature” Nano Lett. **19**, 4836 (2019).

[63] M. DC et al. “Room-temperature spin-to-charge conversion in sputtered bismuth selenide thin films via spin pumping from yttrium iron garnet” Appl. Phys. Lett. **114**, 102401 (2019).

[64] Y. Fan et al. “Spin pumping and large field-like torque at room temperature in sputtered amorphous WTe_{2-x} films” APL Mat. **8**, 041102 (2020).

[65] A.S. Everhardt et al. "Tunable charge to spin conversion in strontium iridate thin films" Phys. Rev. Mat. **3**, 151201(R) (2019).

[66] T. Nan et al. "Anisotropic spin-orbit torque in epitaxial $SrIrO_3$ by symmetry design" PNAS, **116**, 33 (2019).

[67] P. Dang et al. "Materials relevant to realizing a field effect transistor based on spin orbit torques" IEEE Journal on Exploratory Solid-State Computational Devices and Circuit, **5**, 2 (2019).

[68] Pi, U. H. et al. Tilting of the spin orientation induced by Rashba effect in ferromagnetic metal layer, Appl. Phys. Lett., **97**, 162507 (2019).

[69] K. Oura et al. "Surface Science" (Springer, 2003).

[70] P. Noel et al. "Negligible thermal contributions to the spin pumping signal in ferromagnetic metal-Platinum bilayers" Journal of Applied Physics, **127**, 163907 (2020).

[71] R. K. Bennet et al. "Temperature dependence of the anomalous Nernst coefficient for $Ni_{80}Fe_{20}$ determined with metallic nonlocal spin valves" AIP Advances, **10**, 065127 (2020).

[72] A. Bose et al. "Direct detection of spin Nernst effect in platinum" Appl. Phys. Lett. **112**, 162401 (2018).

[73] Z. Liang et al. "Performance Characterization and Majority Gate Design for MESO-based Circuits" IEEE Journal of Exploratory Solid-State Computational Devices and Circuits, **4**, 2 (2018)

[74] J. Kim et al., "Spin-Hall effect MRAM based cache memory: A feasibility study," in Device Research Conference - Conference Digest, DRC, 117-118 (2015).

[75] Q. Shi et al. "A spin Hall effect-based multi-level cell for MRAM," IEEE/ACM Int. Symp. Nanoscale Archit., 143-144 (2016).

[76] R. A. Duine et al. "Synthetic antiferromagnetic spintronics," Nat. Phys., **14**, 217 (2018).

[77] D. Aswachalom and M. Flatte, "Challenges for semiconductor spintronics," Nat. Phys., **3**, 153 (2009).

[78] T. Jungwirth et al. "The multiple directions of antiferromagnetic spintronics," Nat. Phys., **14**, 200 (2018).

[79] M. D. Godfrey and D. F. Hendry, "The Computer as von Neumann Planned It," IEEE Ann. Hist. Comput., **15**, 1 (1993).

[80] Y. Zhang and Y. Zhou, "Transparent Computing : Spatio-Temporal Extension on von Neumann Architecture for Cloud Services," Transparent Comput., **18**, 1 (2013).

[81] D. Shin and H. J. Yoo "The Heterogeneous Deep Neural Network Processor With a Non-von Neumann Architecture," Proc. IEEE, **108**, 1245 (2020).

[82] C. Lüscher et al. "Synaptic plasticity and dynamic modulation of the postsynaptic," Nat. Neurosci., **3**, 545 (2000).

[83] E. Linn et al. "Beyond von Neumann — logic operations in passive crossbar arrays alongside memory operations," Nanotechnology, **23**, 30 (2012).

[84] H. Li et al., "A learnable parallel processing architecture towards unity of memory and computing," Sci. Rep., **5**, 13330 (2015).

[85] Y. Van De Burgt et al., "A non-volatile organic electrochemical device as a low-voltage artificial synapse for neuromorphic computing," Nat. Mater., **16**, 414 (2017).

[86] V. K. Sangwan and M. C. Hersam, "Neuromorphic nanoelectronic materials," Nat. Nanotechnol., **15**, 517 (2020).

[87] I. Boybat et al., "Neuromorphic computing with multi-memristive synapses," Nat. Commun., **9**, 2514 (2018).

[88] D. Silver et al., "Mastering the game of Go with deep neural networks and tree search," Nature, **529**, 484 (2016).

[89] L. Q. Zhu et al. "Artificial synapse network on inorganic proton conductor for neuromorphic systems," Nat. Commun., **5**, 3158 (2014).

[90] M. Prezioso et al. "Training and operation of an integrated neuromorphic network based on metal-oxide memristors," Nature, **521,** 61 (2015).

[91] Z. Wang et al., “Memristors with diffusive dynamics as synaptic emulators for neuromorphic computing,” Nat. Mater., **16**, 101 (2017).

[92] C. Wang at al. “Investigation and Manipulation of Different Analog Behaviors of Memristor as Electronic Synapse for Neuromorphic Applications,” Sci. Rep. , **6**, 22970 (2016).

[93] U. Bauer et al., “Magneto-ionic control of interfacial magnetism,” Nat. Mater., **14,** 174 (2014).

[94] A. J. Tan et al., “Magneto-ionic control of magnetism using a solid-state proton pump,” Nat. Mater.,**18**, 35 (2019).

[95] K. Lee et al., “Fast Magneto-Ionic Switching of Interface Anisotropy Using Yttria-Stabilized Zirconia Gate Oxide,” Nano Lett., **20**, 3435, (2020).

[96] S. Emori et al. “Large voltage-induced modification of spin- orbit torques in Pt / Co / GdO_x,” Appl. Phys. Lett., **105**, 222401, (2014).

[97] U. Bauer et al. “Voltage-controlled domain wall traps in ferromagnetic nanowires,” Nat. Mater., **8** , 411 (2013).

[98] A. W. Marsman et al. “Doped polyaniline polymer fuses : Electrically programmable read-only-memory elements,” J. Mater. Res., **19** , 7 (2004).

[99] H. Cha et al. “A 32-KB Standard CMOS Antifuse One-Time Programmable ROM Embedded in a 16-bit Microcontroller,” IEEE J. Solid-State Circuits, **41**, 9 (2006).

[100] K. P. Ng et al. “Diode Based Gate Oxide Anti-fuse One Time Programmable Memory Array in Standard CMOS Process,” IEEE International Conference of Electron Devices and Solid-State Circuits (EDSSC), 457-460 (2009).

[101] P. Dhanapal et al. “Reversibly controlled magnetic domains of Co film via electric field driven oxygen migration at nanoscale” Appl. Phys. Lett., **114**, 232401, (2019).

[102] P. Sahu et al. “Effects of mobile oxygen ions in top-gated synthetic antiferromagnet structure Effects of mobile oxygen ions in top-gated synthetic antiferromagnet structure,” Appl. Phys. Lett., **117**, 202405, (2020).

[103] Y-W Oh et al. “Interfacial perpendicular magnetic anisotropy in CoFeB / MgO structure with various underlayers,” J. Appl. Phys.,**115** , 17C724, (2014).

[104] T. Newhouse-Illige et al., “Voltage-controlled interlayer coupling in perpendicularly magnetized magnetic tunnel junctions,” Nat. Commun., **8**, 15232 (2017).

[105] D. M. Lattery et al. “Low Gilbert Damping Constant in Perpendicularly Magnetized W / CoFeB / MgO Films with High Thermal Stability,” Sci. Rep., **8**, 13395 (2018).

[106] K. Masuda and Y. Miura, “Perpendicular magnetic anisotropy at the Fe /$MgAl_2O_4$ interface : Comparative first-principles study with Fe / MgO,” Phys. Rev. Appl., **98**, 224421 (2018).

[107] S. Peng et al., “Origin of interfacial perpendicular magnetic anisotropy in MgO / CoFe / metallic capping layer structures,” Sci. Rep., **5**, 18173 (2015).

[108] J. Okabayashi et al. “Anatomy of interfacial spin-orbit coupling in Co/Pd multilayers using X-ray magnetic circular dichroism and first-principles calculations,” Sci. Rep., **8**, 8303 (2018).

[109] H. X. Yang et al. “First-principles investigation of the very large perpendicular magnetic anisotropy at Fe | MgO and Co | MgO interfaces,” Phys. Rev. B, **84**, 054401 (2011).

[110] A. Van Der Brink et al., “Field-free magnetization reversal by spin-Hall effect and exchange bias,” Nat. Commun. **7**, 10854 (2016).

[111] A. K. Nayak et al., “Design of compensated ferrimagnetic Heusler alloys for giant tunable exchange bias,” Nat. Mater.,**14** , 679 (2015).

[112] W. Echtenkamp and C. Binek, “Electric Control of Exchange Bias Training,” Phys. Rev. Lett., **111**, 187204, (2013).

[113] Q. Yang et al. “Perspectives of voltage control for magnetic exchange bias in multiferroic heterostructures,” Phys. Lett. A, **381**, 14 (2017).

[114] N. J. Gökemeijer et al. “Long-Range Exchange Bias across a Spacer Layer,” Phys. Rev. Lett., **79**, 4270 (1997).

[115] C. Binek et al. “Exchange Bias in a generalized Meiklejohn-Bean approach Exchange bias in a generalized Meiklejohn – Bean approach,” J. Magn. Magn. Mater., **234**, 353 (2001).

[116] M.A. Ruderman and C. Kittel“Indirect Exchange Coupling of Nuclear Magnetic Moments by Conduction Electrons,” Phys. Rev., **96**, 99 (1954).

[117] P. Bruno, “Theory of interlayer magnetic coupling,” Phys. Rev. B, **52**, 411, (1995).

[118] J. Qiu et al. “Effect of roughness on perpendicular magnetic anisotropy in $(Co_{90}Fe_{10} / Pt)_n$ superlattices,” AIP Adv., **6**, 056123, (2016).

[119] D.Yang et al. “Shape-controlled synthesis of palladium and copper superlattice nanowires for high-stability hydrogen sensors,” Sci. Rep., **4**, 3773 (2014).

[120] K. A. Kuttiyiel et al. “Gold-promoted structurally ordered intermettalic palladium cobalt nanoparticles for the oxygen reduction reaction,” Nat. Commun., **5**, 5185 (2014).

[121] G. H. O. Daalderop et al. “First principle calculations of the magnetocrystalline anisotropy energy of iron, cobalt and nickel” Phys. Rev. B, **41**, 11919 (1990).

[122] A. V. Davydenko et al. “Origin of perpendicular magnetic anisotropy in epitaxial Pd / Co / Pd (111) trilayers,” Phys. Rev. B, **95**, 064430 (2017).

[123] J. Lee et al. “Thermally robust perpendicular Co / Pd-based synthetic antiferromagnetic coupling enabled by a W capping or buffer layer,” Sci. Rep., **6**, 21324, (2016).

[124] T. N. A. Nguyen et al. “Effect of flattened surface morphology of anodized aluminum oxide templates on the magnetic properties of nanoporous Co / Pt and Co / Pd thin multilayered films,” Appl. Surf. Sci. **427** ,649 (2018).

[125] M. Gottwald et al., “Ultra-thin Co / Pd multilayers with enhanced high-temperature annealing stability,” Appl. Phys. Lett., **102**, 052405 (2013).

[126] J. . Chilress et al., “Perpendicular magnetic anisotropy in Co_xPd_{1-x} alloy films grown by molecular beam epitaxy Perpendicular magnetic anisotropy,” J. Appl. Phys.,**75** , 6412 (1998).

[127] G. G. An et al., “Correlation between Pd metal thickness and thermally stable perpendicular magnetic anisotropy features in $[Co/Pd]_n$ multilayers at annealing temperatures up to 500 ° C,” AIP Adv., **5**, 027137 (2015).

[128] J. H. Cho et al., “Printable ion-gel gate dielectrics for low-voltage polymer thin-film transistors on plastic,” Nat. Mater., **7 ,** 900 (2008).

[129] T. Sadi et al. “Investigation of resistance switching in SiO x Investigation of resistance switching in SiO_x RRAM cells using a 3D multi-scale kinetic Monte Carlo simulator,” J. Phys. Condens. Matter, **30** , 8(2018).

[130] Y. Wen and J. Zhang, “Surface energy calculation of the fcc metals by using the MAEAM,” Solid State Commun., **144,** 163 (2007).

[131] A. Natarajarathinam et al., “Perpendicular magnetic tunnel junctions based on thin CoFeB free layer and Co-based multilayer synthetic antiferromagnet pinned layers,” J. Appl. Phys., **111**, 07C918 (2012).

[132] Y. Huai et al., “Spin-valve heads with synthetic antiferromagnet CoFe / Ru / CoFe / IrMn,” J. Appl. Phys., **85**, 5528 (1999).

[133] V. Cremers et al. “Conformality in atomic layer deposition : Current status overview of analysis and modelling,” Appl. Phys. Rev., **6,** 021302, (2018).

[134] M. Akyol "Origins of Interfacial Magnetic Anisotropy in Ta/CoFeB/MgO and Pt/CoFeB/MgO Multilayer thin film stack" **32**, 457 (2019).

[135] F.J.A den Broeder et al. "Magnetic anisotropy of multilayers" Journal of Magnetism and Magnetic Materials, **93,** 562 (1991).

[136] J. Nogues and I.K. Schuller "Exchange bias" Jounal of Magnetism and Magnetic materials, **192**, 2 (1999).

[137] V. Jeudy et al. "Pinning of domain walls in thin ferromagnetic films" Phys Rev B, **98**, 054406 (2018).

[138] G.M. Wysin, "Magnetic excitations and geometric confinement: Theory and simulations" IOP Publishing, Chapter -3 (2015).

[139] Q. Yang et al. "Ionic liquid gating control of RKKY interaction in FeCoB/Ru/FeCoB and $(Pt/Co)_2/Ru/(Co/Pt)_2$ multilayers" Nat. Comm. **9**, 991 (2018).

[140] Zhang et al. "Bipolar electric-field switching of perpendicular magnetic tunnel junctions through voltage controlled exchange coupling" arxiv: 1912.10289.

[141] J. D. Rojas et al. "Voltage-driven motion of nitrogen ions: a new paradigm for magneto-ionics" Nat. Comm. **11**, 5871 (2020).

[142] G. Chen et al. "Observation of hydrogen-induced Dzyaloshinskii-Moriya interaction and reversible switching of magnetic chirality" Phys. Rev. X, **11**, 021015, (2021).

[143] G. Rippy et al. " X-ray nanodiffraction studies of ionically-controlled nanoscale phase separation in cobaltites" Phys. Rev. Mat., **3**, 082001(R) (2019)

APPENDIX-I

Journal Publications

- P. Sahu. J. C. Myers, J.Y. Chen, J.P. Wang, "Weak antilocalization and low temperature characterization of sputtered polycrystalline Bismuth Selenide", Appl. Phys. Lett. **112**, 122402 (2018).
- P. Sahu[#], D. Zhang[#], T. Peterson, JP Wang "Effects of mobile oxygen ions in top-gated synthetic antiferromagnet structure" Appl. Phys. Lett. **117**, 202405 (2020).
- P. Sahu, Y. Fan, T. Peterson, JY Chen, X. Devaux, H. Jaffres, S. Migot, H. Dang, J-M. George, Y. Lu, JP. Wang "Room Temperature Mott Hopping and Spin pumping Characterization of Amorphous Gd-alloyed Bi_2Se_3" arXiv:1911.03323.
- P. Sahu, JY. Chen, JP Wang "Charge trapping analysis in sputtered Bi_xSe_{1-x} based accumulation-mode FETs" AIP Advances **10**, 015315 (2020).
- P. Sahu, JY Chen, JP Wang, "Charge trapping analysis in sputtered Bi_xSe_{1-x} based accumulation-mode FETs. II. Gate capacitance characteristics" AIP Advances **11**, 015221 (2021).
- T.J. Peterson[#], P. Sahu[#], D. Zhang, M. DC, J.P. Wang, "Annealing Temperature Effects on Spin Hall Magnetoresistance in Perpendicularly Magnetized W/CoFeB Bilayers", IEEE Transaction on magnetics, **55**, 2 (2018).

- M. DC, JY Chen, T. Peterson, P. Sahu, B. Ma, N. Mousavi, R. Harjani, J.P. Wang "Observation of High Spin-to-Charge Conversion by Sputtered Bismuth Selenide Thin Films at Room Temperature" Nano Lett. 2019, **19**, 8, 4836–4844.
- M. DC, T. Liu, JY. Chen, T. Peterson, P. Sahu, H. Li, Z. Zhao, M. Wu, JP Wang, "Room-temperature spin-to-charge conversion in sputtered bismuth selenide thin films via spin pumping from yttrium iron garnet" Appl. Phys. Lett. **114**, 102401 (2019).
- Y. Fan, H. Li, M. DC, T. Peterson, J. Held, P. Sahu, JY. Chen, D. Zhang, A. Mkhoyan, JP. Wang "Spin pumping and large field-like torque at room temperature in sputtered amorphous WTe_{2-x} films" APL Materials **8**, 041102 (2020).
- Y. Lv, J. Kally, T. Liu, P. Sahu, M. Wu, N. Samarth and JP Wang "Large unidirectional spin Hall and Rashba-Edelstein magnetoresistance in topological insulator/magnetic insulator heterostructures" arxiv: 1806.09066.

Patents

- JP Wang, P. Sahu, "TOPOLOGICAL MATERIAL FOR TRAPPING CHARGE AND SWITCHING A FERROMAGNET" USTPO Publication no. 20210125651 (2021).
- JP Wang, D. Zhang, P. Sahu, "ELECTRIC FIELD SWITCHABLE MAGNETIC DEVICES" USTPO Application no. 16/861,869 (2020).

Selected conference Presentations

- P. Sahu et al. “Impurity dominated weak antilocalization in sputtered polycrystalline Bismuth Selenide“ International Conference on Magnetism, San Francisco (2018).
- P. Sahu, et al. “Thermal transport characterization by DC planar Hall measurement” Joint MMM-Intermag conference, Washington DC (2019).
- P. Sahu et al. “Characterization of Traps in Sputtered Topological Insulator FET Structures” MMM Conference, Las Vegas (2019).
- P. Sahu et al. “Charge trapping analysis in sputtered Bi_xSe_{1-x} based accumulation-mode FETs - Part 2”, MMM Conference Virtual conference (2020).
- P. Sahu et al. “Quasi-static C-V Characterization of Traps in Sputtered Bismuth Selenide FET” APS March meeting (2020).
- P. Sahu et al. “Material and Spin Transport Characterization in Gd-alloyed Bismuth Selenide” APS March meeting (2021).